Justus-Liebig-University Giessen
Institute of Experimental Physics I

Combining optical emission spectroscopy and multivariate data analysis methods for an empirical assessment of plasma parameters of ion thrusters

Dissertation to obtain the doctoral degree
Dr. rer. nat.

submitted by
Benny Thierry Nauschütt

reviewed by
Prof. Dr. Peter J. Klar and
Prof. Dr. Sangam Chatterjee

July 21, 2022

ABSTRACT

Rising demand of electric propulsion spacecrafts has triggered research for better, more reliable thrusters and alternative propellants. To increase the speed of development, testing and space qualification of these new thrusters and propellants, it is necessary to employ a wide range of diagnostics.

In this work, a new diagnostic method has been developed for characterizing the plasma of radio-frequency ion thrusters. However, the method should, in principle, also be applicable to other plasma based electric propulsion devices. The method makes use of plasma parameter measurements with established Langmuir probe diagnostics on a reference setup similar to a real thruster. At the same time, optical emission spectroscopy of the plasma near the Langmuir probe is performed. Both of these measurements are combined in order to reveal the correlation between a plasma's optical emission spectrum and its plasma parameters. An integral part of the evaluation process is the compression of the information contained in the spectrum, which is done using principal component analysis. Contrary to the normal procedure of getting plasma parameters from a spectrum, this method has no need for theoretical plasma models but is purely empirical. Therefore, it does not rely on databases with cross sections and transition probabilities. In particular, these circumstances make it a useful tool for analyzing complex plasmas made from gas mixtures or exotic propellants like iodine.

In the future, these diagnostic options may be employed to assist in thruster characterizations to speed up tests and qualification efforts.

ZUSAMMENFASSUNG

Die steigende Nachfrage an Raumfahrtzeugen mit elektrischen Antrieben treibt die Forschung für zuverlässigere Triebwerke und alternative Treibstoffe voran. Um die Geschwindigkeit in der Entwicklung, den Tests und der Weltraumqualifizierung dieser neuen Triebwerke und Treibstoffe zu beschleunigen ist ein breit aufgestelltes Sortiment an Diagnostiken erforderlich.

In dieser Arbeit wurde eine neue Diagnostikmethode entwickelt um Plasmaparameter von Hochfrequenz-Ionentriebwerken zu bestimmen. Allerdings sollte diese Methode prinzipiell auch auf andere plasmabasierte elektrische Triebwerke anwendbar sein. Für diese Methode werden die Plasmaparameter an einem Triebwerk oder einem triebwerkähnlichen Aufbau mit der etablierten Langmuirsondendiagnostik gemessen. Gleichzeitig werden Messungen mit optischer Emissionsspektroskopie an dem Plasma nahe der Langmuirsonde durchgeführt. Diese beiden Messungen werden kombiniert um die Korrelation zwischen dem optischen Emissionsspektrum des Plasmas und den Plasmaparametern aufzudecken. Ein integraler Bestandteil der Auswertung ist die Komprimierung der Informationen, die im Spektrum enthalten sind, was über eine Hauptkomponentenanalyse realisiert wird. Entgegen der gängigen Prozedur zur Bestimmung von Plasmaparametern aus Spektren ist diese Methode rein empirisch und benötigt kein theoretisches Modell des Plasmas. Daher werden keine Datenbanken mit Wirkungsquerschnitten und Übergangswahrscheinlichkeiten benötigt. Speziell deshalb ist diese Methode ein nützliches Werkzeug um komplexe Plasmen aus verschiedenen Gasen oder aus exotischen Treibstoffen wie Iod zu analysieren.

In Zukunft kann diese Diagnostik eingesetzt werden um bei der Charakterisierung und Qualifizierung zu helfen und Testprozeduren zu beschleunigen.

CONTENTS

DECLARATION

I declare that I have completed this dissertation single-handedly without the unauthorized help of a second party and only with the assistance acknowledged therein. I have appropriately acknowledged and cited all text passages that are derived verbatim from or are based on the content of published work of others, and all information relating to verbal communications. I consent to the use of an anti-plagiarism software to check my thesis. I have abided by the principles of good scientific conduct laid down in the charter of the Justus-Liebig-University Giessen "Satzung der Justus-Liebig-Universität Gießen zur Sicherung guter wissenschaftlicher Praxis" in carrying out the investigations described in the dissertation.

Benny Nauschütt

ACKNOWLEDGMENTS

I thank Ariane Group for providing the funding for the first 3.5 years of my Ph.D. studies in the framework of the JLU-Ariane Group Graduate School “Radio-frequency ion thrusters”.

I thank the ERDF for covering the funding for the final phase of my Ph.D. work within the Horizon 2020 program (Innovation Lab “Rough ambient Physics”).

I thank Peter J. Klar for giving me the opportunity to study for my Ph.D. in his research group “Ionentriebwerke”, for being my doctoral adviser, and for all the input and ideas he provided.

I thank Kristof Holste, the laboratory supervisor of the research group “Ionentriebwerke”, for the productive discussions and valuable insight.

I thank Limei Chen for introducing me to principal component analysis, which turned out to be an integral part to interpret my data.

I thank Patrick Dietz for sharing his well-founded experience and knowledge of ion thrusters, the lively debates and for his assistance during my research.

I thank the rest of the research group for a pleasant working atmosphere and the general helpfulness.

I also thank the red tape and aluminum foil, as my work would not have been possible without them.

I would like to thank the collective effort of everyone who I may have forgotten and not mentioned here.

1. INTRODUCTION

Today, space flight has gained considerable importance in modern society. This holds for telecommunication, internet, research or space exploration and observation [1]. Most applications of space flight require some sort of propulsion, as it is the only way to maneuver a spacecraft. For takeoff from Earth's surface, the use of high thrust chemical rockets is currently inevitable. When reaching an Earth's orbit the situation is different, as the spacecraft now already possesses the velocity corresponding to this orbit and only the drag, e. g., from the atmosphere, needs to be compensated requiring much smaller thrusts than the orbit raising itself. Such a stable orbit can be kept with a variety of propulsion systems. At the beginning of space flight history, smaller chemical thrusters were used to stabilize orbits. While the chemical thrusters are still being used, electric propulsion (EP) systems have become an established alternative [2–4]. While EP thrusters suffer from low thrust in comparison to their chemical counterpart, they can achieve significantly higher fuel efficiencies. This allows for a much lower mass of the whole propulsion system than it could be achieved with a chemical propulsion system for the same application. In space flight the total mass of a spacecraft is limited by the capabilities of the carrier rocket. Reducing the mass of the propulsion system means that more mass is available to better fulfill the actual purpose of the spacecraft, i. e., more payload can be accommodated, e. g., additional sensors may be installed or a more powerful antenna may be used. EP systems can also be employed to reduce launch costs, as a smaller carrier rocket can place the spacecraft in a low orbit while the EP thruster slowly moves the spacecraft to its target orbit.

To further enhance the capabilities of EP systems and to fully explore their advantages, research on these systems is still ongoing [3, 4]. The research on alternative propellants is one field, which gains increasing interest [3–17]. For plasma based thrusters, xenon is the commonly used propellant today, as it has a high mass, is chemically inert and has a fairly low ionization energy. It is, however, a rare and, therefore, expensive resource [4, 18, 19]. Alternatives are, for example, lighter and more abundant noble gases like krypton [5,6,9,11–13] or heavy molecular iodine [10, 15, 16].

Characterization, optimization, and qualification of EP thrusters require suitable tools. The development and refining of diagnostic systems is therefore an integral part of EP research. As many EP devices operate with a plasma of some sort to generate thrust, plasma diagnostics are widely used to study the processes inside or around the thruster [3, 4, 20–26]. Invasive probes provide a direct way of measuring plasma parameters like the electron temperature and density [27–29], but they are not viable for some thruster types due to the lack of access, e. g., in case of gridded ion thrusters. Invasive probes also disturb the plasma locally and are therefore less favorable, especially for characterizing small thrusters [20, 30].

Non-invasive techniques like beam diagnostics, thrust measurements, performance data and grid analysis are widely used techniques [31–33]. Another option to determine thruster parameters is optical emission spectroscopy (OES) [30, 34–43].

In this work, a measurement principle was developed and established which allows the determination of the internal parameters of a plasma, in particular electron temperature and density, using an empirical correlation of OES and Langmuir double probe measurements [42, 43].

In order for this method to work, a reference plasma is investigated in a wide range of operational points in terms of its optical emission spectrum and plasma parameters. Spectra and plasma parameters are acquired using a spectrometer with an intensified charge coupled device (ICCD) camera and a Langmuir double probe, respectively [42, 43]. The vast information from the spectra is compressed into small sets of new parameters using a principal component analysis (PCA) [44]. The PCA is a technique capable of reducing the dimensions of a data set like a set of spectra. Each spectrum consists of intensity values recorded at different fixed wavelength positions. Each wavelength position can be considered as a coordinate axis and the corresponding intensity value of a spectrum as its coordinate along this axis. A spectrum taken at n wavelength positions can be represented by a single point in the n-dimensional coordinate system spanned by the coordinates given by the wavelength positions. A series of spectra can be imagined as a cloud of data points which may correspond to a manifold of lower dimensionality. Rotating the coordinate system to a new coordinate system may help to distinguish the data adequately with a smaller number of coordinates. In this new coordinate system resulting from a PCA, the dimensions are called principal components and are sorted by their significance. It is usually sufficient to consider only the first few of these principal components to fully characterize the differences between the spectra. A spectrum can then be described with one value, or so called score, on each principal component axis. The resulting principal component scores and the plasma parameters are then coupled together and, thus, yield a correlation [42, 43]. This correlation is a function that describes the behavior of a certain plasma parameter according to a spectrum's principal component scores, which can be obtained from the already performed PCA. With such a correlation established, the optical emission spectrum of a comparable plasma is already sufficient to determine its plasma parameters.

The correlations can then be employed to investigate the behavior of plasma parameters in situations, where the Langmuir diagnostics are difficult to realize, e. g., in time-resolved measurements. Under the assumption that excitation and relaxation of the electronic states of the plasma atoms are in equilibrium, we applied such correlations to time-resolved spectral data in order to examine the time evolution of plasma parameters within one rf cycle [42]. Since the method works well for xenon, it was also applied to krypton and xenon/krypton mixed plasmas [43]. Another application could be to investigate the spatial distribution of plasma parameters inside a thruster by recording spectra at different positions as a reference for theoretical modeling.

Contrary to other OES methods, which rely on a theoretical microscopic plasma model and the underlying data for excitation cross sections and transition matrix elements (e. g. for argon [36, 45–58] or xenon [30, 34, 35, 37–41, 55, 59–61]), the approach in this work has no need for any external input data [42, 43]. This makes the method very versatile for plasmas with exotic propellants like iodine [15, 16] or propellant mixtures, where only few to no microscopic data is available. But also for regularly used propellants, such as xenon, this principle can yield valuable insight into the processes inside the plasma of a thruster and help to shorten testing and qualification times.

2. BACKGROUND AND FUNDAMENTALS

2.1 Radio-frequency ion thruster

The radio-frequency ion thruster (RIT) was invented by H. Löb in the 1960s [62, 63]. A schematic illustration of a RIT is shown in Fig. 2.1. The plasma in a RIT is contained by a discharge vessel made from a non-conductive and heat resistant material like quartz glass or aluminum-oxide. The vessel is surrounded by a coil, which is driven by a radio-frequency signal in the range of 1 MHz and which is responsible for generating a plasma. A system of grids biased with high voltages accelerates ions from the plasma inside the vessel to space and thus generates thrust [2–4]. The grid system consists of at least two grids. The screen grid has contact with the plasma and is biased with a high positive voltage up to several kilo-volts with respect to the satellite ground potential. The screen grid is usually very thin and has a high transparency. The acceleration grid (or short accel grid) is positioned behind the screen grid and is biased negative with several hundreds of volts. It serves as a shield for the screen grid against electrons from a neutralizer, which would otherwise be attracted by the positive high voltage. It also focuses the ions extracted from the plasma. Contrary to its name, the accel grid does not globally accelerate ions. While ions are accelerated towards the accel grid, they are decelerated after passing it, so the net acceleration comes only from the potential difference between the reference potential and the plasma, which is determined mainly by the voltage on the screen grid. In contrast to the screen, the accel grid is thicker and has smaller holes, so its transparency is lower. The holes in the two grids align to form extraction channels. The channels focus the ions from the plasma through the accel grid such that they form a directed beam. Since the ions are guided through the accel grid, the transparency of the grid system is higher for ions than for neutrals. Optionally, a third grid on spacecraft ground potential can be positioned behind the accel grid. This deceleration grid (or short decel grid) decelerates the extracted ions by the potential difference between accel and spacecraft ground. Since this deceleration is supposed to happen anyway, the decel grid does not reduce the thrust this way. By adding this third grid the accel grid is protected against charge exchange ions that form behind the thruster.

2.2 Lifetime issues

The lifetime of a RIT is limited by the degradation of its grid system, if the neutralizer is not considered. The degree of grid degradation is related to the chosen operational point of the thruster, which itself is related to the plasma parameters. To determine the plasma parameters under realistic conditions, the thruster has to be characterized without modifica-

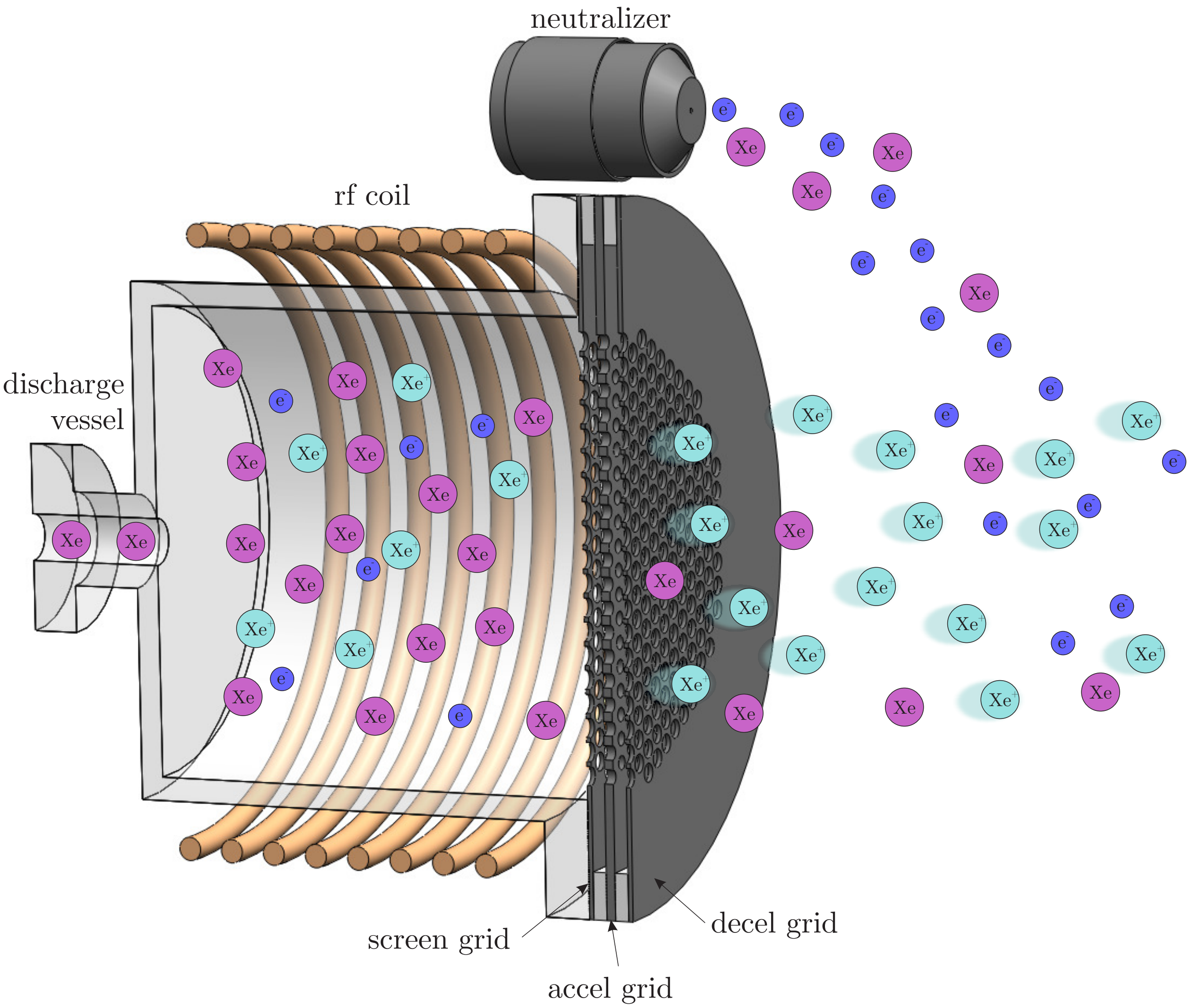

Fig. 2.1: Schematic image of a radio-frequency ion thruster. Propellant gas (here xenon) is inserted into the discharge vessel from the left. The plasma is maintained by an rf coil through inductive heating of the free electrons, which collide with the propellant atoms and ionize them. Ions passing the positively charged screen grid are accelerated towards the negatively charged accel grid. After passing the accel grid, the ions are slightly decelerated until exiting the thruster via the grounded decel grid. A neutralizer next to the RIT emits electrons to keep the overall reference potential constant.

tions or disturbances, which rules out the use of invasive diagnostics. Therefore, non-invasive diagnostics are necessary to characterize the plasma. During operation, the grids can degrade by three processes.

- *direct impingement:* The first and severest process is the direct impingement of accel-

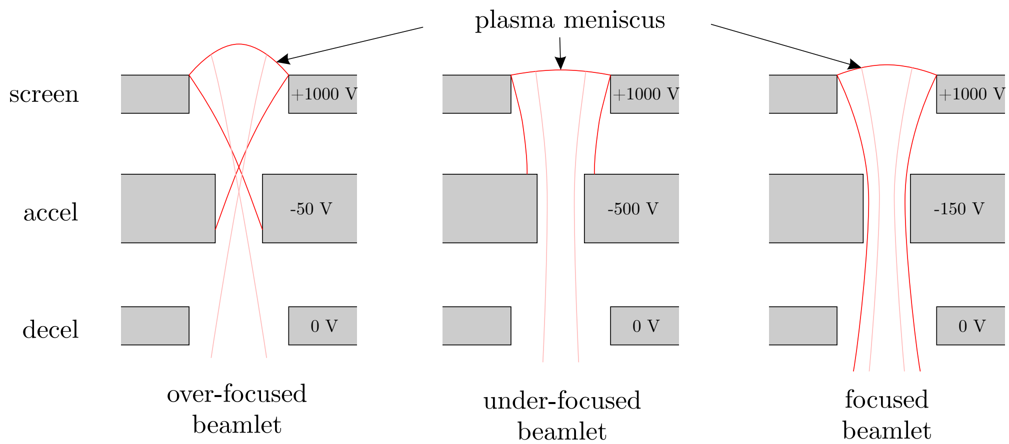

Fig. 2.2: Schematic depiction of correct and incorrect ion beam focusing for different accel grid voltages on the example of a single beamlet.

erated ions onto the acceleration grid [64]. This process is directly linked to the ion beam focusing and occurs when accelerated ions hit the acceleration grid directly as shown in Fig. 2.2. Here, the plasma parameters in conjunction with the grid voltages determine the plasma meniscus at the entrance of the extraction channels. The shape of this meniscus determines the focal point. The ion beam will be over-focused, if the plasma meniscus is strongly concave (Fig. 2.2 left). The ions are accelerated towards the acceleration grid but if over-crossing within the beamlet occurs, ions hit the acceleration grid instead of going through the extraction channel of the grid system. The ion beam will be under-focused, if the plasma meniscus is weakly concave (Fig. 2.2 center). A large fraction of ions is then accelerated directly onto the acceleration grid. On impact, the ions have an energy of

$$E = q(\Phi_{\text{plasma}} + U_{\text{screen}} - U_{\text{accel}}) \tag{2.1}$$

where q is the ion charge, Φ_{plasma} is the plasma potential and U_{screen} and U_{accel} are the voltages on the respective grids. The impact energy can be up to several kilo-electron volts, leading to an extremely high sputter yield. Taking the under-focused beam in Fig. 2.2 (center) as an example and assuming a titanium accel grid, xenon propellant and 40 V plasma potential, the sputter yield on perpendicular impact is $Y = 1.052\frac{\text{Ti}}{\text{Xe}^{+}}$ and $1.643\frac{\text{Ti}}{\text{Xe}^{2+}}$ [65]. In addition to the damage on the accel grid, the sputtered grid material may be deposited inside the plasma vessel causing a conductive coating on its surface, which shields the RF signal which excites the plasma and, thus, rapidly decreases the thruster's performance. Luckily, this process can be prevented by focusing the ion beam correctly (Fig. 2.2 right). However, defocusing may also occur despite the ion optics being set up correctly. If, e. g., an arc forms between the grids, it can temporarily cause an over-current on the acceleration grid. This may lead to a drop-off in the grid voltage, which itself changes the ion optics and therefore causes defocusing. Even after an arc the grid voltage cannot be restored immediately, since the ions impinging on the grid keep up the over-current. The best way to prevent premature grid failure by spontaneous defocusing is to choose an operating point with high tolerance to grid voltage changes and a controller, that detects defocusing and switches off the extraction.

- *charge exchange:* The plasma contains ions, but also neutrals. An electron can be transferred from a neutral to an ion, while neutral and ion velocity remain unchanged. This reaction is called charge exchange and may cause degradation of the accel grid, when it occurs inside the extraction channels [64, 66–69]. When an ion during acceleration gets an electron through charge exchange, the former ion continues its path and usually leaves the thruster, since it was already directed towards the outside. However, the former neutral, now with a positive charge, is attracted by the negative potential of the accel grid. Since it is relatively slow compared to the accelerated ion, the trajectory of the former neutral does not follow the focused ion beam and has a high probability of hitting the accel grid. At worst, the charge exchange ions can have an impact energy up to that of the (singly charged) accelerated ions, if they are generated close to the screen grid. However, charge exchange can also occur close to the accel grid, where the new, slow ion gains almost no energy before impact, leading to a range of possible impact energies with a maximum given by Eq. 2.1. Over time, the acceleration channels will increase in diameter due to sputtering by charge exchange ions. The sputtered accel grid material can, of course, also enter and coat the discharge vessel, similar to the case of direct impingement. Unfortunately, the charge exchange process cannot be prevented. It can, however, be reduced by lowering the pressure inside the discharge vessel. This lowers the amount of neutrals, that can undergo a charge exchange process with an ion. A lower discharge pressure comes with the downside of a higher power demand to maintain the same ion density in the plasma, so that the thrust remains constant.

- *screen sputtering:* Another downside of a lower discharge pressure is the increase in electron temperature. The bulk plasma is on the plasma potential Φ_{plasma}, which is higher than the wall potential Φ_{wall}. The ions in the plasma are therefore accelerated towards the walls by the potential difference between bulk and wall $\Delta\Phi = \frac{k_{\mathrm{B}}T_{\mathrm{e}}}{2e} \cdot \left(1 + \ln\left(\frac{m_{\mathrm{i}}}{2\pi m_{\mathrm{e}}}\right)\right)$ [70, 71], which is in the range of some tens of electron volts and scales linearly with the electron temperature. On the screen grid this potential difference may be enough to exceed the sputtering threshold of the grid material [64, 72]. Higher electron temperatures also cause more doubly charged ions, which hit the wall with twice the energy of singly charged ions and, thus, further increase the sputtering rate. Although not as severe as the direct impingement, the screen sputtering can also contribute to the coating of the inside of the plasma vessel with conducting material over time and decrease performance. A good balance between screen sputtering and charge exchange has to be found to maximize the thruster's lifetime.

2.3 Plasma in the RIT

To form a plasma, electrons are separated from some atoms in a gas. This ionized gas consists of ions and free electrons, and also neutral gas atoms. The atoms are ionized by collision with free electrons with energies higher than the ionization threshold of the neutrals. If the mean free path λ is much shorter than the dimensions of the plasma vessel, the atoms in a gas have energies that follow to a first approximation a Maxwell-Boltzmann distribution

$$f(E) = \frac{2}{\sqrt{\pi}} \cdot T^{-\frac{3}{2}} \sqrt{E} \cdot \mathrm{e}^{-\frac{E}{T}} \tag{2.2}$$

which is only defined by the temperature T. The mean free path λ is [73]

$$\lambda = \frac{1}{\sqrt{2} \cdot \pi d^2 \cdot n} \tag{2.3}$$

where d is the diameter defining the scattering cross section (488 pm at 273.15 K for xenon [73]) and n is the particle density. With an assumed particle density of $n = 2 \cdot 10^{19}\,\mathrm{m}^{-3}$, the mean free path is $\lambda = 4.7\,\mathrm{cm}$, assuming that the scattering cross section does not change significantly with thruster temperature. For a RIT-10 with a 10 cm diameter discharge chamber, the assumption of a Maxwell-Boltzmann energy distribution for neutrals and ions is a good approximation.

The plasma in a RIT is not in thermal equilibrium, which means that the individual species (neutrals, ions and electrons) are not at the same temperature. However, each species can be assigned a temperature, i. e., its energy distribution can be described by a Maxwell-Boltzmann distribution. In a RIT-10 under typical operating conditions, neutrals and ions are slightly above room temperature at around 500 K or 0.04 eV with the ions being slightly hotter. The electrons, which are accelerated in the RIT's rf E-field are, however, much hotter at around $58 \cdot 10^3$ K or 5 eV [2, 4]. The electrons are accelerated over multiple rf cycles to acquire the kinetic energy to ionize propellant atoms or molecules while simultaneously thermalizing by elastic collisions. The energy absorbed during the inductive heating of the electrons is transferred to the neutrals in inelastic collisions, leading to excitation and ionization of the collision partners. While ionization is a desired process in an ion thruster, losses due to excitation are unwanted but cannot be avoided. A RIT also has physical boundaries in form of its discharge chamber walls and grid system where electrons and ions are lost. While entering of ions into the grid system, where they generate thrust, is desired, losses to the discharge chamber walls contribute to a lowering of the electric efficiency of the thruster [2].

The electrons in an atom reside in quantized energy levels which can only be derived theoretically by solving Schrödinger's equation accounting for many-body effects, i. e., the Coulomb repulsion between electrons. These energy levels are distinguished by the quantum

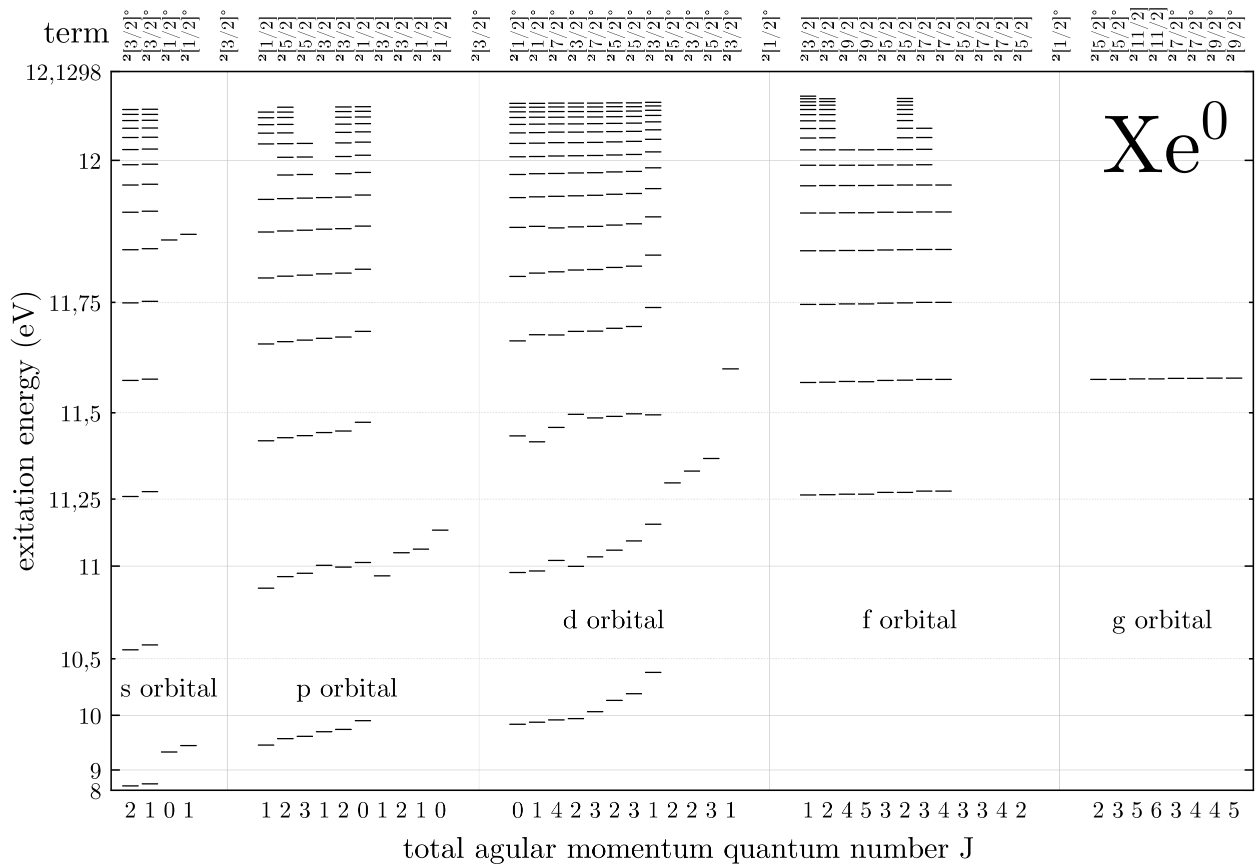

Fig. 2.3: Overview of the energy levels of neutral xenon. 341 out of the 443 levels listed in Ref. 74 are shown. The energy axis has an exponential scale to visually separate the higher energy levels with the maximum set to xenon's ionization energy of roughly 12.1 eV [74].

numbers. An electron has to make a transition to another energy level either by external excitation or radiative or non-radiative relaxation in order to change its energy. As an example, the energy levels of xenon according to Ref. 74 are shown in Fig. 2.3. The electrons in an atom can be excited to a higher energy level by absorption of photons, or collision with electrons or other heavier species like atoms or ions. A radiative relaxation from an excited state E_{upper} to the state E_{lower} produces a photon of the energy $E_{\mathrm{photon}} = E_{\mathrm{upper}} - E_{\mathrm{lower}}$. In most cases, this relaxation happens by spontaneous emission of a photon. The optical transition from one energy level to another has a certain probability, usually given by the Einstein coefficient $A_{k,i}$, which is the inverse half-life or relaxation time. Optical transitions with a high Einstein coefficient usually produce stronger spectral lines than transitions with a lower Einstein coefficient from the same original level, as more photons are generated in a given time in an ensemble of atoms. It is also possible to trigger the emission of a photon by stimulating an excited atom with another photon of the same energy. This stimulated emission is the basis of lasers. However, only the spontaneous emission is relevant in this work as the probability of stimulated emission is orders of magnitude smaller than that of spontaneous emission under the experimental conditions used. A defined continuous excitation of an ensemble of atoms or a plasma typically yields a stationary state of the system with an equilibrium of excitation and non-radiative and radiative recombination processes. This also implies that the relaxation processes between the electronic states are in a steady state. As a consequence the optical emission spectrum of such a system is characteristic for the system's excitation state. The emitted photons can be collected by an optical system and be recorded by a spectrometer with detector for further analysis.

Knowing all relevant microscopic processes and parameters, a plasma can be modeled theoretically on a microscopic level. Such models can give valuable insight during the design phase of a thruster to get estimations on the power consumption and performance [75,76]. By modeling the excitation and relaxation processes utilizing the knowledge about cross sections, selection rules and transitions, the plasma's optical emission spectrum can in principle be calculated.

In reality, however, setting up a reliable theoretical microscopic model of a plasma is a severe challenge. The model needs input in form of plasma parameters like the electron temperature. This temperature refers to a Maxwell-Boltzmann electron energy distribution function (EEDF) as shown in Eq. 2.2. While the assumption of a Maxwell-Boltzmann energy distribution is sufficient for the neutral gas and ions, the electron energy distribution function (EEDF) cannot necessarily be described by Eq. 2.2, as the fast electrons in the Maxwell tail may be suppressed [51, 77–79]. Instead of Eq. 2.2, the EEDF can be described by a more general approach given as [77–79]

$$f(x, E) = c_1' \cdot T^{-\frac{3}{2}} \sqrt{E} \cdot \mathrm{e}^{-c_2' \left(\frac{E}{T}\right)^x} \tag{2.4}$$

with the parameters c_1' and c_2' being

$$c_1' = x \cdot \left(\frac{2}{3}\right)^{\frac{3}{2}} \frac{\Gamma\left(\frac{5}{2x}\right)^{\frac{3}{2}}}{\Gamma\left(\frac{3}{2x}\right)^{\frac{5}{2}}} \quad \text{and} \quad c_2' = \left(\frac{2}{3}\right)^x \left(\frac{\Gamma\left(\frac{5}{2x}\right)}{\Gamma\left(\frac{3}{2x}\right)}\right)^x \tag{2.5}$$

where $\Gamma(x)$ is the gamma function.

The general energy distribution function complicates the modeling by adding the additional shape parameter x. If x is equal to 1, Eq. 2.4 will yield Eq. 2.2. Increasing x suppresses the Maxwell tail until a Druyvesteyn distribution is reached at $x = 2$.

In addition, the density distributions are dependent on, e. g., the shape of the plasma vessel, rf-coil and grid geometry as well as the operational point of the thruster. Assumptions can, for example, be made based on simulations or previous experiments. As the densities can vary spatially, the temperatures will also vary.

The plasma parameters and their distributions are responsible for the state of the plasma and, therefore, its excitation, which means that the optical emission spectrum is strongly related to the plasma parameters describing the state of the system. However, the mechanisms of excitation and relaxation are quite complex with a huge number of energy levels and species to consider. For single atomic plasmas like noble gases, the amount of species that has to be considered is still manageable. Molecular plasmas like nitrogen, oxygen or iodine, however, consist of more species as the molecules can dissociate and form positive as well as negative ions. Lighter noble gases like helium or argon are less complex due to the lower number of energy levels that have to be considered. There are theoretical microscopic models that simulate the excitation and relaxation between the energy levels of an electronic system, some with more, others with less complexity [30, 34–41, 45–61]. These models typically modify their input parameters to match measured and simulated spectrum or find correlations between line intensities and plasma parameters and apply them to a measured spectrum. The models usually focus on the most relevant transitions and excitation mechanisms for their specific application to reduce the complexity. These simplifications are, however, not necessarily valid for other applications, if other gases are used or the excitation or ionization mechanism is different. To give an example: Literature lists 443 energy levels for neutral xenon alone [74], while only 173 levels are considered in the model in Ref. 37 and only 38 levels in Ref. 61. Sometimes it might be justified to neglect some interaction mechanisms like excitation in ion-atom collisions or electron excitation of already excited atoms (excitation from metastable states). In other cases, these mechanisms are essential to yield a result close to reality [35]. Aside from simplifications for the sake of reducing complexity of a model, the cross sections needed to calculate excitation rates for the different species and energetic levels are not always available. Furthermore, it is difficult to determine such missing parameters experimentally or to predict them theoretically [80–85]. This gets even more difficult when implementing a model of a plasma of mixed gases or a molecular propellant.

To show that a model is working correctly and is predictive, a comparison with a direct plasma parameter measurement and optical emission spectra is inevitable.

2.4 Optical emission spectroscopy

A spectrometer uses diffraction to disperse photons of different wavelengths. A detector then measures the amount of photons $I(\lambda)$ and their respective positions on the detector corresponding to a wavelength λ. If the wavelength positions of the measurement system and the detector response is determined, the optical emission spectra obtained will be independent of the measurement system and indeed characteristic for the emitter. In case of a plasma, the spectrum contains information about the composition of the plasma, the density and the excitation conditions.

In this work, a Czerny-Turner spectrometer with an optical length of 0.5 m is used to disperse the light from a plasma. A *Princeton Instruments PI-MAX 4 1024f* intensified charge-coupled device (ICCD) camera was attached to the spectrometer and served as detector. The *Lightfield* software was used to control the ICCD. With the ICCD both continuous-wave (cw) as well as time-resolved measurements on the nanosecond scale were conducted. In the near infrared (NIR) region (around 830 nm), the setup of spectrometer and ICCD reaches a resolution of about 28 pm/pixel. In the near ultra-violet (NUV) region (around 390 nm) the resolution gets slightly worse with about 33 pm/pixel.

The operating principle of the Czerny-Turner spectrometer is shown in Fig. 2.4. To measure a spectrum, the light from the plasma is focused onto the slit of the spectrometer, either

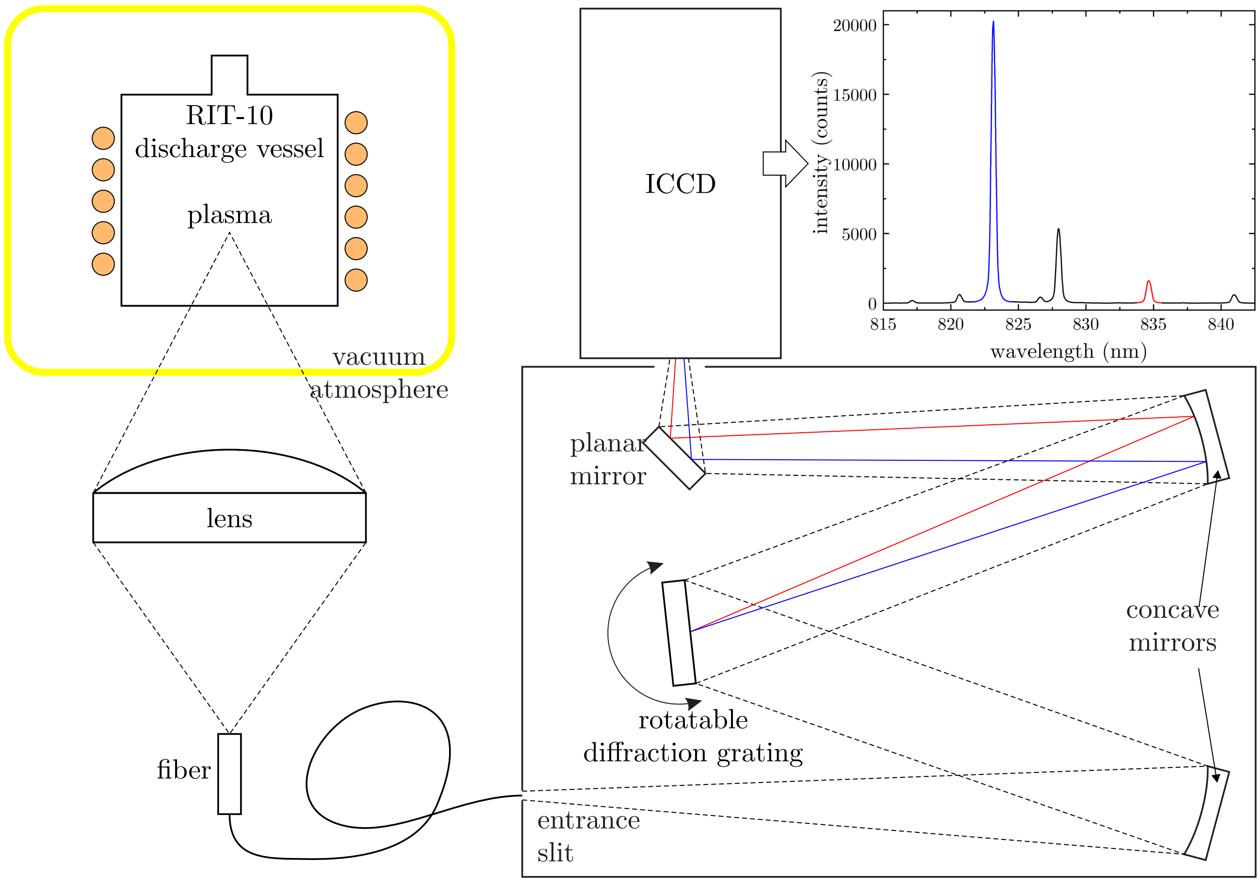

Fig. 2.4: The setup and operating principle of the used parallel Czerny-Turner spectrometer is shown. Light from the plasma is focused on a fiber through a lens. The fiber is connected to the entrance slit of the Czerny-Turner spectrometer. The light is dispersed by wavelength on a diffraction grid and recorded by an ICCD camera, yielding an optical emission spectrum.

directly or via an optical fiber. From the slit the light travels through the spectrometer and falls on a concave mirror, where the light is parallelized and reflected towards a reflective diffraction grating. This grating disperses the incoming light according to the wavelengths of its photons. The dispersed light, typically of the first order of diffraction, falls onto another concave mirror to focus it onto the detector array. The focal points of the different wavelengths are located on a line across the detector array due to the diffraction of the light by the grating. Light of the same wavelength falls on the same column of the detector array and its intensity is integrated yielding $I(\lambda)$. The light that does not hit the second concave mirror is absorbed by the black walls of the spectrometer. The wavelength range falling onto the ICCD array can be selected by rotating the diffraction grating as indicated in Fig 2.4. After recording, the spectrum needs to be response corrected to be comparable with theoretical spectra.

2.5 Principal Component Analysis

2.5.1 Basic principle

A typical challenge in analyzing measurements may be that the information of interest is hidden in a data set consisting of a large number of correlated variables. Such a situation may add a high degree of complexity to the evaluation and good ways of extracting the desired information need to be found. One example of such measurements is an optical emission spectrum. To resolve the line shape of all the optical emission lines in the range of interest, an optical emission spectrum typically consists of $I(\lambda)$ recordings with several closely spaced sampling points λ across each emission line. These may be in the order of 1000 sampling points in the spectral range of interest. As a consequence there will be strong correlations between $I(\lambda)$ and $I(\lambda')$ recorded at different λ and λ'. A possible way to shed light on the data, i. e., to reveal correlations or differences clearly, is the reduction of the dimensions of the problem. In short, a new and smaller set of variables can be found which sufficiently describes the large amount of information contained in the measured data. Several techniques exist to reduce dimensions of a set of variables like factor analysis [86], non-negative matrix factorization [87], linear-discriminant analysis [88] and principal component analysis (PCA) [44], which was used in this work.

The PCA determines a new set of axes which are sorted by the variance in the data they cover. The first axis or principal component PC_1 covers the largest fraction of the total variance, the second axis PC_2 covers the second largest fraction, and so on.

Fig. 2.5 illustrates the process of the PCA. A set of points is arranged in a flat ellipsoidal pattern, which is located shifted and rotated in a three-dimensional coordinate space. The three main axes of the ellipsoid in Fig. 2.5 are easy to spot. The direction with the longest axis has the highest variance. The PCA first determines the axis with the highest variance, which is very close to the main axis of the ellipsoid and shown as a red line in Fig. 2.5. The second highest variance is found on an axis close to the second axis of the ellipsoid (shown as a blue line) and the last axis along the flat side of the ellipsoid (shown as a green line). As there are only three dimensions, there can only be three principal components. The principle directions also form a cartesian coordinate system, i. e., the directions are perpendicular to each other.

The points are transformed into the new coordinate system of PC_1 (red), PC_2 (blue) and PC_3 (green) which can be seen in Fig. 2.6. The coordinates of a point in this PC-coordinate system are also called scores. Since PC_3 follows the flat side of the ellipsoid pattern, it does not hold much additional information about the main differences in the data set and is therefore not shown in Fig. 2.6. From the PCA result, further evaluations and interpretations are more facile than from the original data. In this simple example, the process is very intuitive, but the PCA can also be applied to data with a higher amount of variables or dimensions. In addition, the computational power required to perform a PCA is not high, as only some linear vector algebra needs to be performed.

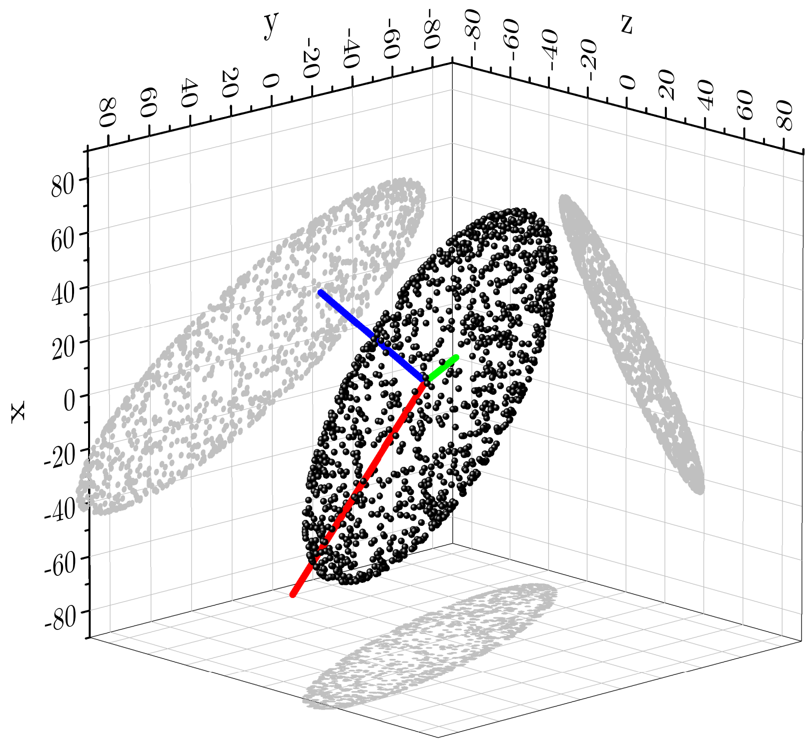

Fig. 2.5: A set of artificial data, arranged on a shifted and rotated ellipsoid. The red, blue and green lines represent the axes of highest variance PC_1, PC_2 and PC_3, which resulted from a principal component analysis.

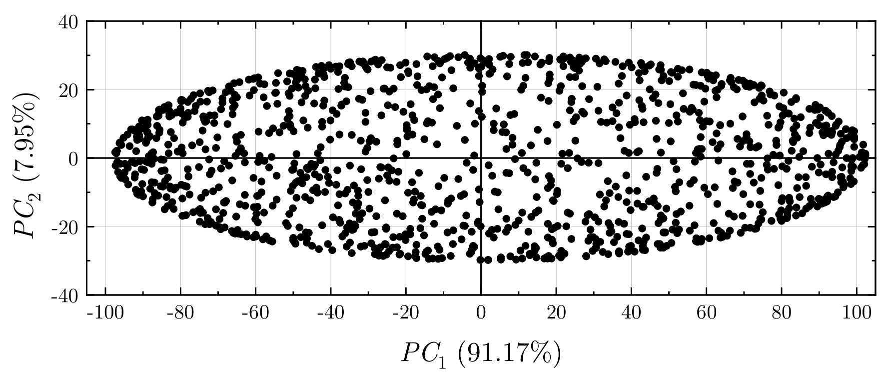

Fig. 2.6: The artificial data shown in Fig. 2.5 but transformed into the PCA coordinate system spanned by the red, blue and green line in Fig. 2.5. The green PC_3-axis is not shown, as it barely adds more information. The coordinates of each data point are also called scores.

2.5.2 Algorithm to perform a PCA

The mathematical formalism behind the PCA is shown in more detail below for an n-dimensional data set. This set of m measurements ($\vec{S}_1$ to $\vec{S}_m$) with a number of n measured variables each is defined as

$$\vec{S}_1 = \begin{pmatrix} x_{11} \\ x_{12} \\ \vdots \\ x_{1n} \end{pmatrix}, \vec{S}_2 = \begin{pmatrix} x_{21} \\ x_{22} \\ \vdots \\ x_{2n} \end{pmatrix}, \ldots, \vec{S}_m = \begin{pmatrix} x_{m1} \\ x_{m2} \\ \vdots \\ x_{mn} \end{pmatrix}. \tag{2.6}$$

The averages of a variables $\overline{x_i}$ $(i = 1, ..., n)$ form the average of all measurements $\langle\vec{S}\rangle$

$$\langle\vec{S}\rangle = \begin{pmatrix} \overline{x_0} \\ \overline{x_1} \\ \vdots \\ \overline{x_n} \end{pmatrix} \tag{2.7}$$

which is subtracted from the data before further evaluation to center them like it was done in Fig. 2.6. From these measurements the covariance matrix $\mathbf{C}$ is set up as

$$\mathbf{C} = \begin{pmatrix} \sigma_{11} & \sigma_{12} & \ldots & \sigma_{1n} \\ \sigma_{21} & \sigma_{22} & \ldots & \sigma_{2n} \\ \vdots & \vdots & \ddots & \vdots \\ \sigma_{n1} & \sigma_{n2} & \ldots & \sigma_{nn} \end{pmatrix} \tag{2.8}$$

where the individual covariances σ_{ij} are calculated according to

$$\sigma_{ij} = \frac{1}{m} \cdot \sum_{k=1}^{m} (x_{ik} - \overline{x_i}) \cdot (x_{jk} - \overline{x_j}). \tag{2.9}$$

The eigenvalues of the covariance matrix $\mathbf{C}$ $(\lambda_1 \geq ... \geq \lambda_n \geq 0)$ are the variances of the data in the direction of the eigenvectors $\overrightarrow{PC}_i$. These eigenvectors of the covariance matrix $\mathbf{C}$ are the principal component axes, which form an orthogonal system that serves as a new coordinate system. The first few principal components represent the differences in the data set almost entirely, since the eigenvectors are sorted by variance.

One way to compute these eigenvectors is to multiply a random vector $\vec{e}_0$ with the matrix $\mathbf{C}$ and normalize the result. This multiplication is performed multiple times until the resulting vector converges to a constant value as shown in Eq. 2.10.

$$\vec{e}_{i+1} = \frac{\mathbf{C} \cdot \vec{e}_i}{|\mathbf{C} \cdot \vec{e}_i|} \quad \text{until} \quad \vec{e}_{i+1} = \vec{e}_i. \tag{2.10}$$

This constant vector $\vec{e}_i$ is then the first eigenvector and, in case of the PCA, the first principal component axis $\overrightarrow{PC}_1$. The length $|\mathbf{C} \cdot \vec{e}_i|$ or $|\mathbf{C} \cdot \overrightarrow{PC}_1|$ is the first eigenvalue λ_1 corresponding to the variance along $\overrightarrow{PC}_1$, so Eq. 2.10 becomes

$$\lambda_1 \cdot \vec{e}_i = \mathbf{C} \cdot \vec{e}_i. \tag{2.11}$$

The coordinates or scores on this PC_1-axis are calculated by scalar multiplication of the data vector $\vec{S}_i$ and $\overrightarrow{PC}_1$

$$PC_{1,i} = \vec{S}_i \cdot \overrightarrow{PC}_1 \quad \text{with} \quad i = 0...m. \tag{2.12}$$

To obtain the second eigenvector, the PC_1-axis is subtracted from the data points $\vec{S}_i$

$$\vec{S}_i{}' = \vec{S}_i - PC_{1,i} \cdot \overrightarrow{PC}_1 \quad \text{with} \quad i = 0...m. \tag{2.13}$$

Afterwards the new covariance matrix $\mathbf{C}'$ is calculated according to Eq. 2.8. The second eigenvector and principal component axis $\overrightarrow{PC}_2$ is determined by the same repetitive multiplication used for $\overrightarrow{PC}_1$ as shown in Eq. 2.10, just with $\mathbf{C}'$ instead of $\mathbf{C}$. The score calculation and data reduction is also performed equivalently to Eq. 2.12 and 2.13.

This algorithm is continued until all n eigenvectors are found. If the data is made up of a large number of variables, it can be advantageous to just compute the first few eigenvectors instead of all, since their relevance for the data separation decreases with each step.

With all (relevant) eigenvectors calculated, the data can be described as a linear combination of the average spectrum (see Eq. 2.7) and all PCA-axes scaled by their scores

$$\vec{S}_i = \langle \vec{S} \rangle + \sum_{j=1}^{n} PC_{j,i} \cdot \overrightarrow{PC}_j \tag{2.14}$$

The described algorithm is summarized as a flow chart in Fig. 2.7.

2.5.3 Data pre-processing

OES measurements offer a suitable means of non-invasively probing the plasma inside an ion thruster. While it is easy to perform such a measurement, some care has to be taken before the measurements while setting up the experiment, during the measurements, as well as afterwards while evaluating the collected data in order to ensure the acquisition of a consistent and comparable data set.

The PCA is very sensitive towards small changes in the analyzed data. Such changes can be tiny wavelength drifts of the spectra due to temperature changes, vibrations or other mechanical shocks. These factors can be reduced by using a sturdy setup in an air-conditioned laboratory, which also reduces the disturbances in the measured spectra.

Another important point is the background in the spectra. To avoid an influence of the background on the PCA, a measured spectrum has to be background corrected. Ideally, optical measurements are performed in a dark room with minimal and constant background. This background can then be measured in advance and be subtracted from the measurements directly. In reality, ion thrusters need large vacuum chambers that are typically not located in dark rooms. In this case, providing a constant background is a good compromise. It is practically the same as in a dark room but of somewhat higher intensity. If a constant background cannot be provided, e. g., due to natural light entering the laboratory, the background will have to be estimated for each measurement individually. Here, the regions without emission lines can be used as background directly. In the regions with emission lines the background has to be approximated using the regions without emission lines as a reference.

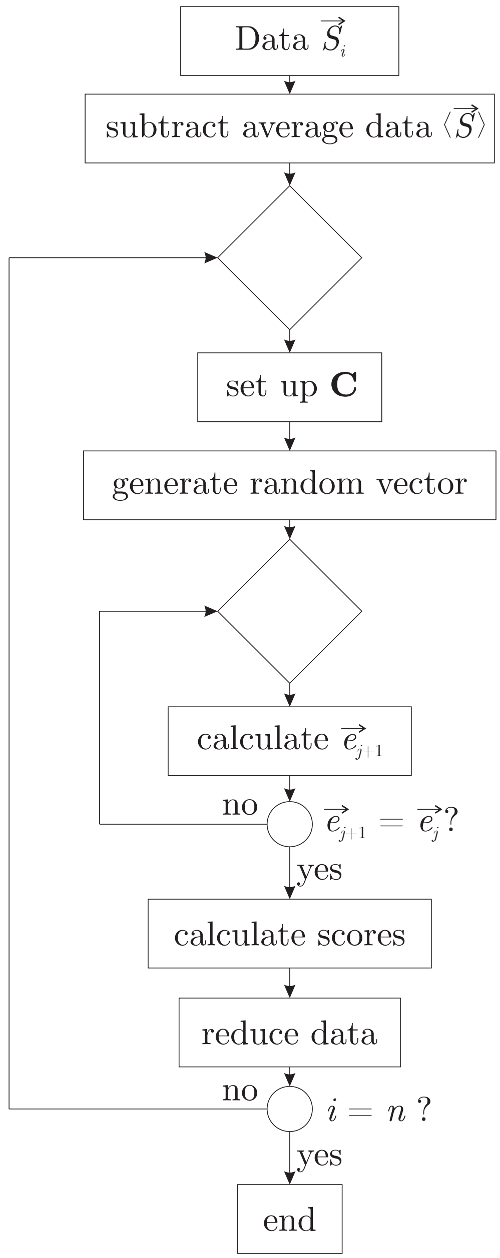

Fig. 2.7: A flow chart of an algorithm that performs a PCA by setting up the covariance matrix and computing its eigenvectors.

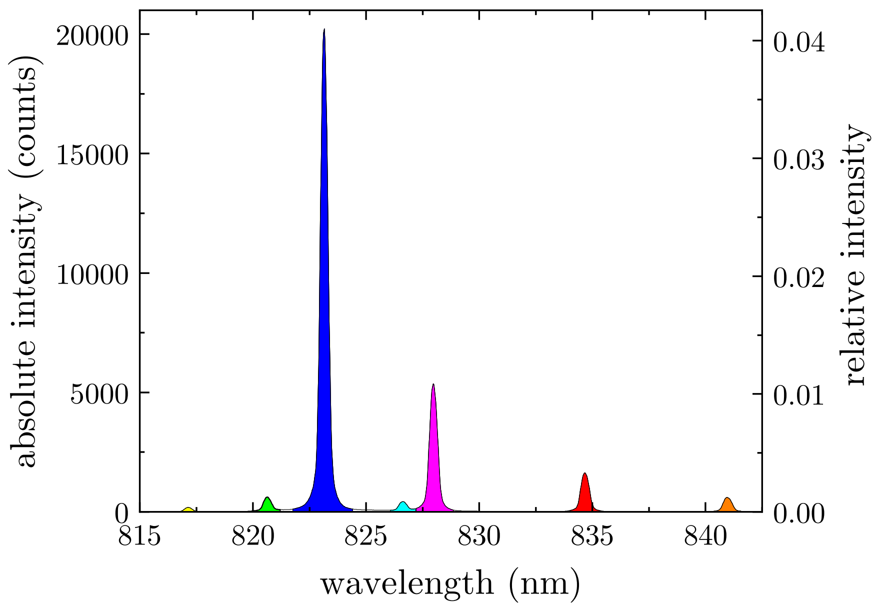

Fig. 2.8: Example of a xenon spectrum in the region of 815 to 842.5 nm. The regions in which the individual lines are integrated are shown in different colors. The relative spectrum is obtained by normalizing the absolute spectrum with the summed intensity of the full spectrum.

If optical measurements are performed with different setups, the spectra can vary due to the optical transmission properties of the components used. So, measurements have to be corrected for the optical response of the measurement system prior to comparing them with measurements taken with another setup. To determine the optical response, a light source with a known spectrum $S_{\mathrm{real}}(\lambda)$ is measured with the optical setup used for the experiment, yielding the measured spectrum $S_{\mathrm{measured}}(\lambda)$. The response correction function $f_{\mathrm{correction}}(\lambda)$ for this setup is then given by

$$f_{\mathrm{correction}}(\lambda) = \frac{S_{\mathrm{real}}(\lambda)}{S_{\mathrm{measured}}(\lambda)}. \tag{2.15}$$

Spectra measured during the experiment $S'_{\mathrm{measured}}(\lambda)$ can then be multiplied by $f_{\mathrm{correction}}(\lambda)$ to yield the setup-independent spectrum $S'_{\mathrm{real}}(\lambda)$.

On different setups or measurement series, the intensities might be different, e. g., due to other distances or detector settings. To compare different spectra to one another, it is often advantageous to compare relative spectra instead of absolute ones. For absolute spectra, a PCA would yield the overall intensity as the axis with the highest variance, although the main subject of interest is the change in line intensity ratios. Here, a spectrum is normalized by dividing it by the integral intensity of the full spectrum after having performed background and response corrections. The spectrum shown in Fig. 2.8 also has a relative intensity axis on the right.

In addition, the intensities of the individual emission lines are integrated by adding the counts of all wavelength positions that fall into the linewidth interval as illustrated in Fig. 2.8.

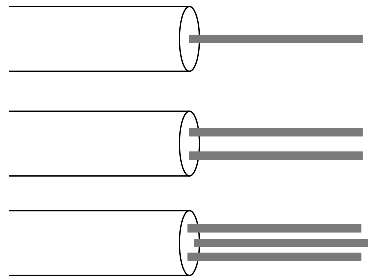

Fig. 2.9: Schematic images of three Langmuir probe types (single, double and triple) with cylindrical electrodes in a ceramic holder.

So, technically it is not a real integration since this would require a multiplication with the wavelength difference between two wavelength positions $\Delta\lambda$. The result is a cumulative intensity over the linewidth instead of the area under the curve. Since $\Delta\lambda$ is approximately constant within the observed spectral region, the results are unaffected by this simplification.

2.6 Langmuir probes

Electrical probes can be used to measure both temperature and densities of the charged species inside a plasma. Some probes can also determine the detailed electron energy distribution function (EEDF) from which the shape parameter x (see Eq. 2.4) can be extracted in addition to the temperature. A suitable tool for plasma diagnostics are Langmuir probes [27–29,89]. Essentially a Langmuir probe is a wire in the plasma, biased with a voltage. This voltage is then swept from negative to positive values to determine the voltage-current characteristic of the plasma, which can be analyzed to determine characteristic parameters of the probed plasma, such as electron temperature, density or EEDF.

To reduce the influence of plasma effects on the measurement, a second wire can be inserted into the plasma close to the first wire [27–29, 89]. The sweeping voltage is applied between the two wires. However, a double probe is somewhat restricted in the determinable plasma parameters and can only yield electron temperature and density.

A third wire may be added to be fully unaffected by rf-influences [28, 89]. Here, three points on the characteristic double probe curve are constantly measured, yielding the electron temperature and density very quickly. However, since only three points of the characteristic are known, the real shape of the curve is unknown and has to be estimated.

Here, a Langmuir double probe has been used in all measurements. The schematic setup is shown in Fig. 2.10. The plasma is generated in a RIT-10 discharge vessel. The Langmuir double probe is inserted in this discharge vessel through a special gas inlet. The Langmuir double probe is realized as two cylindrical tungsten electrodes at the end of a ceramic holder. The electrodes are connected to wires inside this holder. The wires run through the holder outside the discharge vessel. From there, each wire is connected to two cables to realize a four-wire measurement, so cable resistances can be neglected. The *Keysight B2901A Precision Source/Measurement Unit* is used as a power supply as well as the voltage and current

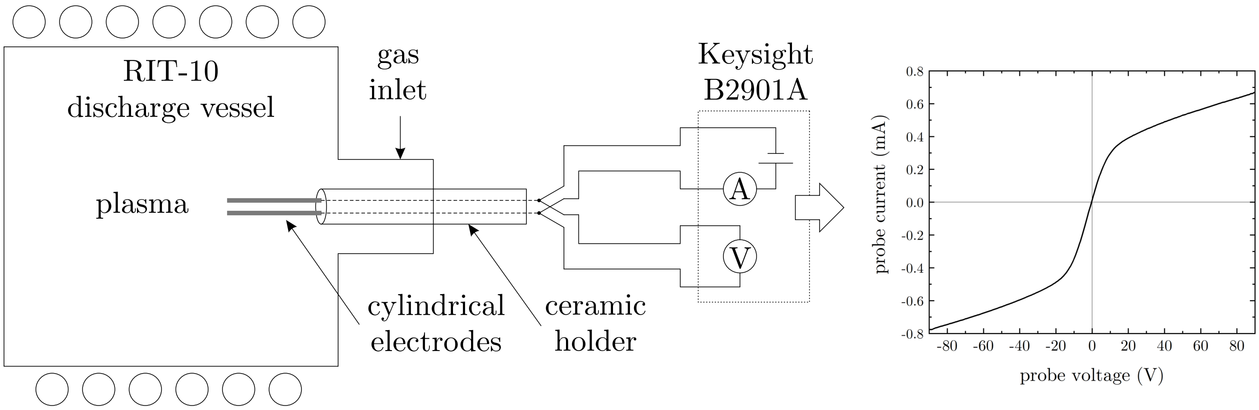

Fig. 2.10: Schematic image of the measurement setup with a Langmuir double probe.

measurement system. The voltage is increased from $-100\,\mathrm{V}$ to $+100\,\mathrm{V}$ in , e. g., $0.1\,\mathrm{V}$ steps each $50\,\mathrm{ms}$, yielding the typical Langmuir double probe characteristic as shown in Fig. 2.10.

In general, a plasma can be characterized by the energy and density distributions of its individual species. The Langmuir double probe used here can, of course, not measure all these parameters, so a few assumptions have to be made. Since the probe measures only on a specific location inside the plasma, a density distribution can only be determined, if a movable probe is used, which was not the case here. Here, the following assumptions were made:

- low temperature plasma $T_\mathrm{n} = T_\mathrm{i} = T_\mathrm{ambient}$
  Since the plasma in a RIT is an rf plasma, it is assumed that neutral gas temperature and ion temperature are close to the ambient temperature.

- low ionization degree $n_\mathrm{n} = n_\mathrm{total}$
  Due to a low ionization degree, it is assumed, that the ion pressure has no significant contribution to the total gas pressure. This also includes the assumption, that no significant amount of doubly (or higher) charged ions is present in the plasma.

- quasi-neutral plasma $n_\mathrm{e} = n_\mathrm{i}$
  The global plasma is assumed to be neutral, so the electron and ion densities are equal. Local inhomogeneous densities like in the plasma sheaths are not taken into account here.

- Maxwell-Boltzmann energy distributions $(x = 1)$
  All energy distributions are assumed to be Maxwell-Boltzmann distributions. This is sufficient for neutrals and ions, but can cause deviations for electrons, as their energy distribution functions may be different.

- to be measured: T_e and n_e
  This cuts the remaining plasma parameters that have to be measured down to the electron temperature and the electron or ion density.

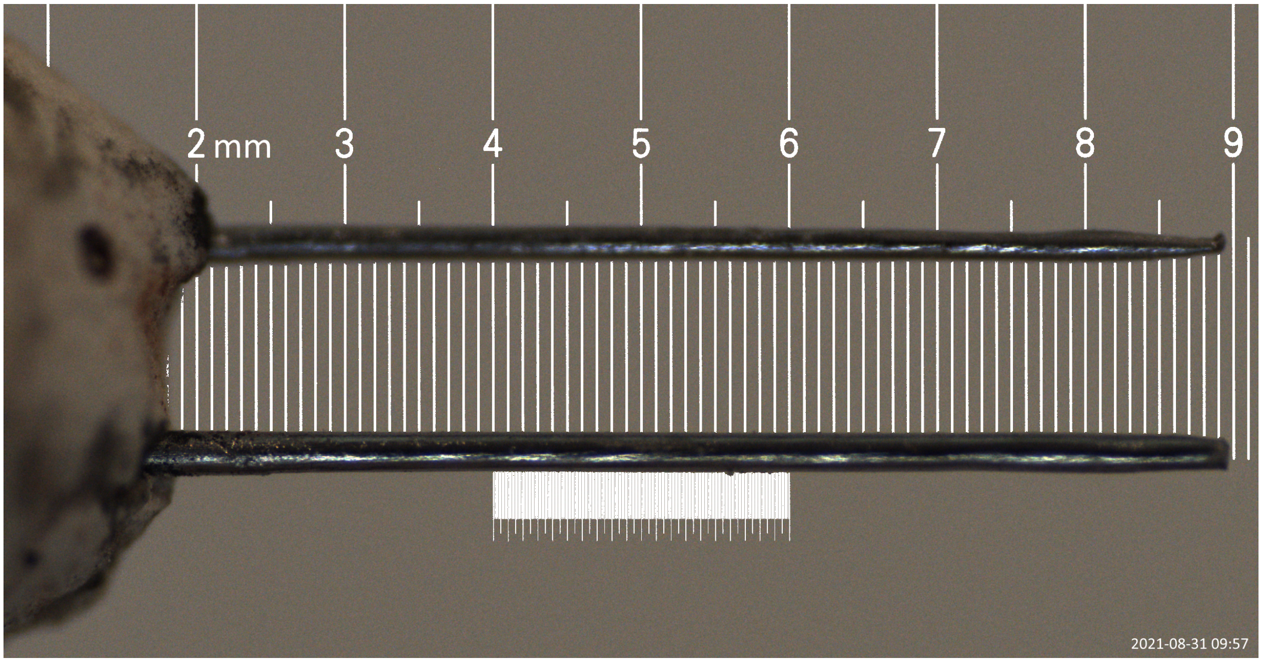

Fig. 2.11: An image of the used Langmuir double probe taken with a tele-microscope. Note that the measurement scale on the ruler is in millimeters. The pictures of the ruler and probe were taken separately and later edited into a single picture to determine the probe dimensions.

In this work, a Langmuir double probe is used to measure the plasma parameters inside a plasma source similar to a RIT-10. The probe is shown in Fig. 2.11. The picture was taken with a tele-microscope, which is essentially a high resolution camera with an aspherical lens to avoid image distortion. The probe image can be overlaid with an image of a calibrated ruler to determine its dimensions. From Fig. 2.11, the probe length was determined at $6.9\,\mathrm{mm} \pm 0.1\,\mathrm{mm}$. The probe wire radius was determined at $0.125\,\mathrm{mm} \pm 0.0125\,\mathrm{mm}$ and the spacing in between the wires at $1.425\,\mathrm{mm} \pm 0.025\,\mathrm{mm}$. After renewing the probe insulation (left in Fig. 2.11), the probe dimensions are still within the given error range.

2.6.1 Data pre-processing

As some measurements contained spikes or jumps in the measured probe current, all measurements were investigated by eye before an automated evaluation was carried out. First, the spikes in the data were identified and removed as shown in Fig. 2.12. To do this, a moving average over 11 probe current points is determined according to

$$\overline{I}(U_i) = \frac{1}{11} \sum_{j=i-5}^{i+5} I_{\mathrm{probe}}(U_j). \tag{2.16}$$

The derivatives of both the measured and the averaged probe currents are determined and their quadratic deviation relative to the maximum probe current is compared to the threshold

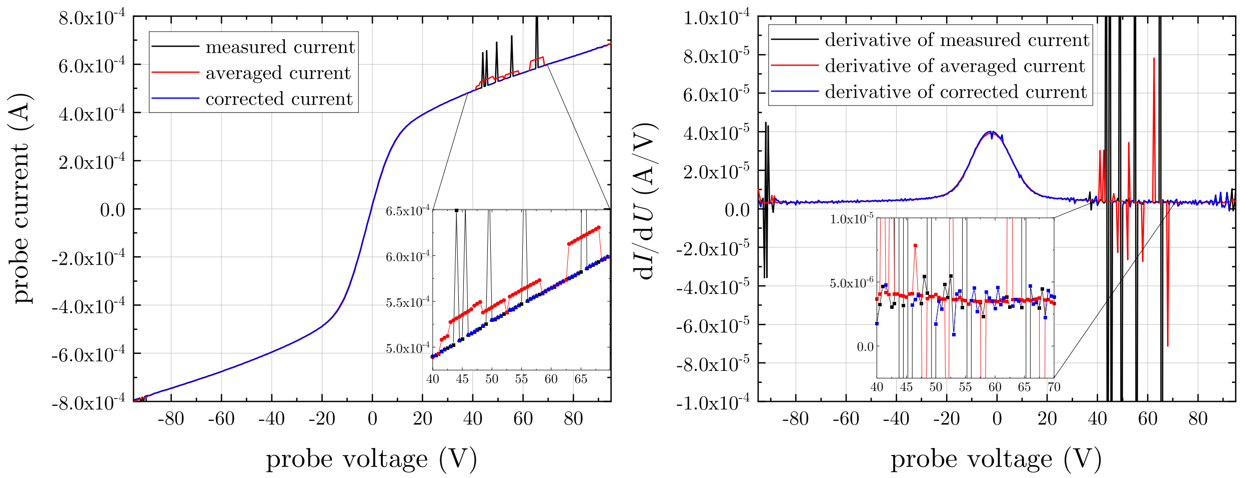

Fig. 2.12: An example of the method used to reject spikes in the measured Langmuir probe current. On the left, the measured curve (black) shows some spikes. In the averaged curve (red), these spikes are less prominent. After applying the spike rejection algorithm, the blue curve still contains the relevant data points, while the spikes are removed. On the right, the derivatives of the original (black), averaged (red) and the corrected (blue) probe current characteristics are shown. Here, the spikes are strongly pronounced and the difference to the average curve can be detected easily.

value x according to

$$\left(\frac{\frac{\mathrm{d}}{\mathrm{d}U}I_{\mathrm{probe}}(U)-\frac{\mathrm{d}}{\mathrm{d}U}\overline{I}(U)}{\max(|I_{\mathrm{probe}}(U)|)}\right)^2 < x. \tag{2.17}$$

All probe current points for which Eq. 2.17 is not fulfilled are not considered for the proceeding evaluation. To ensure that only spikes are removed and not too much of the data, the value for the threshold parameter x is chosen manually for each measurement, typically between $2.5 \cdot 10^{-5}$ and $5 \cdot 10^{-4}$ depending on the signal to noise ratio. The resulting curve shown in Fig. 2.12 contains the relevant data points without modification to their values, while the spikes have been removed and can no longer distort the following fits.

There are also other sources that can disturb the evaluation. An example is the sudden jump of the probe current shown in Fig. 2.13. These jumps are likely caused by accumulated contamination between the probe wires that starts to become slightly conductive, thus increasing the effective probe area or allowing current to flow directly between the electrodes. Such effects occur at higher voltages. While the spike rejection in Fig. 2.12 detects these jumps and removes the corresponding data points (which do not fulfill Eq. 2.17) from the curve, the other data points after the current jump are still considered. Therefore, the evaluation region is reduced so these jumps are not included anymore as indicated by the vertical dashed line in Fig. 2.13. Due to the spike rejection executed beforehand, several data points in a row are missing in the vicinity of a jump. To automatically find a jump an algorithm searches for these gaps and shifts the limits of the evaluation region to the gap with the lowest voltage. Afterwards a confirmation by eye of the limits ensures that no problematic

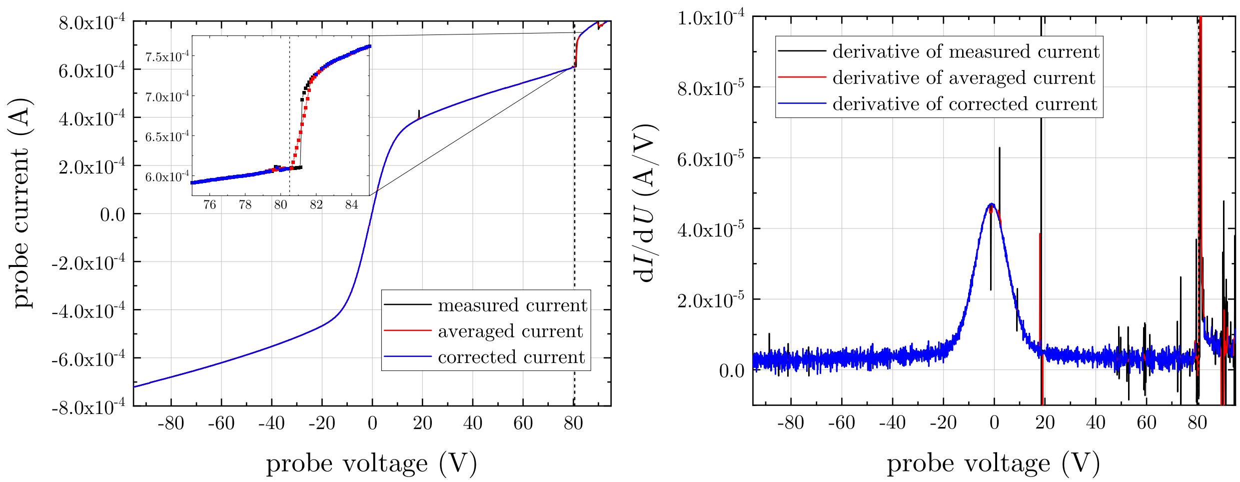

Fig. 2.13: An example of the method used to reject jumps in the measured Langmuir probe current. On the left, the measured curve (black) shows a sudden jump in current. On the right the derivative of the characteristic is shown. The vertical dashed line marks the new upper limit, in which the Langmuir characteristic will be evaluated. The initial limits are found automatically but can be adjusted by hand afterwards.

regions are left in the evaluation range.

2.6.2 Data evaluation

Now that the data is preprocessed, the actual evaluation is performed automatically by an algorithm. First, an electron temperature is guessed $T_{\mathrm{e,guess}}$. As the shape of the measured curve scales with T_{e} along the U-axis and with the ion saturation current I_{sat} along the I-axis, we use $T_{\mathrm{e,guess}}$ to determine the fitting regions. The ion saturation region is assumed to start above 6.5 times $T_{\mathrm{e,guess}}$ in eV. So the positive ion saturation region is fitted between $(6.5 \cdot T_{\mathrm{e,guess}}/\mathrm{eV})\mathrm{V}$ and the upper evaluation limit. Accordingly, the negative ion saturation region is fitted between $(-6.5 \cdot T_{\mathrm{e,guess}}/\mathrm{eV})\mathrm{V}$ and the lower evaluation limit. The electron temperature is determined by the maximum slope of the curve at $U \approx 0$. The fitting region is set to $\pm(2.125 \cdot T_{\mathrm{e,guess}}/\mathrm{eV} - 0.0625 \cdot (T_{\mathrm{e,guess}}/\mathrm{eV})^2)\mathrm{V}$. These relations were determined according to theoretical curves generated using

$$I(U) = I_{\mathrm{sat}} \cdot \tanh\left(\frac{U}{2 \cdot (T_{\mathrm{e}}/\mathrm{eV})}\right) + a \cdot U \tag{2.18}$$

where a is the slope of the saturation region.

With some probes, the UI-characteristic is shifted and therefore not symmetrical around zero. This can be caused by a probe bias and may be corrected by centering the curve at zero. The algorithm does this centering by determining the zero-crossing of the curve and subtracting it from all voltage values. Afterwards, the positive and negative saturation regions are fitted with a linear function and $\pm I_{\mathrm{sat}}$ are determined as the y-axis intercepts. Since we assume the absolute values of $\pm I_{\mathrm{sat}}$ to be equal, $(|I_{\mathrm{sat},+}| - |I_{\mathrm{sat},-}|)/2$ is subtracted from all current values. This process of shifting the curve left/right and then up/down is repeated until

$$\frac{|I_{\text{sat},+}| - |I_{\text{sat},-}|}{|I_{\text{sat},+}| + |I_{\text{sat},-}|} < 10^{-5} \tag{2.19}$$

or 40 iterations are reached. Both ion saturation currents should be equal now. For the probe shown in Fig. 2.11, the data was already centered so the algorithm performed only minor adjustments.

The fit parameters from the last iterations are used to correct for the sheath expansion. Here the slope of the negative ion saturation region fit a_- is subtracted from the negative part of the curve, while the slope of the positive region fit a_+ is subtracted from the positive part of the curve

$$I_{\text{corrected}}(U) = \frac{I(U) - \begin{cases} a_- \cdot U & U < 0 \\ a_+ \cdot U & U \geq 0 \end{cases}}{I_{\text{sat}}} \tag{2.20}$$

while everything is normalized by dividing by the ion saturation current I_{sat}. Eq. 2.20 uses two different slopes, as the two probe wires are not always perfectly identical in shape and dimensions as it can be seen in Fig. 2.11. This can cause slightly different slopes of the saturation regions, which can lead to errors if they are not considered.

To obtain T_{e}, the typical procedure would be to apply an atanh on $I_{\text{corrected}}(U)$ and determine the slope at $U = 0$ by a linear fit

$$\frac{1}{T_{\text{e}}/\text{eV}} = 2 \cdot \frac{\mathrm{d}}{\mathrm{d}U} \operatorname{atanh}(I_{\text{corrected}}(U)) \bigg|_{U=0} . \tag{2.21}$$

Applied to data that follow the theoretical ideal curve of Eq. 2.18 this approach yields good results, as the application of the atanh function actually results in a linear curve. In reality, slight deviations from this ideal behavior occur, so atanh does not necessarily yield a linear function. Here, different approaches were tested on a set of measured and generated data. The first important point is that atanh is practically equal to its argument x close to $x = 0$

$$\operatorname{atanh}(x) = \frac{1}{2} \ln\left(\frac{1+x}{1-x}\right) \approx x \quad \text{if} \quad x \approx 0. \tag{2.22}$$

This means that it is not necessary to apply atanh in the first place, as the slope at $x \approx 0$ is unchanged. Other options tried in addition to the standard procedure were a linear fit of $I_{\text{corrected}}$, a third degree polynomial fit of $I_{\text{corrected}}$, a second degree polynomial fit of $\frac{\mathrm{d}}{\mathrm{d}U} I_{\text{corrected}}$ and $\frac{\mathrm{d}}{\mathrm{d}U}\operatorname{atanh}(I_{\text{corrected}})$ as well as a Gaussian fit of $\frac{\mathrm{d}}{\mathrm{d}U} I_{\text{corrected}}$. The most robust evaluation procedure was the third degree polynomial fit of $I_{\text{corrected}}$, as it showed only a small dependence on the choice of the fitting range (tested on real data) as well as the noise level (tested on generated data according to Eq. 2.18) when compared to the other options. This polynomial $p(U) = \sum_{i=0}^{3} a_i U^i$ can follow the slightly curved parts at the edges of the fitting region without affecting the relevant part around $U = 0$. The maximum slope can then be easily determined as $s_{\max} = a_1 - a_2^2/(3a_3)$. Note that no assumption has to be made that the maximum slope is exactly at $U = 0$, which is not necessarily the case. The position of the maximum slope inherently results from the polynomial fit. In agreement with Eq. 2.21 the electron temperature is

$$T_\mathrm{e}/\mathrm{eV} = \frac{1}{2 \cdot s_\mathrm{max}} \tag{2.23}$$

The electron density n_e is now determined as

$$n_\mathrm{e} = \frac{I_\mathrm{sat}}{\mathrm{e}A_\mathrm{probe}} \cdot \sqrt{\frac{m_\mathrm{ion}}{\mathrm{k}T_\mathrm{e}}} \tag{2.24}$$

where A_probe is the surface area of the probe wires and m_ion is the mass of the plasma ions.

Initially, the fit boundaries were determined using a guessed electron temperature $T_\mathrm{e,guess}$, which is probably not equal to the determined T_e. The algorithm starts over and over again using T_e as the new $T_\mathrm{e,guess}$, until $|T_\mathrm{e,guess} - T_\mathrm{e}| < 0.01$. This iterative evaluation process ensures, that the fit boundaries are chosen correctly for each measurement. The full algorithm is schematically shown in Fig. 2.14

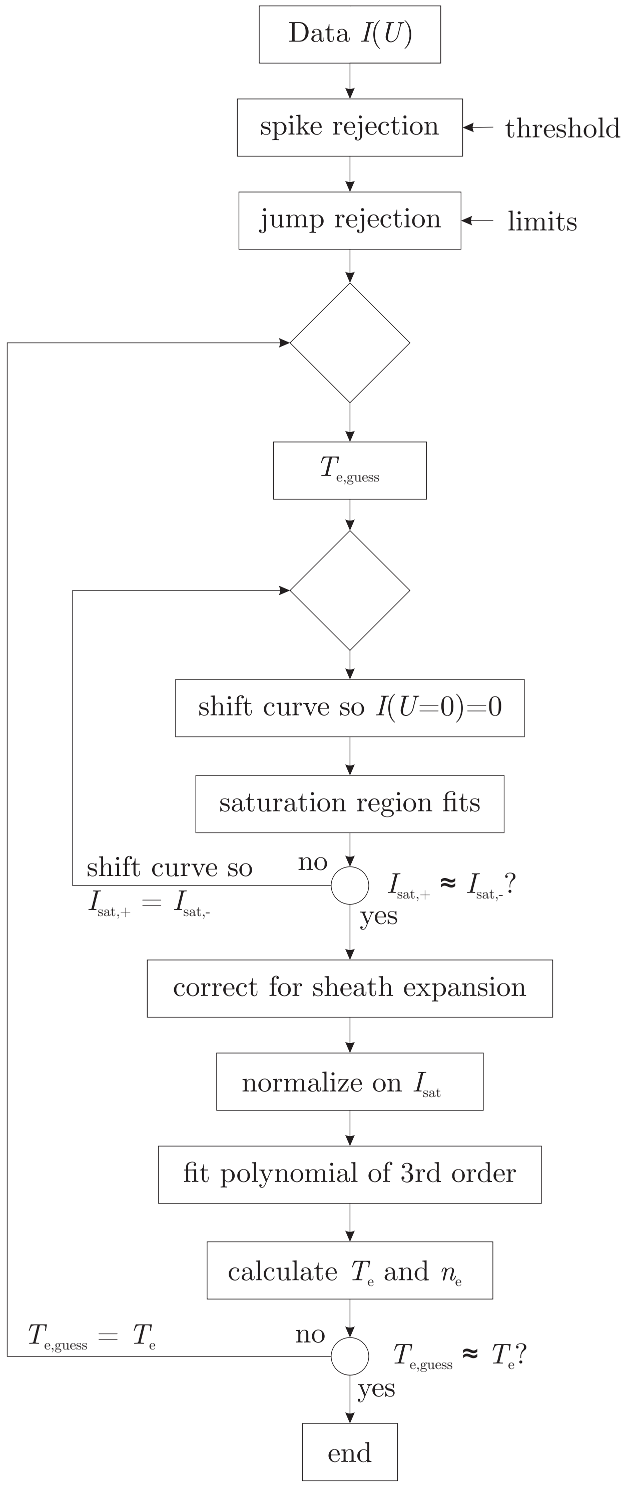

Fig. 2.14: A flow chart of the algorithm that performs the evaluation of Langmuir double probe measurements.

3. IDEA BEHIND COMBINING OES VIA PCA WITH LANGMUIR DIAGNOSTICS

Optical emission spectroscopy is a non-invasive measurement technique, that can be applied for plasma based ion thrusters [30, 34, 35, 37–41]. As the emission line intensities result from the excitation, changes in line intensities mean changes in the excitation. This means that the plasma parameters have to change, since the excitation directly results from the plasma parameters. So, there is a relation between the optical emission spectrum and the state of a plasma, that can be utilized to determine the plasma parameters non-invasively from an OES measurement.

A plasma's optical emission spectrum can be theoretically modeled on a microscopic level with sufficient knowledge of the relevant processes involved. This has been done in numerous works, for example for argon [45–58] and xenon plasmas [30, 34, 35, 37–40, 55, 59–61]. An example of the implementation of such a model is shown in Fig. 3.1 [42]. Here, the plasma parameters are inserted into a plasma model from which the occupation of the electronic states of the atoms and ions is derived. By using the transition matrix elements, the theoretical optical emission spectrum $S_{\mathrm{theo}}(\lambda)$ is generated and compared with a measured spectrum $S'(\lambda)$. The plasma parameters used as input for the model are then adapted until the two spectra agree.

These models, however, are in need of a database containing the relevant microscopic parameters like excitation cross-sections, electronic states of the plasma species and transition matrix elements etc. These microscopic parameters are not always available in the necessary detail and are difficult to determine by experiment or to predict by theory [80–85].

These issues are usually accepted, as OES has the advantage of being a non-invasive measurement technique and knowledge on plasma parameters can give valuable insights into the thrusters. In this work, a new technique has been developed to determine plasma parameters from optical emission spectra without the need for theoretical microscopic models. Instead, a measurement-based empirical correlation is determined by linking the results from OES measurements and Langmuir diagnostics on a reference setup similar to the thruster under investigation. Here, a PCA is used in order to simplify the measured emission spectra while preserving their most relevant features. The plasma parameters and PCA results are then connected to create a correlation that describes the plasma parameters as functions of the spectra. An optical emission spectrum on a plasma similar to the reference plasma can then be simplified using the results of the reference PCA. The found correlations can then be applied to these simplified spectra to yield the corresponding plasma parameters. The application of the empirical correlation method is shown shematically in Fig. 3.2 [42]. In principle, this method can be employed for all propellants or propellant mixtures. So far, it has been

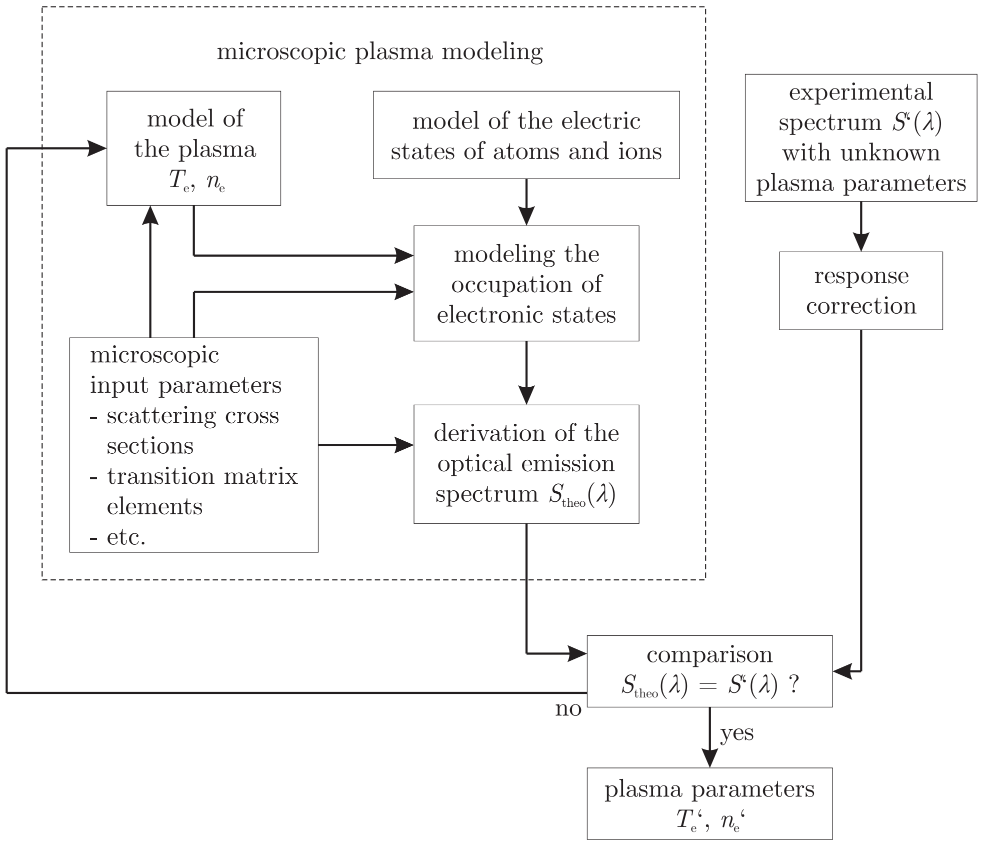

Fig. 3.1: A schematic flow chart of a possible theoretical microscopic plasma model that calculates the optical emission spectrum $S_{\text{theo}}(\lambda)$ from the plasma parameters T_e and n_e. The calculated spectrum is then compared to a measured spectrum $S'(\lambda)$ to determine the corresponding plasma parameters.
The graphic is taken from Ref. 42 with kind permission of the European Physical Journal (EPJ).

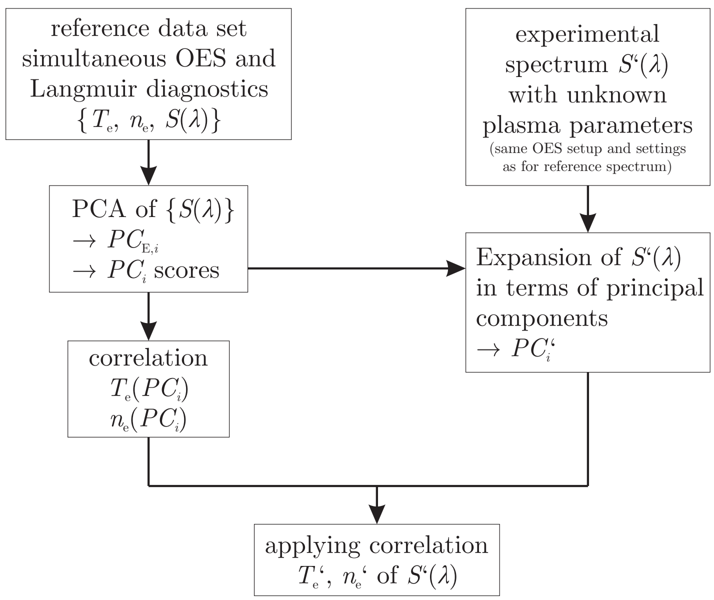

Fig. 3.2: A schematic flow chart of the empirical correlation method. A measured reference data set consisting of OES measurements and plasma parameters is needed from which a correlation between both measurements is derived. A PCA is used in assistance to simplify the OES measurements for the correlation. This correlation can then be applied to the PCA scores of a measured spectrum $S'(\lambda)$ to yield the corresponding plasma parameters.
The graphic is taken from Ref. 42 with kind permission of the European Physical Journal (EPJ).

tested for xenon, krypton and mixtures of the two [43]. Furthermore, the approach has been used to assess the plasma parameters of an operating thruster [90]. As it has no need for theoretical modeling nor any knowledge on the microscopic parameters of the plasma species, this method is a versatile alternative to the modeling approach.

4. MAIN RESULTS

4.1 *Publication 1: Non-invasive assessment of plasma parameters inside an ion thruster combining optical emission spectroscopy and principal component analysis [42] (see attachment 1)*

In this work, a new approach was taken to determine plasma parameters non-invasively by employing a correlation between OES and Langmuir measurements. Modeling of the plasma can be bypassed entirely, since a comparison with direct measurements of the plasma parameters is carried out in the reference measurements and, thus, the measured optical emission spectra and plasma parameters can also be correlated directly. Once a one-to-one correspondence between plasma parameters and optical measurements is established, it can be used to directly relate an optical emission spectrum of the sample under study, e. g., the thruster's plasma, with the plasma parameters of its current operational state. In other words, the direct measurement of plasma parameters with a Langmuir probe is no longer necessary and the determination of the plasma parameters is entirely non-invasive.

To establish such a correlation, an invasive Langmuir double probe measures the plasma parameters, while a spectrometer is used to measure the optical emission simultaneously. A reference series is recorded, in which the operating parameters (here rf input power and propellant gas flow) are varied over a wide rage of settings. The spectra are reduced to their most prominent features by performing a principal component analysis [44]. This yields a 2D map in which each spectrum is represented by a single point and the spectra are separated by the varied input parameters power and gas flow. The resulting principal component scores are assigned to their corresponding plasma parameters. A 3D-polynomial is used as a fit function that describes a specific plasma parameter as a function of the PCA scores, i. e., the simplified optical emission spectra. This can be done for all plasma parameters to obtain the described one-to-one correspondence between the spectra and the plasma parameters $T_\mathrm{e}(PC_1, PC_2)$ and $n_\mathrm{e}(PC_1, PC_2)$.

Such a correlation of OES and plasma parameters can then be applied on a similar plasma. In this work, the correlations were applied to time resolved measurements on the same setup to examine the behavior of the plasma parameters during the rf-cycle, which is described in more detail in chapter 4.3.2.

4.2 Publication 2: Combination of optical emission spectroscopy and multivariate data analysis techniques as a versatile non-invasive tool for characterizing xenon/krypton mixed gas plasma inside operating ion thrusters [43] (see attachment 2)

Xenon is the currently preferred propellant for plasma based electric propulsion thrusters due to its high mass, chemical inertness and relatively low ionization energy of 12.13 eV [74]. However, xenon is quite expensive as it is a rare resource [18,19]. Therefore, finding suitable alternative propellants is of great interest. One of these alternatives is the lighter noble gas krypton [5, 6, 9, 11–13]. Another candidate is iodine as it has a high molecular mass and is an easily vaporized solid with low ionization energy [15, 16].

A thruster has to be characterized with the intended propellant, which is not an issue with electrical probes. The correlations between OES measurements and plasma parameters, on the other hand, are only valid for a single propellant. In case of theoretical microscopic models, a new model has to be created for each propellant, using the corresponding microscopic parameters like cross sections. Of course, an empirically found correlation is also only valid for a single propellant. However, the empirical approach can be easily adapted to other propellants, as no microscopic parameters are required.

Here, we explored the viability of the empirical approach for the two propellants xenon and krypton as well as for mixtures of these two gases. Compared to the initial work [42], the ranges of the rf input power and gas flow were increased to get a broader map of parameters. The OES measurement was now performed on the position of the Langmuir probe by focusing the light onto a fiber. The xenon gas flow and rf input power were varied in several measurement series with different constant krypton gas flows.

Again, we performed a PCA on the OES measurements for each individual measurement series. It could be seen that the resulting PCA scores formed a 3D-surface. A projection plane has been defined between one of the PCA axes and a vector $\vec{v}$, which is a linear combination of the remaining two PCA axes, to avoid overlapping data points when observing the PCA results in just two dimensions. The individual spectra could be separated well in these projected 2D-map of PCA scores. The projected scores x_{PC} and x_{v} were then assigned to the plasma parameters and a 3D-polynomial fit yielded the correlation functions $T_{\mathrm{e}}(x_{\mathrm{PC}}, x_{\mathrm{v}})$ and $n_{\mathrm{e}}(x_{\mathrm{PC}}, x_{\mathrm{v}})$. In case of krypton, this projection method was not applicable, as no projection plane could be found in which the 3D data points did not overlap. Here, arbitrary variables u and v were assigned to the individual data points. Each principal component and the individual plasma parameters were then described as functions of these variables by a 3D-polynomial fit, yielding $PC_i(u, v)$, $T_{\mathrm{e}}(u, v)$ and $n_{\mathrm{e}}(u, v)$. Now, the variables u and v have to be found to determine the plasma parameters from an OES measurement, which can be done by minimizing the sum of the relative quadratic deviations of the measured scores and the scores calculated using $PC_i(u, v)$. Of course, the tree dimensional PCA scores could be used directly and the plasma parameters could be described by a 4D-polynomial fit function. This is, however, hard to visualize.

Due to the successful correlation between OES and plasma parameters for more complex plasmas in this study, it can be assumed, that the empirical correlation method is also applicable to other propellants and propellant mixtures.

4.3 Preliminary additional experimental results

4.3.1 Publication 3: Plasma parameter measurement on a RIT-10 using empirical correlations between non-invasive optical emission spectroscopy and Langmuir diagnostics [90] (see attachment 3, not peer-reviewed)

The correlation method was initially only tested on a RIT-like setup. While the discharge chamber and rf-coil were parts also used in RITs, there was no extraction grid system present. For easy access, the setup was placed outside the vacuum with only the inside of the discharge vessel being evacuated.

As the correlations between plasma parameters and optical emission spectra in previous works were quite successful [42, 43], the setup was advanced since. Here, a new correlation measurement series was performed on a RIT-10 laboratory prototype [90]. This thruster was equipped with a modified gas inlet that allows the insertion of a Langmuir double probe. Since the thruster has to be operated under vacuum conditions, the OES measurement was realized through a window in the vacuum chamber with view on the grid system. The light from the plasma was focused on a fiber by using a lens, similar to the previous experiments in Ref. 43.

First, a correlation measurement series was performed by simultaneous measurement of OES and plasma parameters while the thruster operated in stand-by, i. e., with ignited plasma but without ion beam extraction. Since ion beam extraction on a RIT is realized by applying high voltages to the screen and accel grids, the plasma itself is biased by the screen grid voltage due to direct contact. This, however, also biases the Langmuir probe inside the thruster as well as the measurement unit connected to it. So, applying a screen grid voltage of 1700 V is not possible while the measurement unit is connected, as it can only be biased by 250 V towards ground. After the correlation measurement series, the Langmuir probe was disconnected from the measurement unit. This allowed for thruster operation with ion beam extraction. Several performance curves were measured for different beam currents, i. e., variation of propellant gas flow with constant beam current. The OES measurements were performed at each point of operation.

The spectra from the correlation series were again simplified using a PCA, which yielded a good separation of spectra by rf input power and gas flow like in previous studies. The PCA scores were assigned to the corresponding plasma parameters and a 3D-polynomial fit yielded the correlation functions like in previous studies. The PCA scores of the ion beam extraction measurement series were then calculated using the PCA eigenvectors from the PCA of the correlation series. As the resulting scores fall into the area mapped by the correlation series, the correlations can be applied. The absolute values have yet to be verified, but the resulting electron temperatures increase with decreasing gas flow, while the electron densities increased with higher beam currents, which is the expected behavior for a RIT [2, 75, 91].

4.3.2 Time-resolved studies

Being excited by a rf signal, it can be observed that the plasma follows this excitation [42, 92–94].Since the rf signal is an AC-excitation, the magnetic field in the rf-coil changes direction periodically. This causes the induced rotational electric field to change direction, too. As a consequence, the absolute electric field, which is responsible for the acceleration of the free electrons in the plasma, reaches its maximum value twice during each rf cycle. Therefore, the plasma oscillations will change with twice the rf frequency.

This implies that electron temperature and, therefore, the plasma potential are subject to periodic oscillations. As screen grid erosion is linked to the plasma potential, oscillations in the plasma potential might exceed the threshold for sputtering periodically, while the average is still be below the threshold. However, as the electron density oscillates, too, an estimation of the sputtering gets complicated. If the electron temperature and density oscillate with the same phase, i. e., both parameters increase and decrease in sync, the real sputtering will be higher than estimated with averaged values. On the other hand, if electron temperature and density oscillate with a 180° phase shift, i. e., the density decreases while the temperature increases and vise versa, the averaged estimation may also overestimate the real sputtering. In this case, the increase in sputtering yield due to higher electron temperature and, therefore, higher plasma potential competes with the smaller amount of ions, which result from the lower electron density. Which of the described cases is present in a thruster depends on the specific operational point.

While there is benefit in knowing the time-resolved plasma parameters in a thruster, measuring these parameters is not trivial. As the measurement times have to be short in comparison with the rf-signal, disturbances from the rf cannot be averaged in electric probes. As an alternative, optical emission spectroscopy can provide high time resolution and is not disturbed by the rf-signal. Typical excitation frequencies of around 1 to 2 MHz correspond to rf periods of 0.5 to 1.0 μs. This time frame is significantly longer than the relaxation times of some optical transitions of the regularly used propellant gas xenon and also krypton, which can be in the region of 20 to 100 ns [95]. If the relaxation times are short compared to the rf period, we assume that the optical transitions react almost instantaneous to the changes in the plasma during the rf period. With our ICCD, these fast lines can be observed with sufficiently high time resolution to monitor their behavior over the course of an rf cycle [42].

Like anticipated before, the oscillation of the spectral transitions with twice the rf frequency could be observed. Under the assumption that the excitation and relaxation of the plasma atoms and ions are in equilibrium, it is possible to determine time-resolved plasma parameters by employing correlations from a suited reference plasma like for a cw OES measurement. Oscillations in electron density could be observed for all measurements (amplitudes $\approx 30\,\%$ of average), while oscillations of the electron temperature were only visible for some measurements (amplitudes up to 0.5 eV), mainly for low average electron temperatures (< 3 eV). The phase shift between density and temperature was 180° for most measurements with visible oscillations. Phase shifts of 0° were also observed, however, with much smaller amplitudes (< 0.1 eV). Of course, the viability of this assumption depends on the spectral transitions chosen for the measurement and correlation and has yet to be verified.

4.3.3 Spatial plasma mapping

A real thruster is not a point source, so the plasma has a certain volume. The plasma parameters are not constant within this volume [70, 96–99].

This means, that the plasma meniscus at the extraction grids is probably not the same for all extraction channels. So, in theory a slight defocusing might occur, which might be interpreted as charge exchange losses, thus causing a faster erosion of the affected channels. Differences in electron temperature and density may also result in corresponding differences in screen grid sputtering. So, spatially resolved measurements are necessary to fully characterize a thruster.

Electrical probes can only measure the plasma parameters at a certain position. Such an electrical probe has to be moved or multiple probes need to be installed to map the plasma parameters over the whole plasma volume. In EP-thrusters with open ionization chambers like Hall effect thrusters, a movable probe can be realized quite easily [25, 26]. In a RIT, a movable probe is not easily possible, as the plasma vessel is closed off by the grid system. Nevertheless, such measurements are not impossible and were performed by, e. g., Schäfer [96] on a RIT-like setup. While multiple probes can be installed in a RIT, it results in larger modifications of the thruster and becomes increasingly difficult for smaller thrusters. Beam diagnostics for spatially resolved measurements usually have to be close to the thruster and, therefore, have to withstand continuous high energy ion bombardment. The influence of beam diagnostics in the near-field of the thruster can also make the measurement more complicated.

Using the correlation method described in this work, plasma parameters can also be obtained from a spatially resolved OES measurement. An OES setup can be placed in front of the thruster on a movable platform similar to beam diagnostics like those in Ref. 22. The emission spectrum can be measured easily even with low intensities, as the detector is not affected by electrical noise. Therefore, the setup can be placed further away from the thruster than other near-field detectors. As light is emitted in all directions, it might be possible for some thrusters to place the OES setup outside of the ion beam to further reduce interactions between thruster and diagnostics. If a suitable window is equipped to the vacuum chamber, the OES setup may even be placed outside the vacuum. Spatial resolved optical emission spectra of a plasma can be obtained by moving the focus of the optical setup inside the thruster, even for closed thrusters like RITs. The spectra can then be used to determine plasma parameters by employing correlations from a suited reference plasma.

5. CONCLUSION

A new measurement-based empirical method for correlating optical emission spectroscopy and plasma parameters without the need for theoretical microscopic models has been developed in this work. Measurements of the optical emission spectrum via a spectrometer as well as plasma parameters via a Langmuir double probe were performed simultaneously on a plasma inside a RIT-10 discharge chamber. The measured spectra were simplified by a principal component analysis. This allowed to reduce the spectra to a single point in a two dimensional coordinate space in which the spectra are separated by their main differences. A three dimensional polynomial fit was used to describe the plasma parameters as functions of the PCA results. This correlation can then be applied on optical emission spectra of similar plasmas to determine their plasma parameters non-invasively.

Here, the PCA yielded a 2D map of the spectra, in which the spectra are sufficiently separated by propellant gas flow and rf input power. The correlation fit describes the plasma parameters as functions of the PCA scores. Applying the correlation to time resolved OES measurements showed that the plasma parameters might oscillate during the rf-cycle, which has, however, yet to be verified. Correlation measurements using different propellants and mixtures all yielded very similar results. Therefore, it can be optimistically said that this method is likely to work for other propellants and mixtures as well. In measurements on a thruster, a correlation was established during standby operation, which was afterwards applied to OES measurements taken during ion beam extraction. The resulting PCA scores of the extraction measurements fell into the area mapped during standby operation, meaning that the correlations can be applied as the spectra are similar. The resulting plasma parameters showed reasonable trends with the absolute values yet to be verified.

The empirical correlation between plasma parameters and optical emission spectra showed to be a versatile tool to determine plasma parameters non-invasively. It has clear advantages over theoretical microscopic models, as it easily works with alternative propellants and does not require any prior knowledge on the microscopic parameters of the plasma species.

In future studies, the empirical correlation approach may be employed to determine plasma parameters non-invasively in ion thrusters from the development phase up to the qualification for space. The presented method will contribute to a deeper characterization and understanding of ion thrusters in which invasive Langmuir probes may not be used. Due to the easy adaptability on other propellants and mixtures, as well as the simple procedure, this method can be used instead of theoretical microscopic modeling of spectra, also when no sufficient database or simulation of microscopic input parameters is available. As OES can be performed with high spatial and time resolution, plasma parameter distributions and their periodic time behavior during the rf cycle may be investigated further using the proposed method of non-invasively determining plasma parameters inside ion thrusters.

BIBLIOGRAPHY

[1] Wilfried Ley, Klaus Wittmann, and Willi Hallmann. Handbuch der Raumfahrttechnik. *Carl Hanser Verlag GmbH & Co. KG*, München, 5th edition, January 2019.

[2] Dan M. Goebel and Ira Katz. Fundamentals of Electric Propulsion. *John Wiley & Sons*, Hoboken, 1st edition, March 2008.

[3] Stéphane Mazouffre. Electric propulsion for satellites and spacecraft: established technologies and novel approaches. *Plasma Sources Science and Technology*, 25(3):033002, April 2016.

[4] K. Holste, P. Dietz, S. Scharmann, K. Keil, T. Henning, D. Zschätzsch, M. Reitemeyer, B. Nauschütt, F. Kiefer, F. Kunze, J. Zorn, C. Heiliger, N. Joshi, U. Probst, R. Thüringer, C. Volkmar, D. Packan, S. Peterschmitt, K. T. Brinkmann, H.-G. Zaunick, M. H. Thoma, M. Kretschmer, H. J. Leiter, S. Schippers, K. Hannemann, and P. J. Klar. Ion thrusters for electric propulsion: Scientific issues developing a niche technology into a game changer. *Review of Scientific Instruments*, 91(6):061101, June 2020.

[5] K. H. Groh, H. W. Löb, and H. W. Velten. Performance data comparison of the inert gas RIT 10. *Journal of Spacecraft and Rockets*, 21(4):360–365, July 1984.

[6] H. Bassner and K. H. Groh. A 50 mN RIT Thruster Assembly for Application to Heavy Geostationary-Satellites. In *31st AIAA/ASME/SAE/ASEE Joint Propulsion Conference & Exhibit*, AIAA 95-3068, San Diego, CA, July 1995.

[7] Rainer A. Dressler, Yu-Hui Chiu, and Dale J. Levandier. Propellant alternatives for ion and Hall effect thrusters. In *38th Aerospace Sciences Meeting and Exhibit*, AIAA 2000-0602, Reno, NV, January 2000.

[8] B. A. Arkhipov, A. I. Koryakin, V. M. Murashko, A. N. Nesterenko, I. A. Khoromsky, V. Kim, V. I. Kozlov, G. A. Popov, and A. I. Skrylnikov. The results of testing and effectiveness of the Kr-Xe mixture application in SPT. In *27th International Electric Propulsion Conference*, IEPC-01-064, Pasadena, CA, October 2001.

[9] Vladimir Kim, Garry A. Popov, Vyacheslav Kozlov, Alexander Skrylnikov, and Dmitry Grdlichko. Investigation of SPT Performance and Particularities of it's Operation with Kr and Kr/Xe Mixtures. In *27th International Electric Propulsion Conference*, IEPC-01-065, Pasadena, CA, October 2001.

[10] O. S. Tverdokhlebov and A. V. Semenkin. Iodine Propellant for Electric Propulsion - To Be Or Not To Be. In *37th AIAA/ASME/SAE/ASEE Joint Propulsion Conference & Exhibit*, AIAA 2001-3350, Salt Lake City, UT, July 2001.

[11] A. I. Bugrova, A. I. Morozov, A. S. Lipatov, A. M. Bishaev, V. K. Kharchevnikov, and M. V. Kozintseva. Integral and spectral characteristics of ATON stationary plasma thruster operating on krypton and xenon. In *28th International Electric Propulsion Conference*, IEPC-03-366, Toulouse, France, March 2003.

[12] Jesse A. Linnell and Alec D. Gallimore. Internal plasma potential measurements of a Hall thruster using xenon and krypton propellant. *Physics of Plasmas*, 13(9):093502, September 2006.

[13] Jesse A. Linnell and Alec D. Gallimore. Efficiency Analysis of a Hall Thruster Operating with Krypton and Xenon. *Journal of Propulsion and Power*, 22(6):1402–1418, November 2006.

[14] Nazareno Fazio, Stephen Gabriel, and Igor O. Golosnoy. Alternative propellants for gridded ion engines. In *Space Propulsion Conference*, SP2018_00102, Sevilla, Spain, May 2018.

[15] Kristof Holste, Waldemar Gärtner, Daniel Zschätzsch, Steffen Scharmann, Peter Köhler, Patrick Dietz, and Peter J. Klar. Performance of an iodine-fueled radio-frequency ion-thruster. *The European Physical Journal D*, 72(1):9, January 2018.

[16] Patrick Dietz, Waldemar Gärtner, Quirin Koch, Peter E. Köhler, Yan Teng, Peter R. Schreiner, Kristof Holste, and Peter J. Klar. Molecular propellants for ion thrusters. *Plasma Sources Science and Technology*, 28(8):084001, August 2019.

[17] Nazareno Fazio, Stephen Gabriel, Igor O. Golosnoy, and Birk Wollenhaupt. Mission Cost for Gridded Ion Engines using Alternative Propellants. In *36th International Electric Propulsion Conference*, IEPC-2019-831, Vienna, Austria, September 2019.

[18] Richard P. Welle. Availability Considerations in the Selection of Inert Propellants for Ion Engines. In *21th International Electric Propulsion Conference*, AIAA 90-2589, Orlando, FL, July 1990.

[19] Richard Welle. Xenon and krypton availability for electric propulsion - An updated assessment. In *29th Joint Propulsion Conference & Exhibit*, AIAA 93-2401, Monterey, CA, June 1993.

[20] G. Karabadzhak, Y.-H. Chiu, S. Williams, and R. Dressler. Hall thruster optical emission analysis based on single collision luminescence spectra. In *37th AIAA/ASME/SAE/ASEE Joint Propulsion Conference & Exhibit*, AIAA 2001-3893, Salt Lake City, UT, July 2001.

[21] Stéphane Mazouffre. Laser-induced fluorescence diagnostics of the cross-field discharge of Hall thrusters. *Plasma Sources Science and Technology*, 22(1):013001, November 2012.

[22] Fabrizio Scortecci, Damiano Pagano, Carsten Bundesmann, Christoph Eichhorn, Frank Scholze, Daniel Spemann, Hans Leiter, Holger Kersten, Richard Blott, Stephane Mazouffre, et al. AEPD System as a Standard On-ground Tool for Electric Propulsion Thrusters. In *35th International Electric Propulsion Conferce*, IEPC-2017-33, Atlanta, Georgia, October 2017.

[23] Daren Yu, Tianhang Meng, Zhongxi Ning, and Hui Liu. Confinement effect of cylindrical-separatrix-type magnetic field on the plume of magnetic focusing type Hall thruster. *Plasma Sources Science and Technology*, 26(4):04LT02, March 2017.

[24] C. V. Young, A. Lucca Fabris, N. A. MacDonald-Tenenbaum, W. A. Hargus, and M. A. Cappelli. Time-resolved laser-induced fluorescence diagnostics for electric propulsion and their application to breathing mode dynamics. *Plasma Sources Science and Technology*, 27(9):094004, September 2018.

[25] T. Andreussi, M. M. Saravia, and M. Andrenucci. Plasma characterization in Hall thrusters by Langmuir probes. *Journal of Instrumentation*, 14(05):C05011, May 2019.

[26] V. Giannetti, M. M. Saravia, and T. Andreussi. Measurement of the breathing mode oscillations in Hall thruster plasmas with a fast-diving triple Langmuir probe. *Physics of Plasmas*, 27(12):123502, December 2020.

[27] E. O. Johnson and L. Malter. A Floating Double Probe Method for Measurements in Gas Discharges. *Physical Review*, 80(1):58–68, October 1950.

[28] V. I. Demidov, S. V. Ratynskaia, and K. Rypdal. Electric probes for plasmas: The link between theory and instrument. *Review of Scientific Instruments*, 73(10):3409–3439, October 2002.

[29] Shankar Bhattarai. Interpretation of Double Langmuir Probe I-V Characteristics at Different Ionospheric Plasma Temperatures. *American Journal of Engineering and Applied Sciences*, 10(4):882–889, April 2017.

[30] Jason Sommerville and Lyon King. An Optical Diagnostic for Xenon Hall Thrusters Including Metastable Contributions. In *42nd AIAA/ASME/SAE/ASEE Joint Propulsion Conference & Exhibit*, AIAA 2006-4823, Sacramento, CA, July 2006.

[31] J. R. Beattie, R. Robson, and J. D. Williams. Flight qualification of an 18-mN xenon ion thruster. In *23rd International Electric Propulsion Conference*, IEPC-93-106, Seattle, WA, September 1993.

[32] Vincent Rawlin, James Sovey, John Anderson, and J. Polk. NSTAR flight thruster qualification testing. In *34th AIAA/ASME/SAE/ASEE Joint Propulsion Conference & Exhibit*, AIAA-98-3936, Cleveland,OH, July 1998.

[33] Daniel A. Herman. NASA's Evolutionary Xenon Thruster (NEXT) Project Qualification Propellant Throughput Milestone: Performance, Erosion, and Thruster Service Life Prediction After 450 kg. In *JANNAF 7th Modeling and Simulation, 5th Liquid Propulsion, and 4th Spacecraft Propulsion Joint Subcommittee Meeting*, NASA/TM-2010-216816, Colorado Springs, Colorado, May 2010.

[34] Yu-hui Chiu, Brad L. Austin, Skip Williams, Rainer A. Dressler, and George F. Karabadzhak. Passive optical diagnostic of Xe-propelled Hall thrusters. I. Emission cross sections. *Journal of Applied Physics*, 99(11):113304, June 2006.

[35] George F. Karabadzhak, Yu-hui Chiu, and Rainer A. Dressler. Passive optical diagnostic of Xe propelled Hall thrusters. II. Collisional-radiative model. *Journal of Applied Physics*, 99(11):113305, June 2006.

[36] Taylor S. Matlock, C. William Larson, William A. Hargus Jr., and Michael R. Nakles. An Inversion Method for Reconstructing Hall Thruster Plume Parameters from the Line Integrated Measurements (Postprint). In *43rd AIAA/ASME/SAE/ASEE Joint Propulsion Conference & Exhibit*, AIAA 2007-5303, Cincinnatti, OH, July 2007.

[37] Juan Yang, Shigeru Yokota, Ryotaro Kaneko, and Kimiya Komurasaki. Diagnosing on plasma plume from xenon Hall thruster with collisional-radiative model. *Physics of Plasmas*, 17(10):103504, October 2010.

[38] Li-Qiu Wei, Wen-Bo Li, Yong-Jie Ding, Xi-Ming Zhu, Yan-Fei Wang, Jun-Feng Hu, Shi-Lin Yan, and Da-Ren Yu. A photographic method for in-orbit measurement of electron temperature distribution in the plume of Hall thrusters. *Plasma Sources Science and Technology*, 27(8):084002, August 2018.

[39] Yang Wang, Yan-Fei Wang, Xi-Ming Zhu, Oleg Zatsarinny, and Klaus Bartschat. A xenon collisional-radiative model applicable to electric propulsion devices: I. Calculations of electron-impact cross sections for xenon ions by the Dirac B-spline R-matrix method. *Plasma Sources Science and Technology*, 28(10):105004, October 2019.

[40] Xi-Ming Zhu, Yan-Fei Wang, Yang Wang, Da-Ren Yu, Oleg Zatsarinny, Klaus Bartschat, Tsanko Vaskov Tsankov, and Uwe Czarnetzki. A xenon collisional-radiative model applicable to electric propulsion devices: II. Kinetics of the 6s, 6p, and 5d states of atoms and ions in Hall thrusters. *Plasma Sources Science and Technology*, 28(10):105005, October 2019.

[41] Michael R. Nakles and Taylor S. Matlock. Hall Thruster Near-Field Plume Characterization Through Optical Emission Spectroscopy. In *36th International Electric Propulsion Conference*, IEPC-2019-246, Vienna, Austria, September 2019.

[42] Benny T. Nauschütt, Limei Chen, Kristof Holste, and Peter J. Klar. Non-invasive assessment of plasma parameters inside an ion thruster combining optical emission spectroscopy and principal component analysis. *EPJ Techniques and Instrumentation*, 8(1):13, August 2021.

[43] Benny Nauschütt, Limei Chen, Kristof Holste, and Peter J. Klar. Combination of optical emission spectroscopy and multivariate data analysis techniques as a versatile non-invasive tool for characterizing xenon/krypton mixed gas plasma inside operating ion thrusters. *Journal of Applied Physics*, 131(5):053301, February 2022.

[44] Hervé Abdi and Lynne J. Williams. Principal component analysis. *Wiley Interdisciplinary Reviews: Computational Statistics*, 2(4):433–459, June 2010.

[45] J. Vlcek. A collisional-radiative model applicable to argon discharges over a wide range of conditions. I. Formulation and basic data. *Journal of Physics D: Applied Physics*, 22(5):623–631, May 1989.

[46] J. Vlcek and V. Pelikan. A collisional-radiative model applicable to argon discharges over a wide range of conditions. II. Application to low-pressure, hollow-cathode arc and low-pressure glow discharges. *Journal of Physics D: Applied Physics*, 22(5):632–643, May 1989.

[47] Annemie Bogaerts, Renaat Gijbels, and Jaroslav Vlcek. Collisional-radiative model for an argon glow discharge. *Journal of Applied Physics*, 84(1):121–136, July 1998.

[48] Annemie Bogaerts, Renaat Gijbels, and Jaroslav Vlcek. Modeling of glow discharge optical emission spectrometry: Calculation of the argon atomic optical emission spectrum. *Spectrochimica Acta Part B: Atomic Spectroscopy*, 53(11):1517–1526, October 1998.

[49] S. Iordanova and I. Koleva. Optical emission spectroscopy diagnostics of inductively-driven plasmas in argon gas at low pressures. *Spectrochimica Acta Part B: Atomic Spectroscopy*, 62(4):344–356, April 2007.

[50] Niu Tian-Ye, Cao Jin-Xiang, Liu Lei, Liu Jin-Ying, Wang Yan, Wang Liang, and Lv You. A comparison among optical emission spectroscopic methods of determining electron temperature in low pressure argon plasmas. *Chinese Physics*, 16(9):2757–2763, September 2007.

[51] G. P. Canal, H. Luna, R. M. O. Galvão, and R. Castell. An approach to a non-LTE Saha equation based on the Druyvesteyn energy distribution function: a comparison between the electron temperature obtained from OES and the Langmuir probe analysis. *Journal of Physics D: Applied Physics*, 42(13):135202, June 2009.

[52] John B. Boffard, Chun C. Lin, and Charles A. DeJoseph Jr. Application of excitation cross sections to optical plasma diagnostics. *Journal of Physics D: Applied Physics*, 37(12):R143–R161, May 2004.

[53] John B. Boffard, R. O. Jung, Chun C. Lin, and A. E. Wendt. Optical emission measurements of electron energy distributions in low-pressure argon inductively coupled plasmas. *Plasma Sources Science and Technology*, 19(6):065001, October 2010.

[54] John B. Boffard, R. O. Jung, Chun C. Lin, L. E. Aneskavich, and A. E. Wendt. Argon 420.1–419.8 nm emission line ratio for measuring plasma effective electron temperatures. *Journal of Physics D: Applied Physics*, 45(4):045201, January 2012.

[55] Xi-Ming Zhu, Wen-Cong Chen, Jiang Li, and Yi-Kang Pu. Determining the electron temperature and the electron density by a simple collisional–radiative model of argon and xenon in low-pressure discharges. *Journal of Physics D: Applied Physics*, 42(2):025203, December 2008.

[56] Xi-Ming Zhu and Yi-Kang Pu. Optical emission spectroscopy in low-temperature plasmas containing argon and nitrogen: determination of the electron temperature and density by the line-ratio method. *Journal of Physics D: Applied Physics*, 43(40):403001, September 2010.

[57] Xi-Ming Zhu, Yi-Kang Pu, Yusuf Celik, Sarah Siepa, Edmund Schüngel, Dirk Luggenhölscher, and Uwe Czarnetzki. Possibilities of determining non-Maxwellian EEDFs from the OES line-ratios in low-pressure capacitive and inductive plasmas containing argon and krypton. *Plasma Sources Science and Technology*, 21(2):024003, April 2012.

[58] Sarah Siepa, Stephan Danko, Tsanko V. Tsankov, Thomas Mussenbrock, and Uwe Czarnetzki. On the OES line-ratio technique in argon and argon-containing plasmas. *Journal of Physics D: Applied Physics*, 47(44):445201, October 2014.

[59] Rainer A. Dressler, Yu-hui Chiu, Oleg Zatsarinny, Klaus Bartschat, Rajesh Srivastava, and Lalita Sharma. Near-infrared collisional radiative model for Xe plasma electrostatic thrusters: the role of metastable atoms. *Journal of Physics D: Applied Physics*, 42(18):185203, August 2009.

[60] Xi-Ming Zhu, Wen-Cong Chen, and Yi-Kang Pu. Gas temperature, electron density and electron temperature measurement in a microwave excited microplasma. *Journal of Physics D: Applied Physics*, 41(10):105212, May 2008.

[61] Priti, R. K. Gangwar, and R. Srivastava. Collisional-radiative model of xenon plasma with calculated electron-impact fine-structure excitation cross-sections. *Plasma Sources Science and Technology*, 28(2):025003, February 2019.

[62] Horst Löb. Ein elektrostatisches Raketentriebwerk mit Hochfrequenzionenquelle. *Astronautica Acta*, 8(1):49, January 1962.

[63] Horst Löb and Josef Freisinger. Ionenraketen. *Vieweg+Teubner Verlag*, Braunschweig, 1st edition, 1967.

[64] George C. Soulas. Improving the Total Impulse Capability of the NSTAR Ion Thruster with Thick-Accelerator-Grid Ion Optics. In *27th International Electric Propulsion Conference*, IEPC-01-081, Pasadena, CA, December 2001.

[65] Michael Schmid and IAP/TU Wien Surface Physics Group. A Simple Sputter Yield Calculator. `https://www.iap.tuwien.ac.at/www/surface/sputteryield`, accessed 17.02.2022.

[66] John R. Brophy, J. E. Polk, and L. C. Pless. Test-to-Failure of a Two-Grid, 30-cm-dia. Ion Accelerator System. In *23rd International Electric Propulsion Conference*, IEPC-93-172, Seattle, WA, September 1993.

[67] J. Scott Miller, Steve H. Pullins, Dale J. Levandier, Yu-hui Chiu, and Rainer A. Dressler. Xenon charge exchange cross sections for electrostatic thruster models. *Journal of Applied Physics*, 91(3):984–991, February 2002.

[68] Masakatsu Nakano. Three-dimensional simulations of grid erosion in ion engines. *Vacuum*, 83(1):82–85, September 2008.

[69] Miguel Sangregorio, Kan Xie, Ningfei Wang, Ning Guo, and Zun Zhang. Ion engine grids: Function, main parameters, issues, configurations, geometries, materials and fabrication methods. *Chinese Journal of Aeronautics*, 31(8):1635–1649, August 2018.

[70] Michael A. Lieberman and Allan J. Lichtenberg. Principles of Plasma Discharges and Materials Processing. *John Wiley & Sons*, Hoboken, 2nd edition, April 2005.

[71] Peter E. H. Köhler. Design, Konstruktion und Test eines hochauflösenden Gegenfeldanalysators mit fokussierender Elektrode und hochgelegtem Kollektor. *PhD thesis, Justus-Liebig-University*, Giessen, March 2018.

[72] Michael J. Patterson, Vincent K. Rawlin, James S. Sovey, Michael J. Kussmaul, and James Parkes. 2.3 kW Ion Thruster Wear Test. In *31st AIAA/ASME/SAE/ASEE Joint Propulsion Conference & Exhibit*, AIAA 95-2516, San Diego, CA, July 1995.

[73] Karl Jousten. Wutz Handbuch Vakuumtechnik (German Edition). *Vieweg+Teubner Verlag*, Wiesbaden, 10th edition, 2010.

[74] E. B. Saloman. Energy Levels and Observed Spectral Lines of Xenon, Xe I through Xe LIV. *Journal of Physical and Chemical Reference Data*, 33(3):765–921, September 2004.

[75] Patrick Dietz, Andreas Reeh, Konstantin Keil, Kristof Holste, Uwe Probst, Peter J. Klar, and Chris Volkmar. Global models for radio-frequency ion thrusters. *EPJ Techniques and Instrumentation*, 8(1):10, July 2021.

[76] Andreas Reeh. Der Modellierungsprozess und die Auslegung eines Radiofrequenz-Ionentriebwerks. *PhD thesis, Justus-Liebig-University*, Giessen, February 2021.

[77] Hiroshi Amemiya. Sheath Formation Criterion and Ion Flux for Non-Maxwellian Plasma. *Journal of the Physical Society of Japan*, 66(5):1335–1338, May 1997.

[78] J. T. Gudmundsson. On the effect of the electron energy distribution on the plasma parameters of an argon discharge: a global (volume-averaged) model study. *Plasma Sources Science and Technology*, 10(1):76–81, January 2001.

[79] John B. Boffard, R. O. Jung, Chun C. Lin, L. E. Aneskavich, and A. E. Wendt. Optical diagnostics for characterization of electron energy distributions: argon inductively coupled plasmas. *Plasma Sources Science and Technology*, 20(5):055006, August 2011.

[80] Eugene J. McGuire. Electron ionization cross sections in the Born approximation. *Physical Review A.*, 16(1):62–72, July 1977.

[81] D. Margreiter, H. Deutsch, and T.D. Märk. A semiclassical approach to the calculation of electron impact ionization cross-sections of atoms: from hydrogen to uranium. *International Journal of Mass Spectrometry and Ion Processes*, 139:127–139, September 1994.

[82] Dah-Wei Chang and Philip L. Altick. Doubly, singly differential and total ionization cross sections of rare-gas atoms. *Journal of Physics B: Atomic, Molecular and Optical Physics*, 29(11):2325–2335, January 1996.

[83] A. A. Sorokin, L. A. Shmaenok, S. V. Bobashev, B. Möbus, M. Richter, and G. Ulm. Measurements of electron-impact ionization cross sections of argon, krypton, and xenon by comparison with photoionization. *Physical Review A.*, 61(2):022723, January 2000.

[84] R. O. Jung, John B. Boffard, L. W. Anderson, and Chun C. Lin. Electron-impact excitation cross sections from the xenon J=2 metastable level. *Physical Review A.*, 72(2):022723, August 2005.

[85] M. A. Stevenson, L. R. Hargreaves, B. Lohmann, I. Bray, D. V. Fursa, K. Bartschat, and A. Kheifets. Fully differential cross-section measurements for electron-impact ionization of neon and xenon. *Physical Review A.*, 79(1):012709, January 2009.

[86] Richard L. Gorsuch. Factor Analysis. *Psychology Press*, New York, 2nd edition, May 2013.

[87] V. Paul Pauca, J. Piper, and Robert J. Plemmons. Nonnegative matrix factorization for spectral data analysis. *Linear Algebra and its Applications*, 416(1):29–47, July 2006.

[88] Alan Julian Izenman. Linear Discriminant Analysis. In Modern Multivariate Statistical Techniques: Regression, Classification, and Manifold Learning, pages 237–280. *Springer New York*, New York, NY, 1st edition, 2013.

[89] Jan Benedikt, Holger Kersten, and Alexander Piel. Foundations of measurement of electrons, ions and species fluxes toward surfaces in low-temperature plasmas. *Plasma Sources Science and Technology*, 30(3):033001, March 2021.

[90] Benny Nauschütt, Felix Becker, Limei Chen, Kristof Holste, and Peter J. Klar. Plasma parameter measurement on a RIT-10 using empirical correlations between non-invasive optical emission spectroscopy and Langmuir diagnostics. In *37th International Electric Propulsion Conference*, IEPC-2022-253, Cambridge, MA, 2022.

[91] Andreas Reeh, Uwe Probst, and Peter J. Klar. Global model of a radio-frequency ion thruster based on a holistic treatment of electron and ion density profiles. *The European Physical Journal D*, 73(11):232, November 2019.

[92] Gilles de Rosny, Earl R. Mosburg, John R. Abelson, Genevieve Devaud, and Ralph C. Kerns. Evidence for a time dependent excitation process in silane radio frequency glow discharges. *Journal of Applied Physics*, 54(5):2272–2275, May 1983.

[93] R. A. Gottscho and T. A. Miller. Optical techniques in plasma diagnostics. *Pure and Applied Chemistry*, 56(2):189–208, January 1984.

[94] Daniel L. Flamm and Vincent M. Donnelly. Time-dependent excitation in high- and low-frequency chlorine plasmas. *Journal of Applied Physics*, 59(4):1052–1062, February 1986.

[95] Alexander Kramida, Yuri Ralchenko, Joseph Reader, and NIST ASD Team. NIST Atomic Spectra Database (ver. 5.9). `https://physics.nist.gov/asd`, 2021.

[96] Manfred Schäfer. Plasmadiagnostik und Energiebilanzuntersuchung an dem HF-Ionentriebwerk RIT-10. *PhD thesis, Justus-Liebig-University*, Giessen, July 1971.

[97] Pascal Chabert and Nicholas Braithwaite. Physics of radio-frequency plasmas. *Cambridge University Press*, New York, 1st edition, February 2011.

[98] P. Chabert, J. Arancibia Monreal, J. Bredin, L. Popelier, and A. Aanesland. Global model of a gridded-ion thruster powered by a radiofrequency inductive coil. *Physics of Plasmas*, 19(7):073512, July 2012.

[99] Mantas Dobkevicius and Davar Feili. Multiphysics Model for Radio-Frequency Gridded Ion Thruster Performance. *Journal of Propulsion and Power*, 33(4):939–953, July 2017.

ATTACHMENTS

Attachment 1: Non-invasive assessment of plasma parameters inside an ion thruster combining optical emission spectroscopy and principal component analysis

Attachment 2: Combination of optical emission spectroscopy and multivariate data analysis techniques as a versatile non-invasive tool for characterizing xenon/krypton mixed gas plasma inside operating ion thrusters

Attachment 3: Plasma parameter measurement on a RIT-10 using empirical correlations between non-invasive optical emission spectroscopy and Langmuir diagnostics (not peer-reviewed)

Nauschütt *et al. EPJ Techniques and Instrumentation* (2021) 8:13
https://doi.org/10.1140/epjti/s40485-021-00070-x

EPJ Techniques and Instrumentation

RESEARCH ARTICLE

Open Access

Non-invasive assessment of plasma parameters inside an ion thruster combining optical emission spectroscopy and principal component analysis

Benny T. Nauschütt*, Limei Chen, Kristof Holste and Peter J. Klar

*Correspondence:
Benny.Nauschuett@physik.uni-giessen.de
Institute of Experimental Physics I, Justus Liebig University, Heinrich-Buff-Ring 16, 35392 Giessen, Germany

Abstract

We present a non-invasive approach for determining plasma parameters such as electron temperature and density inside a radio-frequency ion thruster (RIT) using optical emission spectroscopy (OES) in conjunction with principal component analysis (PCA). Instead of relying on a theoretical microscopic model of the plasma emission to extract plasma parameters from the OES, an empirical correlation is established on the basis of conducting simultaneous OES and Langmuir diagnostics. The measured reference spectra are simplified and a PCA is performed. The PCA results are correlated with the plasma parameters of the Langmuir measurements yielding a one-to-one correspondence. This correlation allows us to derive the plasma parameters by analysis of a non-invasively determined emission spectrum without additional Langmuir measurements. We show how the plasma parameters can be calculated from OES measurements using this correlation. Under the assumption that the electronic system thermalizes on much shorter time scales than the period of the RF signal driving the thruster, we can also use time-resolved spectral data to determine the time evolution of plasma parameters. In future, this method may contribute to shorter test and qualification times of RITs and other ion thrusters.

Keywords: Optical emission spectroscopy, Plasma parameters, Principal component analysis

Introduction

Electric propulsion (EP) systems are nowadays commonly used on spacecrafts [1, 2]. Due to their high thrust to fuel consumption ratio as well as their large variety of different implementations and usable propellants, EP systems are a versatile alternative to their chemical counterparts in many in-orbit applications. One type of EP system is the radio-frequency ion thruster (RIT), which was developed at the Justus Liebig University of Giessen in the 1960s [3, 4]. Inside a RIT, a plasma of the propellant is sustained by inductive heating of its electrons. Positive ions (usually xenon) are accelerated by a system of extraction grids and expelled from the thruster, thus generating thrust according to Newton's third law [1, 2, 5]. The plasma in the discharge vessel is responsible for the thruster's performance. Thus, knowledge of plasma parameters (e. g., electron temperature and density) may give valuable insight into the erosion processes inside the plasma vessel and of the grid system, but also thruster performance in general. Usually, plasma parameters are determined using invasive electrical probes [6, 7]. For a RIT or other thrusters during qualification for space , it is not desirable to use invasive probes inside the plasma vessel, as they affect the thruster's performance [6] and, if installed permanently, will constitute an additional possible source of failure.

In this paper a method is introduced that utilizes non-invasive optical emission spectroscopy (OES) to assess plasma parameters of an operating thruster. It may be used during terrestrial testing in the context of the qualification process for space. Depending on the thruster, an optical probe can even be installed outside of the ion plume, so plume and probe do not affect each other. Usually, assessing plasma parameters by OES requires complex theoretical modeling of the electronic states of the atoms and ions of the plasma and, via the scattering and recombination processes, their occupation and the optical transitions contributing to the emission spectrum in order to derive a theoretical spectrum which may be compared with experiment.

To circumvent the involved challenges, we pursue an empirical approach which avoids entirely the use of a microscopic plasma model for extracting the plasma parameters from an optical emission spectrum. We measure emission spectra simultaneously with the plasma parameters in a RIT like setup and correlate the results with the help of a principal component analysis (PCA)[8]. This correlation can then be used to determine the state of a plasma non-invasively by simply acquiring an optical emission spectrum and employing the established correlation as long as the plasma is operated in the same range of plasma parameters as used for the reference data set. Ultimately, the method shall be applied to thrusters such as RITs to give an easy and uncomplicated access to plasma parameters and contribute to shorter test cycles and qualification times. It might also be used to optimize a RIT to, for instance, reduce its extraction grid erosion, which partially depends on the plasma parameters and limits its lifetime [9, 10]. Operation of the RIT with low mass efficiency results in a low ionization degree of the plasma and causes more charge exchange reactions, leading to increased sputtering of the acceleration grid. High mass efficient operation, on the other hand, causes a higher electron temperature, which may lead to sputtering on the screen grid.

In case of an RF-plasma, the excitation as well as the plasma parameters and OES are not constant but oscillating in time [11–14]. To examine the time-dependent plasma parameters, time- or phase-resolved spectra can be measured and evaluated using the found correlation.

A brief description of a typical theoretical model is given in "Theoretical and empirical model" section together with a comparison to our approach. The experimental details are described in "Experimental details and theory" section, in particular, the Langmuir and OES measurements as well as the PCA approach correlating the two measurements are explained. The resulting correlation, its application to time-resolved spectra and a corresponding discussion are given in "Results and discussion" section. The paper is concluded in "Conclusion" section where the method is rated and an outlook on future applications is given.

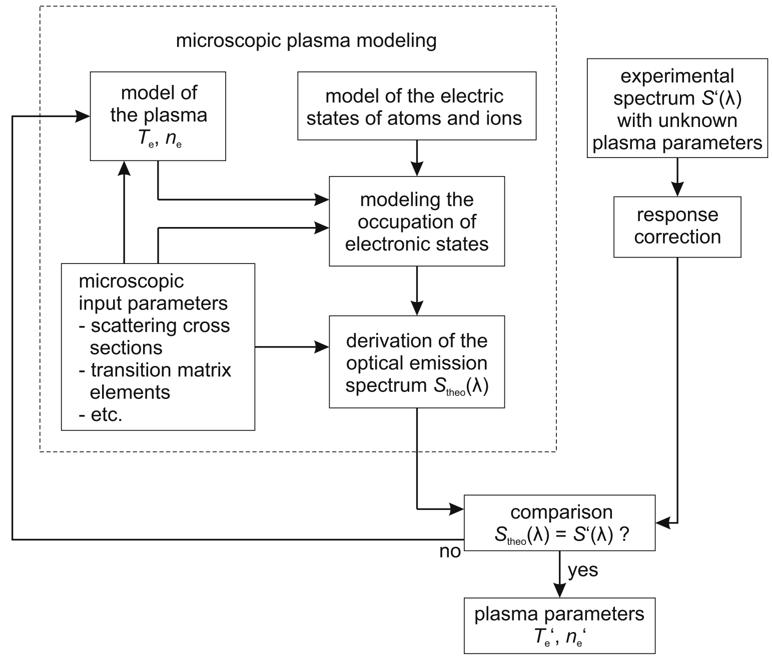

Fig. 1 Schematic description of the work flow necessary to extract plasma parameters from an experimental optical emission spectrum $S'(\lambda)$ by comparison with microscopic theory. The theoretical model contains a microscopic description of the plasma as well as of the electronic states of its ions and atoms. The occupation of these states needs to be modeled based on the microscopic processes inside the plasma. The intensities of the optical transitions need to be calculated based on the occupation of the electronic states and the transition matrix elements in order to obtain a theoretical spectrum $S_{theo}(\lambda)$, which can then be compared to the response-corrected experimental spectrum to obtain the plasma parameters

Theoretical and empirical model

Theoretical plasma models exist, e. g., for argon [15–28] and xenon [25, 29–38]. A possible use of such a model for extracting plasma parameters from optical emission spectra is shown schematically in Fig. 1. Such models are typically tailored for a specific application. For other applications, such as using other gases, the theoretical model needs to be modified.

In electric propulsion, alternative propellants such as krypton and iodine gain considerable interest [39, 40]. In case of molecular propellants like iodine I_2 these models would become increasingly complex. For a successful description of the corresponding plasma, such a microscopic model requires many microscopic input parameters like excitation cross sections for all relevant species, including I_2, I_2^+, I^+, I^- in case of an iodine plasma.

Furthermore, the microscopic parameters serving as basis of such a model like, for instance, transition matrix elements, scattering cross sections etc. are usually not accurately known, as they are, in many cases, difficult to derive theoretically and to verify experimentally. Typically, some simplifications and assumptions are made to compensate the lack of information and to reduce the complexity of the model. Heavy gases like xenon have a large number of electronic states. Ref. [41] lists 443 levels for neutral Xe, 161 for Xe^+, 157 for Xe^{2+} and a lot more for higher ionized xenon ions. Since not all of these levels are relevant in a real plasma, only some levels are considered in the modeling (e. g., 173 levels in Ref. [33] or 38 levels in Ref. [38]). So the number of considered levels can vary from one model to another. Neglecting levels may, however, cause errors in the calculated population of other related levels. Another typical simplification is the negligence of uncommon excitation processes like ion-atom collisions or excitation from meta-stable states. However, these processes are necessary in some cases to yield a reliable correlation between OES and plasma parameters [30]. Whether a simplification or assumption in a model is justified can only be verified by a direct comparison with experiments.

Therefore, we decided to avoid the microscopic modeling entirely and correlate the optical spectrum directly to measured plasma parameters using multivariate data analysis techniques. In contrast to the theoretical plasma model, our empirical approach does not require any microscopic input other then the measurement of the plasma parameters. A schematic description of our approach is shown in Fig. 2. We measure a reference data set of emission spectra simultaneously with the plasma parameters in a RIT like setup operating with a propellant plasma, such as xenon. A Langmuir diagnostics is permanently installed inside the discharge vessel. Using a Langmuir double probe [42] the electron temperature and density can be measured. The analysis of the OES reference data is performed by applying a PCA [8]. The results from both measurements are analyzed and a one-to-one correlation between the principal components and the electron temperature and the electron/ion density is established. This correlation can be employed to extract plasma parameters non-invasively from plasmas operating under similar conditions as the reference plasma, for instance, inside a thruster. For this purpose, an optical emission spectrum $S'(\lambda)$ is measured and expanded in terms of the PC of the reference data to yield its PC scores. Then, using the established correlation between PC scores and plasma parameters, n'_e and T'_e, corresponding to $S'(\lambda)$ can be obtained.

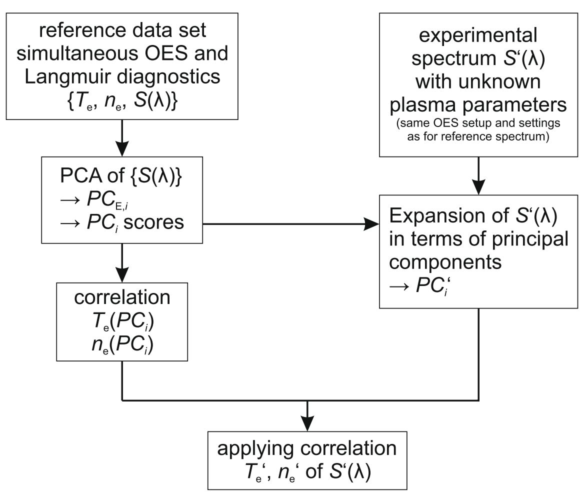

Fig. 2 Schematic description of our measurement-based correlation between optical emission spectrum and plasma parameters. First, a reference data set is measured consisting of simultaneously performed OES and Langmuir diagnostics. The measured spectrum is transferred into a simplified coordinate system using PCA, which yields the axes $PC_{E,i}$ and the coordinates or scores PC_i of the spectra on these axes. The scores PC_i are then correlated with the measured plasma parameters. The correlation can then be used to extract plasma parameters from a measured spectrum $S'(\lambda)$ by calculating its scores PC'_i and inserting them into the correlation

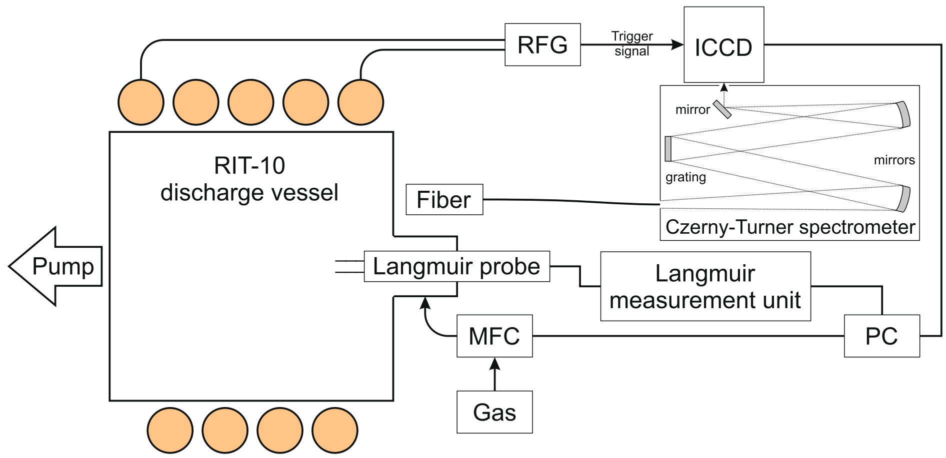

Fig. 3 Experimental setup for simultaneous optical emission spectroscopy and the Langmuir double probe measurements

Experimental details and theory

The experimental setup used is shown in Fig. 3. An inductively generated plasma is ignited in a 10 cm diameter cylindrical quartz glass discharge vessel of a RIT-10. Basically, it is a RIT-10 without an extraction system or surrounding vacuum. The gas inlet in this setup also contains the Langmuir double probe, which is used to determine the electron temperature T_e and density n_e [6, 7, 42] . The glass vessel facilitates an easy optical access to the plasma from behind. The spectrum was measured at a position close to the Langmuir probe. The Czerny-Turner spectrometer used is connected to an intensified charge-coupled device (ICCD) camera. In the observed spectral window from 820 to 840 nm the system has a resolution of approximately 28 pm/pixel. This spectral window was chosen, since neutral xenon has several strong lines in the near-infrared region. Six of them lie in the observed window. The ICCD is capable of both continuous-wave (cw) and time-resolved measurements on the nanosecond scale and was operated with 20 ns time resolution here, i.e., the acquisition time was 20 ns long after a predefined time delay. The corresponding trigger was a 0 to 5 V rectangular signal taken from the radio-frequency generator (RFG). For each delay time, several 100 acquisitions were recorded and accumulated. By varying the delay time in the range of 600 to 1400 ns a series of optical emission spectra is obtained which covers the time evolution of the plasma parameters during one RF excitation cycle. The gas flow into the discharge vessel is controlled by a mass flow controller (MFC). The plasma was excited by the RFG at a resonance frequency of approximately 1.2 MHz corresponding to a period of the RF cycle of 0.83 μs. The RFG input power was varied while keeping the gas flow constant. The experiments were performed for various gas flows.

An example of a cw OES measurement is shown as an inset in Fig. 4. The six xenon lines, (1) to (6) are assigned to the optical transitions between Xe^0 states using the NIST data base [43]. The electronic states involved are shown in the main graph. The upper levels of the six transitions observed in this experiment can be populated either by direct excitation or by another spectral transition (the strongest are shown in Fig. 4). In Table 1, wavelength position, relaxation time, qualitative relative intensity and the involved electronic states are given for each transition according to the data provided in Ref. [41] and [43].

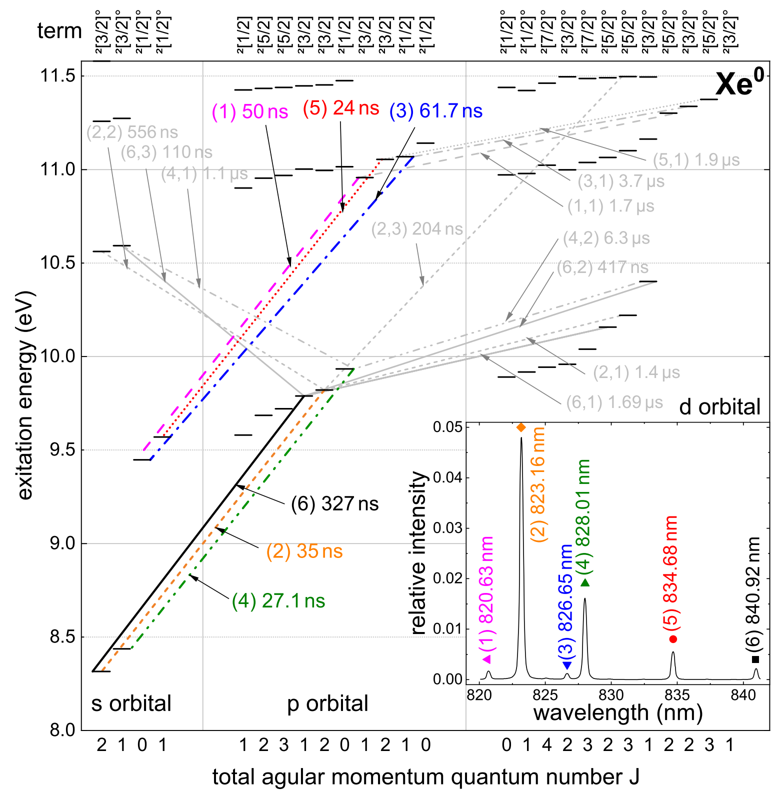

Fig. 4 The measured spectral range from 820 nm to 841 nm exhibits six xenon transitions, which are shown in the energy level scheme for neutral xenon generated from the data from Ref. [41]. A corresponding example spectrum is shown in the inset. The strongest transitions feeding the upper levels of the observed transitions are also shown. The relaxation times of the transitions are given according to Ref. [43]. Using the labeling given in the figure, the transitions can be found in Table 1 for additional details

As examples a series of cw OES measurements is shown in Fig. 5a with the corresponding Langmuir double probe measurements in Fig. 5b. Here, the RF input power was varied at a constant gas flow of 0.1 sccm.

The line intensity ratios differ only slightly in the spectra shown in Fig. 5a. All spectra were intensity-normalized over the measured range. The effect can be observed best for the two strongest lines at 823.2 nm and 828.0 nm. Here, the 823.2 nm line increases with higher input power, while the 828.0 nm line decreases. The plasma parameters determine the population of the energy levels. At different operating points with different plasma parameters the levels are populated differently with electrons, resulting in other line ratios when the electrons recombine radiatively.

Principal component analysis

Instead of founding the analysis on individual line ratios, we made use of the entire spectral information in terms of relative intensities available in a spectrum of a given operational point by performing a PCA of all spectra [8]. The PCA technique can simplify the complex correlations between several measured lines and the resulting plasma parameters by reducing the dimensions of the data set. Similar techniques for dimension reduction which may offer an alternative and may also yield satisfying results are Linear

Table 1 Wavelengths, relaxation times, intensities and the involved electronic states of the transitions shown in Fig. 4 are listed [41, 43]

index	wavelength (nm)	relaxation time (ns)	intensity	lower level			upper level		
				configuration	term	J	configuration	term	J
(1)	**820.63**	**50**	**700**	$\boldsymbol{5p^5(^2P^\circ_{1/2})6s}$	$\boldsymbol{^2[1/2]^\circ}$	**0**	$\boldsymbol{5p^5(^2P^\circ_{1/2})6p}$	$\boldsymbol{^2[3/2]}$	**1**
(1,1)	3605.49	1700	20	$5p^5(^2P^\circ_{1/2})6p$	$^2[3/2]$	1	$5p^5(^2P^\circ_{1/2})5d$	$^2[5/2]^\circ$	2
(2)	**823.16**	**35**	**10000**	$\boldsymbol{5p^5(^2P^\circ_{3/2})6s}$	$\boldsymbol{^2[3/2]^\circ}$	**2**	$\boldsymbol{5p^5(^2P^\circ_{3/2})6p}$	$\boldsymbol{^2[3/2]}$	**2**
(2,1)	3107.77	1400	6000	$5p^5(^2P^\circ_{3/2})6p$	$^2[3/2]$	2	$5p^5(^2P^\circ_{3/2})5d$	$^2[5/2]^\circ$	3
(2,2)	1672.82	556	5000	$5p^5(^2P^\circ_{3/2})6p$	$^2[3/2]$	2	$5p^5(^2P^\circ_{3/2})7s$	$^2[3/2]^\circ$	2
(2,3)	739.38	204	150	$5p^5(^2P^\circ_{3/2})6p$	$^2[3/2]$	2	$5p^5(^2P^\circ_{3/2})7d$	$^2[5/2]^\circ$	3
(3)	**826.65**	**61.7**	**500**	$\boldsymbol{5p^5(^2P^\circ_{1/2})6s}$	$\boldsymbol{^2[1/2]^\circ}$	**1**	$\boldsymbol{5p^5(^2P^\circ_{1/2})6p}$	$\boldsymbol{^2[1/2]}$	**1**
(3,1)	4610.87	3700	1	$5p^5(^2P^\circ_{1/2})6p$	$^2[1/2]$	1	$5p^5(^2P^\circ_{1/2})5d$	$^2[3/2]^\circ$	2
(4)	**828.01**	**27.1**	**7000**	$\boldsymbol{5p^5(^2P^\circ_{3/2})6s}$	$\boldsymbol{^2[3/2]^\circ}$	**1**	$\boldsymbol{5p^5(^2P^\circ_{3/2})6p}$	$\boldsymbol{^2[1/2]}$	**0**
(4,1)	1878.82	1100	860	$5p^5(^2P^\circ_{3/2})6p$	$^2[1/2]$	0	$5p^5(^2P^\circ_{3/2})7s$	$^2[3/2]^\circ$	1
(4,2)	2651.77	6300	30	$5p^5(^2P^\circ_{3/2})6p$	$^2[1/2]$	0	$5p^5(^2P^\circ_{3/2})5d$	$^2[3/2]^\circ$	1
(5)	**834.68**	**24**	**2000**	$\boldsymbol{5p^5(^2P^\circ_{1/2})6s}$	$\boldsymbol{^2[1/2]^\circ}$	**1**	$\boldsymbol{5p^5(^2P^\circ_{1/2})6p}$	$\boldsymbol{^2[3/2]}$	**2**
(5,1)	3869.68	1900	200	$5p^5(^2P^\circ_{1/2})6p$	$^2[3/2]$	2	$5p^5(^2P^\circ_{1/2})5d$	$^2[5/2]^\circ$	3
(6)	**840.92**	**327**	**2000**	$\boldsymbol{5p^5(^2P^\circ_{3/2})6s}$	$\boldsymbol{^2[3/2]^\circ}$	**2**	$\boldsymbol{5p^5(^2P^\circ_{3/2})6p}$	$\boldsymbol{^2[3/2]}$	**1**
(6,1)	3367.59	1690	3500	$5p^5(^2P^\circ_{3/2})6p$	$^2[3/2]$	1	$5p^5(^2P^\circ_{3/2})5d$	$^2[5/2]^\circ$	2
(6,2)	2026.78	417	2300	$5p^5(^2P^\circ_{3/2})6p$	$^2[3/2]$	1	$5p^5(^2P^\circ_{3/2})5d$	$^2[3/2]^\circ$	1
(6,3)	1541.8	180	110	$5p^5(^2P^\circ_{3/2})6p$	$^2[3/2]$	1	$5p^5(^2P^\circ_{3/2})7s$	$^2[3/2]^\circ$	1

The listed intensities are only the qualitative vf. [41]. Using the index, the transitions can be found in Fig. 4. The observed transitions are shown in bold

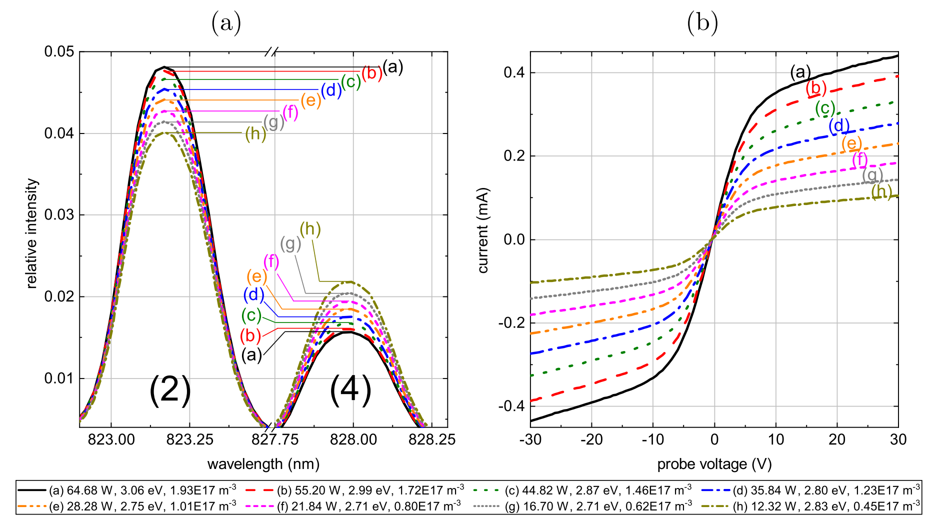

Fig. 5 The two strongest lines (see Fig. 4) of intensity-normalized xenon spectra for a measurement series at 0.1 sccm gas flow at different operating points (see also Fig. 6) (**a**) together with the corresponding Langmuir double probe measurements (**b**). This series of spectra is part of the reference data set

Discriminant Analysis [44], Non-negative Matrix Factorization [45] and Factor Analysis [46].

A total of m spectra is measured as a reference data set. A spectrum consists of n data points, i. e., n wavelength positions and corresponding emission intensity values. Each of the m spectra yields a data point in an n-dimensional space, where each of the n wavelength positions of the spectrum corresponds to one coordinate axis and the intensity value to the specific coordinate on that axis. The PCA simplifies the data by reducing this n-dimensional space into, for example, a two-dimensional space, that represents the data best. This is done by finding the axes with the highest variance in the data.

First, the average spectrum of the entire reference data set $\overline{S_{\mathrm{PCA}}}(\lambda)$ is subtracted from each spectrum $S(\lambda)$. To derive the new coordinates, i. e., the PCA-axes, the covariances σ_{ij} of each of the n wavelength positions with every other wavelength position (including itself) are calculated using

$$\sigma_{ij} = \frac{1}{m} \cdot \sum_{k=0}^{m} (x_{ki} - \overline{x_i}) \cdot (x_{kj} - \overline{x_j}) \quad \text{where } \overline{x_i} = \overline{x_j} = 0. \tag{1}$$

Here, x_{ki} and x_{kj} are the values of wavelength positions i and j of the spectrum k. Since the average intensities of each wavelength position $\overline{x_i}$ and $\overline{x_j}$ were already subtracted before, they are now zero.

With these covariances the covariance matrix $\mathbf{C}$ is set up

$$\mathbf{C} = \begin{pmatrix} \sigma_{00} & \sigma_{01} & \cdots & \sigma_{0n} \\ \sigma_{10} & \sigma_{11} & \cdots & \sigma_{1n} \\ \vdots & \vdots & \ddots & \vdots \\ \sigma_{n0} & \sigma_{n1} & \cdots & \sigma_{nn} \end{pmatrix}. \tag{2}$$

Diagonalizing $\mathbf{C}$ yields its eigenvalues, which correspond to the variance of the data on the principal component axes $PC_{\mathrm{E},i}(\lambda)$. The PC-axes are the eigenvectors of $\mathbf{C}$.

To transfer a spectrum into the new coordinate system spanned by the eigenvectors $PC_{\mathrm{E},i}(\lambda)$ and obtain its coordinates, i. e., the PC scores, the spectrum is scalar multiplied with each eigenvector

$$PC_i = \sum_{\lambda} (S(\lambda) - \overline{S_{\mathrm{PCA}}}(\lambda)) \cdot PC_{\mathrm{E},i}(\lambda). \tag{3}$$

The spectrum can now be written as

$$S(\lambda) = \overline{S_{\mathrm{PCA}}}(\lambda) + \sum_{i} PC_i \cdot PC_{\mathrm{E},i}(\lambda). \tag{4}$$

The percentage of the variance on each axis of the total variance shows how well the data is represented. If the sum of the variances of PC_1 and PC_2 is already close to the total variance, these two axes are sufficient to describe the main differences in the data.

Evaluation of the Langmuir probe measurements

The plasma parameters obtained from the Langmuir double probe measurements were evaluated using a modified version of the standard procedure described in Ref. [6], [7] and [42], which is more robust against deviations from the theoretical ideal. First, the ion saturation current I_{sat} is determined as the intercept of a linear fit of the saturation region (approximately $< -20\,\mathrm{V}$ and $> +20\,\mathrm{V}$ in Fig. 5b). The slope a of the fit is subtracted from the measured U-I-characteristic ($I_{\mathrm{corrected}}(U) = I(U) - a \cdot U$). Afterwards, $I_{\mathrm{corrected}}(U)$ is divided by I_{sat} to normalize the U-I-characteristic. Next, the electron temperature T_{e} is extracted from the maximum slope. A polynomial fit of third order ($f(x) = \sum_{i=0}^{3} a_i \cdot x^i$) around $U = 0 \pm \Delta U$ is used instead of a linear fit, because the resulting slope is less affected by the chosen fit bounds ΔU. The maximum slope of this fit is given with $s_{\mathrm{max}} = -\frac{1}{3} a_2^2 / a_3 + a_1$ and yields the electron temperature according to

$$T_{\mathrm{e}} = \frac{e}{2k_{\mathrm{B}} \cdot s_{\mathrm{max}}}. \tag{5}$$

The electron density n_{e} is calculated from I_{sat}, T_{e}, the probe area A_{p}, and the ion mass m_{ion} according to

$$n_{\mathrm{e}} = \frac{I_{\mathrm{sat}}}{A_{\mathrm{p}} e} \sqrt{\frac{m_{\mathrm{ion}}}{k_{\mathrm{B}} T_{\mathrm{e}}}}. \tag{6}$$

It should be noted that the definition of a temperature assumes a Maxwellian electron energy distribution function (EEDF) [6, 7, 42]. For an RF plasma, the EEDF can deviate from the Maxwellian ideal, as the fast electrons in the Maxwell tail are suppressed [21, 47]. In particular in a theoretical microscopic plasma model, the EEDF can have a major impact on the calculated spectrum and therefore on the extraction of plasma parameters by comparison between microscopic model and experiment. In case of our empirical approach the specific EEDF is not relevant, as long as it is comparable in model setup and later measurement, which should be the case when the optical emission spectra are comparable.

Results and discussion

Before performing the PCA, the measured spectra are compressed by considering only the intensities or areas of the spectral lines (see e. g. Figs. 4 or 5a). This prevents small wavelength shifts in the range of several tens of picometers to influence the PCA result. The line intensities are then used as input variables for the PCA. The PCA yields a set of new orthogonal coordinate axes, i. e., the principal components $PC_{\mathrm{E},i}$ ($i = 1,\ldots,n$), along which the spread in the data set is maximum, as they are the eigenvectors of the variance. The $PC_{\mathrm{E},i}$ are numbered serially to descending variance weight, i. e., $PC_{\mathrm{E},1}$ carries the highest weight, followed by $PC_{\mathrm{E},2}$ etc. Often, the first few $PC_{\mathrm{E},i}$ already collate most of the variance (e. g., 90 %), and thus plots of the PC scores of a spectrum in a low-dimensional coordinate system spanned by those $PC_{\mathrm{E},i}$ can separate the data adequately. In case of our data, $PC_{\mathrm{E},1}$ and $PC_{\mathrm{E},2}$ are sufficient to fully distinguish between the spectra obtained at different operational points of the plasma, i. e., corresponding to different plasma parameters. The results are shown in Fig. 6a. It can be seen that the individual data points are clearly separated. The cloud of data points representing all spectra analyzed has a “triangular” shape. Towards lower PC_1-values, the plasma extinguished. Towards higher PC_1-values the input power limitation of the RFG was reached. The plasma is stable even at lower input powers at higher gas flows. Therefore, more measurements were possible at higher PC_2-values. With decreasing gas flow towards lower PC_2-values, the

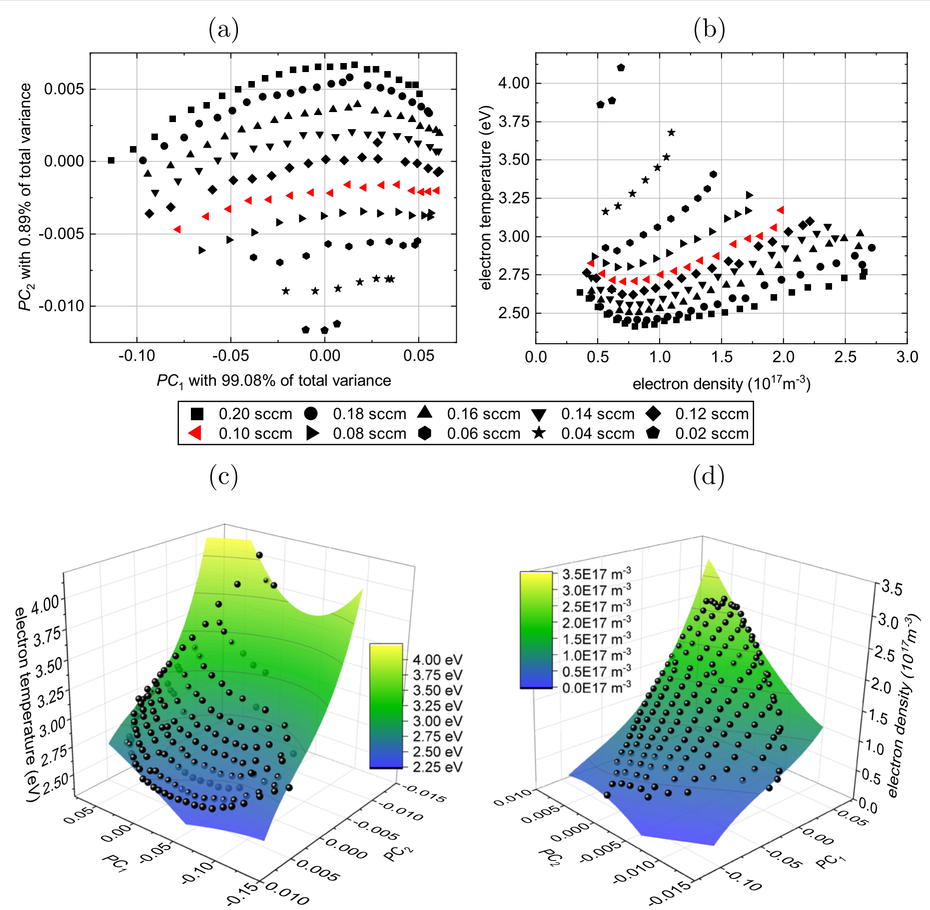

Fig. 6 PCA scores from the cw OES measurements of a xenon plasma (**a**) and the corresponding electron temperatures and densities from the simultaneously conducted Langmuir double probe measurements (**b**). The PCA scores of the spectra shown in Fig. 5a from the 0.10 sccm measurement series (shown in red here) are clearly distinguishable. The input power increases from left to right in both plots (a) and (**b**). The fits of the electron temperature (**c**) and density (**d**) over the PCA scores are the depict correlation between OES and plasma parameters

minimum power to sustain the plasma increased, until eventually reaching the RFG input power limit. Therefore, only a few points could be measured in this range.

The plasma parameters electron temperature T_e and electron density n_e corresponding to each spectrum from the Langmuir measurements are shown in Fig. 6b. Here, the cloud of data points also exhibits a triangular arrangement. The reason for this shape is the same as discussed above for the PCA data in Fig. 6a.

While the data points are spread quite homogeneously in Fig. 6a, the data sets corresponding to various gas flows in Fig. 6b are very close for low T_e and far apart for high T_e. This means that the sensitivity of T_e on the neutral gas density increases with decreasing gas flow. This change in sensitivity on the gas flow can barely be observed for the OES data in Fig. 6a. In a series of spectra where the RFG input power was varied, the corresponding data points are rather equally distributed, resulting from constant steps of the RFG input voltage. The data points plotted by red symbols in Fig. 6a and b correspond to the series of optical emission spectra and corresponding Langmuir measurements shown in Fig. 5a and b, respectively. It can be seen that the red data points string together well underlining that the PCA and the restriction to the PC scores of $PC_{E,1}$ and $PC_{E,2}$ grabs the differences in the spectra sufficiently to clearly distinguish between them.

By using a polynomial fit of the form given in Eq. (7) the plasma parameters from Fig. 6b can be described as a function of the PCA-scores from Fig. 6a, yielding the sought correlation

$$f(PC_1, PC_2) = \sum_{i=0}^{3} \sum_{j=0}^{i+j\leq 3} a_{i,j} \cdot PC_1^i \cdot PC_2^j. \tag{7}$$

The fitted surfaces for the electron temperature and density versus the scores of PC_1 and PC_2 are shown in Fig. 6c and d, respectively. The R^2-values of the fitting procedures were 0.984 (T_e) and 0.998 (n_e), so the fitted surfaces are well suited for describing the measured data. The choice of a polynomial fitting surface of order 3 is the result of an optimization process. In other cases, such as other propellant gases or the choice of another spectral window, fitting with lower or higher polynomials may turn out the best choice.

To apply this correlation to a measured spectrum $S'(\lambda)$ for which the plasma parameters are not known, the eigenvectors of the PCA $PC_{E,i}(\lambda)$ are needed in order to extract them. The eigenvectors are scalar multiplied with the spectrum $S'(\lambda)$ from which the average of the intensities initially used for the PCA $\overline{S_{PCA}}(\lambda)$ are subtracted, as shown in Eq. (3). The resulting coordinates of PC_1 and PC_2 can then be inserted into the polynomial expressions describing the fitted surfaces $T_e(PC_1, PC_2)$ and $n_e(PC_1, PC_2)$ shown in Fig. 6c and d to obtain T_e' and n_e' corresponding to $S'(\lambda)$.

In order to minimize experimental uncertainties the optical spectra and Langmuir parameters were measured at almost the same position inside the plasma (see Fig. 3). It is essential to keep the deviations between the spots probed by OES and the Langmuir probe as small as possible, because the plasma parameters may vary locally inside the vessel. A large distance between the measurement positions introduces uncertainties when employing the established correlation for extracting plasma parameters from another system. In principle, the correlation may be employed on any other Xe plasma source where the plasma parameters lie in the same range as used here for establishing the correlation. Having established a reliable correlation, it can be used to spatially monitor the plasma parameter variation inside a plasma vessel. For example, such spatial mapping will further benefit the understanding of the processes inside an ion thruster.

The relaxation times of the observed transitions are in the range of 24 to 327 ns and even longer in case of radiative transitions whose higher electronic state is fed by other higher lying states (see Fig. 4 or Table 1). Compared to the RF period of approximately 833 ns, not all of these times are significantly shorter. This can cause different relative line intensities, when the plasma is driven with another radio frequency, and the population of the electronic states cannot follow the RF excitation. Because of such effects, it is of paramount importance to make sure that reference spectra and probe spectra are recorded with the corresponding plasmas driven by the same radio frequency.

Time-resolved measurements

The time dependence of the example OES measurement from Fig. 4 is shown in Fig. 7. The graph shows the variation of the line intensities obtained from a series of optical emission spectra taken at different delay times. Here, the integrated line intensities of the six strongest lines in the spectrum are plotted as the relative deviation from their corresponding average value during one RF cycle. The intensity of each line oscillates about its average value with twice the radio frequency. This is anticipated as the power input is proportional to the RF field squared. During one RF cycle, the electrons are accelerated the most at the maximum and minimum electric field, but in opposite directions. The excitation of the gas atoms and ions in the discharge chamber is strongest at these two points in

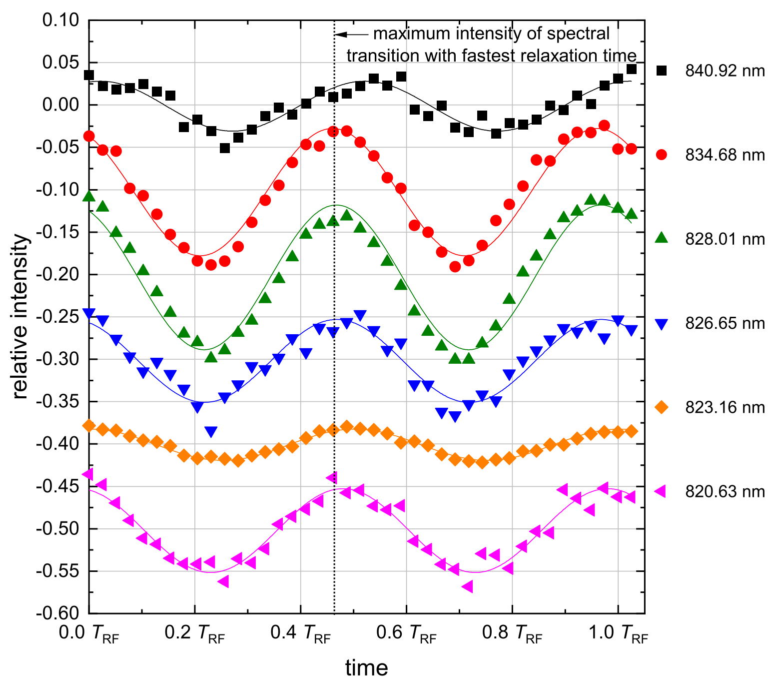

Fig. 7 Time evolution of the intensities obtained from a series of spectra taken at different time delays. The average spectrum of this series is shown in Fig. 4. The intensities are divided by the corresponding average line intensity and shifted by 0.1 towards each other for better visibility. The local maximum of the spectral transition with the fastest relaxation time is indicated by the dashed line. The slower spectral transitions show a small phase shift of approximately 10 to 30 ns (except 840.92 nm, where it is slightly more). The radio frequency driving the plasma was 1.281 MHz, so $T_{RF} = 780$ ns

time and weakest at times when the electric field crosses zero, resulting in an oscillation with twice the radio frequency as visible in Fig. 7.

Assuming that the time response of the electron system to changes of the RF excitation is faster than 20 ns, we can assume that each emission spectrum taken at a specific time delay is characterized by a set of plasma parameters. Thus, time-resolved OES measurements like those shown in Fig. 7 can be evaluated using the correlation method described above to obtain the time-evolution of the plasma parameters during one RF cycle. However, it should be noted that some of the excitation and relaxation processes leading to the optical spectra possess characteristic times on the nanosecond scale leading to a phase shift between the cosine curves describing the intensity variation in Fig. 7. If a relaxation time is very long compared to the oscillation period, the phase of the oscillation will lack behind and its amplitude will flatten, eventually down to zero [11–13]. When comparing the oscillations of the 840.92 nm and the 828.01 nm lines in Fig. 7, which have 327 ns and 27.1 ns [43] relaxation times, respectively (see Fig. 4 or Table 1), this effect already starts to occur. A similar phase shift can be observed for the 823.16 nm line which has a relaxation time of 35.0 ns [43]. This is still short compared to the approximately 390 ns oscillation period and indicates, that the upper level of the 823.16 nm line is not excited directly, but is fed through one or several higher lying electronic states with longer relaxation times, as shown in Fig. 4 or Table 1. The free electrons are able to follow the RF, so the excitation of the electronic states should follow, too. The relaxation of the electronic states on the other hand cannot necessarily follow. For now, we will assume that the evaluation of the time-resolved optical spectra is a valid approach, since the phase shift of the intensity oscillations in Fig. 7 against each other of approximately 10 to 30 ns are rather short compared to the oscillation period of, in this case, 390 ns. Whether this leads to a reliable determination of time-resolved plasma parameters has yet to be verified, for instance, by a PIC (particle in cell) modeling of the microscopic processes inside the plasma. A set of lines with faster relaxation times or lower RF frequencies will reduce the errors made.

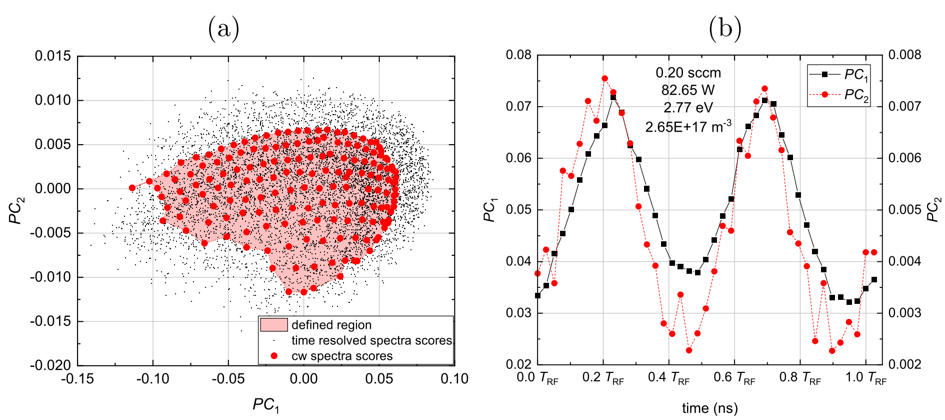

Fig. 8 PCA scores of the time-resolved optical emission measurements for a xenon plasma driven with 1.2 MHz RF excitation (**a**). The defined region that is mapped by the scores of the cw optical emission spectra from which the correlation has been established is shown in red. Scores of time-resolved spectra outside this region cannot reliably be used to estimate plasma parameters as they lie outside the area where the one-to-one correlation was established and fitted. Plasma parameters extracted from the fitting in this range are uncertain. The oscillation of the PCA scores as a function of delay time is shown in (**b**) for a series of time-resolved spectra. Mass flow, RF input power and average electron temperature and density are given in the plot. PC_1 and PC_2 oscillate with twice the radio frequency as the corresponding line intensities in Fig. 7

To extract the time evolution of the plasma parameters from the optical emission spectra taken at different time delays, the PCA scores for the series of spectra need to be calculated with respect to the PCA eigenvectors derived from the cw measurements. The PCA scores are obtained by scalar multiplication with the PCA eigenvectors of the cw measurements as described in equation (3) and are shown in Fig. 8a. It can already be seen that some PCA scores in Fig. 8a lie outside of the mapped area of the cw data for which the correlation with the plasma parameters was established by the fits. Therefore, the plasma parameters extracted for these data points employing the fitted correlation will be rather unreliable. Nevertheless, plotting the scores of the PC_1 and PC_2 values obtained as a function of delay time yields an oscillating behavior with twice the radio frequency (see Fig. 7b).

With the PCA scores calculated the polynomial fitting functions describing the parameter surfaces in Fig. 6c and d are used to translate these scores into plasma parameters as described by Eq. (7). This way, the time evolution of the plasma parameters during one RF cycle can be obtained. Some examples of such time evolutions are shown in Fig. 9. Note that some measurements yield rather stable results, while others are mostly estimations since their PCA-scores are outside the reliable region defined by the cw measurements shown in Fig. 8a. In Fig. 9a it can be seen that the amplitude of the electron density oscillation during an RF cycle increases with increasing average electron density, i.e., with increasing RF input power. The electron temperature in Fig. 9b, on the other hand, is almost constant over the RF cycle for the curves obtained from series of spectra at higher RF input power. In contrast, the two curves obtained from series of spectra at lower input power exhibit strong oscillations. Such strong oscillations in electron temperature may lead to a sputtering rate of the RIT screen grid that is higher than anticipated from the average electron temperature.

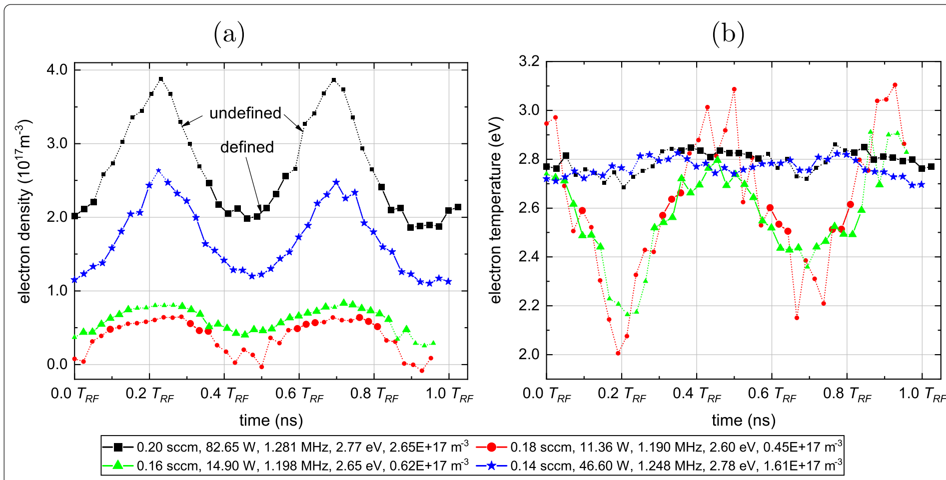

Fig. 9 Plots of the time evolution of electron density (**a**) and temperature (**b**) for a xenon plasma driven by 1.2 MHz RF excitation for various operation parameters calculated from the PCA scores (see Fig. 8b) of time-resolved optical spectra (see Fig. 7). Mass flow, RF input power, frequency as well as average electron temperature and density are given in the legend. Parameters resulting from data points outside the mapped region (see Fig. 8a) are ill defined and plotted as smaller symbols connected by a dotted line. The plasma parameters oscillate with twice the radio frequency

Conclusion

A method of non-invasively extracting plasma parameters from an OES using a correlation based on a reference data set of simultaneously recorded optical emission spectra and Langmuir measurements has been presented and validated. The method utilizes the high sensitivity of a PCA to detect small and multi-dimensional changes occurring in the emission spectra of the plasma inside an ion thruster at different operational points. The PCA results are fitted to plasma parameters obtained by Langmuir measurements yielding a one-to-one correlation. Using this correlation, plasma parameters can be determined with just the non-invasive OES measurement. We have also demonstrated that our correlation approach can be used to monitor the time-evolution of the plasma parameters in an RF plasma, electron temperature and density, during an RF cycle. Knowledge of the time dependence of plasma parameters will help to identify critical operation points of RITs and other thrusters and to optimize their performance. Furthermore, it will yield valuable input parameters for theory, i.e., help to further develop theoretical models of such thrusters. In addition, the approach is not restricted to xenon as propellant and may be also employed in case of alternative propellants such as krypton or iodine. Typically, the plasma parameters also vary spatially inside a macroscopic plasma vessel. Thus, the approach described has the potential to spatially resolve the distribution of plasma parameters inside a plasma vessel. Carefully conducted, our approach provides a powerful tool for determining the plasma parameters non-invasively by OES without having to rely on microscopic modeling.

Abbreviations

RIT: Radio-frequency Ion Thruster; OES: Optical Emission Spectroscopy; PCA: Principal Component Analysis; PC: Principal Component; EP: Electric Propulsion; ICCD: Intensified Charge-Coupled Device; cw: continuous wave; RFG: Radio-Frequency Generator; RF: Radio-Frequency; MFC: mass flow controller; NIST: National Institute of Science and Technology; EEDF: Electron Energy Distribution Function

Acknowledgements

Benny Nauschütt is grateful for receiving a PhD studentship in the framework of the JLU-Ariane Group Graduate School "Radiofrequency ion thrusters".

Authors' contributions

BN wrote the manuscript and performed and evaluated the measurements. LC assisted in evaluating the OES measurements using PCA. KH and PJK supervised the activities and provided the idea for the experiment. All authors contributed to data interpretation and discussion. All authors read and approved the final manuscript.

Funding

Open Access funding enabled and organized by Projekt DEAL.

Availability of data and materials

The data sets used and/or analyzed during the current study are available from JLUdata under the link "http://dx.doi.org/10.22029/jlupub-54".

Declarations

Ethics approval and consent to participate

Not applicable.

Consent for publication

All authors agree to the publication of the article.

Competing interests

The authors declare that they have no competing interests.

Received: 31 May 2021 Accepted: 17 July 2021
Published online: 05 August 2021

References

1. Mazouffre S. Electric propulsion for satellites and spacecraft: established technologies and novel approaches. Plasma Sources Sci Technol. 2016;25(3):033002. https://doi.org/10.1088/0963-0252/25/3/033002.
2. Holste K, Dietz P, Scharmann S, Keil K, Henning T, Zschätzsch D, Reitemeyer M, Nauschütt B, Kiefer F, Kunze F, Zorn J, Heiliger C, Joshi N, Probst U, Thüringer R, Volkmar C, Packan D, Peterschmitt S, Brinkmann K-T, Zaunick H-G, Thoma MH, Kretschmer M, Leiter HJ, Schippers S, Hannemann K, Klar PJ. Ion thrusters for electric propulsion: Scientific issues developing a niche technology into a game changer. Rev Sci Instrum. 2020;91(6):061101. https://doi.org/10.1063/5.0010134.
3. Löb H. Ein elektrostatisches Raketentriebwerk mit Hochfrequenzionenquelle. Astronautica Acta. 1962;8(1):49.
4. Löb H, Freisinger J. Ionenraketen. Braunschweig: Vieweg+Teubner Verlag; 1967.
5. Goebel DM, Katz I. Fundamentals of Electric Propulsion. 1st ed. Hoboken: Wiley; 2008.
6. Demidov VI, Ratynskaia SV, Rypdal K. Electric probes for plasmas: The link between theory and instrument. Rev Sci Instrum. 2002;73(10):3409–39. https://doi.org/10.1063/1.1505099.
7. Benedikt J, Kersten H, Piel A. Foundations of measurement of electrons, ions and species fluxes toward surfaces in low-temperature plasmas. Plasma Sources Sci Technol. 2021;30(3):033001. https://doi.org/10.1088/1361-6595/abe4bf.
8. Abdi H, Williams LJ. Principal component analysis. Wiley Interdiscip Rev Comput Stat. 2010;2(4):433–59. https://doi.org/10.1002/wics.101.
9. Tartz M, Hartmann E, Neumann H. Evolution of Extraction Grid Erosion with Operation Time. In: 40th AIAA/ASME/SAE/ASEE Joint Propulsion Conference and Exhibit. American Institute of Aeronautics and Astronautics; 2004. https://doi.org/10.2514/6.2004-3787.
10. Sangregorio M, Xie K, Wang N, Guo N, Zhang Z. Ion engine grids: Function, main parameters, issues, configurations, geometries, materials and fabrication methods. Chin J Aeronaut. 2018;31(8):1635–49. https://doi.org/10.1016/j.cja.2018.06.005.
11. de Rosny G, Mosburg ER, Abelson JR, Devaud G, Kerns RC. Evidence for a time dependent excitation process in silane radio frequency glow discharges. J Appl Phys. 1983;54(5):2272–5. https://doi.org/10.1063/1.332381.
12. Gottscho RA, Miller TA. Optical techniques in plasma diagnostics. Pure Appl Chem. 1984;56(2):189–208. https://doi.org/10.1351/pac198456020189.
13. Flamm DL, Donnelly VM. Time-dependent excitation in high- and low-frequency chlorine plasmas. J Appl Phys. 1986;59(4):1052–62. https://doi.org/10.1063/1.336541.
14. Schulze J, Schüngel E, Donkó Z, Luggenhölscher D, Czarnetzki U. Phase resolved optical emission spectroscopy: a non-intrusive diagnostic to study electron dynamics in capacitive radio frequency discharges. J Phys D Appl Phys. 2010;43(12):124016. https://doi.org/10.1088/0022-3727/43/12/124016.
15. Vlcek J. A collisional-radiative model applicable to argon discharges over a wide range of conditions. I, Formulation and basic data. J Phys D Appl Phys. 1989;22(5):623–31. https://doi.org/10.1088/0022-3727/22/5/009.
16. Vlcek J, Pelikan V. A collisional-radiative model applicable to argon discharges over a wide range of conditions. II, application to low-pressure, hollow-cathode arc and low-pressure glow discharges. J Phys D Appl Phys. 1989;22(5): 632–43. https://doi.org/10.1088/0022-3727/22/5/010.
17. Bogaerts A, Gijbels R, Vlcek J. Collisional-radiative model for an argon glow discharge. J Appl Phys. 1998;84(1): 121–36. https://doi.org/10.1063/1.368009.
18. Bogaerts A, Gijbels R, Vlcek J. Modeling of glow discharge optical emission spectrometry: Calculation of the argon atomic optical emission spectrum. Spectrochim Acta B At Spectrosc. 1998;53(11):1517–26. https://doi.org/10.1016/s0584-8547(98)00139-6.
19. Iordanova S, Koleva I. Optical emission spectroscopy diagnostics of inductively-driven plasmas in argon gas at low pressures. Spectrochim Acta B Atomic Spectrosc. 2007;62(4):344–56. https://doi.org/10.1016/j.sab.2007.03.026.
20. Tian-Ye N, Jin-Xiang C, Lei L, Jin-Ying L, Yan W, Liang W, You L. A comparison among optical emission spectroscopic methods of determining electron temperature in low pressure argon plasmas. Chin Phys. 2007;16(9): 2757–63. https://doi.org/10.1088/1009-1963/16/9/043.
21. Canal GP, Luna H, Galvão RMO, Castell R. An approach to a non-LTE Saha equation based on the Druyvesteyn energy distribution function: a comparison between the electron temperature obtained from OES and the Langmuir probe analysis. J Phys D Appl Phys. 2009;42(13):135202. https://doi.org/10.1088/0022-3727/42/13/135202.
22. Boffard JB, Lin CC, DeJosephJr CA. Application of excitation cross sections to optical plasma diagnostics. J Phys D Appl Phys. 2004;37(12):143–61. https://doi.org/10.1088/0022-3727/37/12/r01.
23. Boffard JB, Jung RO, Lin CC, Aneskavich LE, Wendt AE. Argon 420.1–419.8 nm emission line ratio for measuring plasma effective electron temperatures. J Phys D Appl Phys. 2012;45(4):045201. https://doi.org/10.1088/0022-3727/45/4/045201.
24. Boffard JB, Jung RO, Lin CC, Wendt AE. Optical emission measurements of electron energy distributions in low-pressure argon inductively coupled plasmas. Plasma Sources Sci Technol. 2010;19(6):065001. https://doi.org/10.1088/0963-0252/19/6/065001.
25. Zhu X-M, Chen W-C, Li J, Pu Y-K. Determining the electron temperature and the electron density by a simple collisional–radiative model of argon and xenon in low-pressure discharges. J Phys D Appl Phys. 2008;42(2):025203. https://doi.org/10.1088/0022-3727/42/2/025203.
26. Zhu X-M, Pu Y-K. Optical emission spectroscopy in low-temperature plasmas containing argon and nitrogen: determination of the electron temperature and density by the line-ratio method. J Phys D Appl Phys. 2010;43(40): 403001. https://doi.org/10.1088/0022-3727/43/40/403001.
27. Zhu X-M, Pu Y-K, Celik Y, Siepa S, Schüngel E, Luggenhölscher D, Czarnetzki U. Possibilities of determining non-Maxwellian EEDFs from the OES line-ratios in low-pressure capacitive and inductive plasmas containing argon and krypton. Plasma Sources Sci Technol. 2012;21(2):024003. https://doi.org/10.1088/0963-0252/21/2/024003.
28. Siepa S, Danko S, Tsankov TV, Mussenbrock T, Czarnetzki U. On the OES line-ratio technique in argon and argon-containing plasmas. J Phys D Appl Phys. 2014;47(44):445201. https://doi.org/10.1088/0022-3727/47/44/445201.

29. Chiu Y, Austin BL, Williams S, Dressler RA, Karabadzhak GF. Passive optical diagnostic of Xe-propelled Hall thrusters. I, Emission cross sections. J Appl Phys. 2006;99(11):113304. https://doi.org/10.1063/1.2195018.
30. Karabadzhak GF, Chiu Y, Dressler RA. Passive optical diagnostic of Xe propelled Hall thrusters. II, Collisional-radiative model. J Appl Phys. 2006;99(11):113305. https://doi.org/10.1063/1.2195019.
31. Sommerville J, King L. An Optical Diagnostic for Xenon Hall Thrusters Including Metastable Contributions. In: 42nd AIAA/ASME/SAE/ASEE Joint Propulsion Conference & Exhibit. American Institute of Aeronautics and Astronautics; 2006. https://doi.org/10.2514/6.2006-4823.
32. Dressler RA, Chiu Y, Zatsarinny O, Bartschat K, Srivastava R, Sharma L. Near-infrared collisional radiative model for Xe plasma electrostatic thrusters: the role of metastable atoms. J Phys D Appl Phys. 2009;42(18):185203. https://doi.org/10.1088/0022-3727/42/18/185203.
33. Yang J, Yokota S, Kaneko R, Komurasaki K. Diagnosing on plasma plume from xenon Hall thruster with collisional-radiative model. Phys Plasmas. 2010;17(10):103504. https://doi.org/10.1063/1.3486530.
34. Wei L-Q, Li W-B, Ding Y-J, Zhu X-M, Wang Y-F, Hu J-F, Yan S-L, Yu D-R. A photographic method for in-orbit measurement of electron temperature distribution in the plume of Hall thrusters. Plasma Sources Sci Technol. 2018;27(8):084002. https://doi.org/10.1088/1361-6595/aad4cd.
35. Zhu X-M, Chen W-C, Pu Y-K. Gas temperature, electron density and electron temperature measurement in a microwave excited microplasma. J Phys D Appl Phys. 2008;41(10):105212. https://doi.org/10.1088/0022-3727/41/10/105212.
36. Zhu X-M, Wang Y-F, Wang Y, Yu D-R, Zatsarinny O, Bartschat K, Tsankov TV, Czarnetzki U. A xenon collisional-radiative model applicable to electric propulsion devices: II, Kinetics of the 6s, 6p, and 5d states of atoms and ions in Hall thrusters. Plasma Sources Sci Technol. 2019;28(10):105005. https://doi.org/10.1088/1361-6595/ab30b7.
37. Wang Y, Wang Y-F, Zhu X-M, Zatsarinny O, Bartschat K. A xenon collisional-radiative model applicable to electric propulsion devices: I, Calculations of electron-impact cross sections for xenon ions by the Dirac B-spline R-matrix method. Plasma Sources Sci Technol. 2019;28(10):105004. https://doi.org/10.1088/1361-6595/ab3125.
38. Priti, Gangwar RK, Srivastava R. Collisional-radiative model of xenon plasma with calculated electron-impact fine-structure excitation cross-sections. Plasma Sources Sci Technol. 2019;28(2):025003. https://doi.org/10.1088/1361-6595/aaf95f.
39. Holste K, Gärtner W, Zschätzsch D, Scharmann S, Köhler P, Dietz P, Klar PJ. Performance of an iodine-fueled radio-frequency ion-thruster. Eur Phys J D. 2018;72(1):. https://doi.org/10.1140/epjd/e2017-80498-5.
40. Dietz P, Gärtner W, Koch Q, Köhler PE, Teng Y, Schreiner PR, Holste K, Klar PJ. Molecular propellants for ion thrusters. Plasma Sources Sci Technol. 2019;28(8):084001. https://doi.org/10.1088/1361-6595/ab2c6c.
41. Saloman EB. Energy Levels and Observed Spectral Lines of Xenon, Xe I through Xe LIV. J Phys Chem Ref Data. 2004;33(3):765–921. https://doi.org/10.1063/1.1649348.
42. Johnson EO, Malter L. A Floating Double Probe Method for Measurements in Gas Discharges. Phys Rev. 1950;80(1):58–68. https://doi.org/10.1103/physrev.80.58.
43. Kramida A, Ralchenko Y. NIST Atomic Spectra Database, NIST Standard Reference Database 78: National Institute of Standards and Technology; 1999. https://doi.org/10.18434/T4W30F.
44. Izenman AJ. Linear Discriminant Analysis. In: Modern Multivariate Statistical Techniques. In: Springer Texts in Statistics. Springer; 2013. p. 237–80. https://doi.org/10.1007/978-0-387-78189-1_8.
45. Pauca VP, Piper J, Plemmons RJ. Nonnegative matrix factorization for spectral data analysis. Linear Algebra Appl. 2006;416(1):29–47. https://doi.org/10.1016/j.laa.2005.06.025.
46. Gorsuch RL. Factor Analysis: Psychology Press; 2013. https://doi.org/10.4324/9780203781098.
47. Boffard JB, Jung RO, Lin CC, Aneskavich LE, Wendt AE. Optical diagnostics for characterization of electron energy distributions: argon inductively coupled plasmas. Plasma Sources Sci Technol. 2011;20(5):055006. https://doi.org/10.1088/0963-0252/20/5/055006.

Publisher's Note

Springer Nature remains neutral with regard to jurisdictional claims in published maps and institutional affiliations.

Journal of Applied Physics ARTICLE scitation.org/journal/jap

Combination of optical emission spectroscopy and multivariate data analysis techniques as a versatile non-invasive tool for characterizing xenon/krypton mixed gas plasma inside operating ion thrusters

Cite as: J. Appl. Phys. **131**, 053301 (2022); doi: 10.1063/5.0074412
Submitted: 8 October 2021 · Accepted: 11 January 2022 ·
Published Online: 2 February 2022

View Online Export Citation CrossMark

Benny Nauschütt,[a)] Limei Chen, Kristof Holste, and Peter J. Klar

AFFILIATIONS

Institute of Experimental Physics I and Center of Materials Research (ZfM/Lama), Justus Liebig University, Heinrich-Buff-Ring 16, 35392 Giessen, Germany

Note: This paper is part of the Special Topic on Physics of Electric Propulsion.

[a)]**Author to whom correspondence should be addressed:** Benny.Nauschuett@physik.uni-giessen.de

ABSTRACT

Non-invasive assessment of the plasma parameters is a useful tool for a reliable characterization of many electric thrusters for space applications. Due to high costs, limited availability, and growing use of electric propulsion in spaceflight, alternatives to Xe as a propellant are becoming increasingly important. One option is to use the lighter noble gas krypton or xenon/krypton gas mixtures as a propellant. We propose a versatile analytical approach for establishing empirical correlations between plasma parameters and optical emission (OE) spectroscopy utilizing principal component analysis (PCA). Our approach allows us to establish a surjective mapping of individual OE spectra via their PCA scores onto the corresponding plasma parameters. We prove the feasibility of this approach for Xe, Kr, and Xe/Kr mixed plasmas demonstrating that it is applicable for a wide range of propellant candidates. A major advantage is that the approach does not rely on any microscopic modeling of the OE spectra of the plasma. After having established corresponding reference mappings, the approach can be explored for determining non-invasively and spatially resolved plasma parameters of the propellant plasma of various kinds of operating ion thrusters, which operate in the same plasma regime as the reference plasma. Thus, this method may contribute to shorter qualification and testing times of ion thrusters.

I. INTRODUCTION

Nowadays, electric propulsion (EP) systems are an established option as spacecraft engines.[1,2] While they deliver less thrust compared to their chemical counterpart, EP systems excel due to their high fuel efficiency and the vast number of usable propellants yielding a large variability for implementing them in space mission scenarios. There are many types of EP thrusters that generate a propellant plasma in the process of generating thrust. To optimize a thruster without disturbing the plasma, it is favorable to characterize the plasma non-invasively.[3,4] Currently, mainly, xenon is used as a propellant due to its high mass, chemical inertness, and fairly low ionization energy. However, xenon is also a rare resource and correspondingly expensive.[5,6] Thus, alternatives are sought, such as diluting or replacing xenon with the lighter and ten times more abundant noble gas krypton.[7–12] However, the properties of the plasma operated inside the thruster will change when altering the propellant used. Consequently, the operational points of the thruster need to be adjusted. This re-optimization may even require hardware adaptations.[7,11,12]

The radio-frequency ion thruster (RIT) is one of these established EP systems and was developed at the Justus Liebig University of Giessen in the 1960s.[13,14] The plasma discharge in a RIT is achieved by inductive heating of the electrons. When leaving the thruster, positive ions are accelerated by at least two extraction grids to generate a directed ion beam and, therefore, thrust according to Newton's third law.[1,2,15] The functioning of the ion optics of a RIT is determined by the interplay of plasma parameters of the propellant plasma inside the discharge vessel and the grid system. In other words, the geometry of the grid system alone does not define the ion optics. The shape of the plasma meniscus at the grid apertures of the screen grid depends on the plasma parameters and determines the divergence of the ion beamlet inside the grid system.[15] A wrong ion beam focusing leads to grid erosion by direct impingement and may drastically reduce the thruster's lifetime. Knowledge of the plasma parameters, in particular, electron temperature and density, at the actual operational points of the thruster is essential for a successful optimization of the thruster's performance.[15] During thruster qualification, non-invasive diagnostics, such as beam diagnostics, thrust measurement, performance data, and post- or mid-test erosion analysis, are commonly used to obtain information on the operating thruster.[16–18] In principle, invasive electrical probes can be used to determine plasma parameters[19,20] but are typically undesirable during qualification, as they may itself alter the plasma and, thus, affect the thruster's performance.[19] The plasma of gridded ion thrusters, in particular, will usually not be accessible with invasive probes, if no dedicated openings are available, since such extra openings are not desirable in a flight model; i.e., the grid system or the discharge vessel should not be altered.

Non-invasive alternatives for plasma characterization inside gridded ion thrusters need to be sought. A possible non-invasive diagnostics option is optical emission spectroscopy (OES), which can be used to assess plasma parameters of both beam and discharge by the application of a theoretical plasma model.[4,21–28] We recently introduced a method that utilizes non-invasive OES to assess plasma parameters of a thruster operating with xenon non-invasively by applying an empirical correlation between plasma parameters and OES instead of a theoretical model.[29] This method utilizes a principal component analysis (PCA)[30] and does not rely on any microscopic input other than the measurement of plasma parameters and OE spectra in a reference setup. Since it only requires optical access to the plasma, an OES-based method may be used during terrestrial testing for thruster development or space qualification in cases where an invasive probe cannot be employed. With the plasma parameters provided by this method, grid erosion can be estimated during testing already in the case of gridded ion thrusters. Depending on the type of thruster, an optical probe can be placed strategically to avoid interaction with the plume, allowing one to monitor the thruster with OES and beam diagnostics simultaneously. The high spatial resolution achievable in optical spectroscopy may allow establishing spatial maps of the plasma parameters of an inhomogeneous plasma. An example, where this may be of interest, is the mapping of the radial distribution of plasma parameters inside the discharge vessel of gridded ion thrusters, such as RITs.

In principle, plasma parameters can be extracted from OES using theoretical modeling of the electronic states of the atoms and ions responsible for the optical emission. Such theoretical plasma models can be found, e.g., for argon[31–44] and xenon,[4,21,22,24–27,41,45–47] but rarely for gas mixtures where even more microscopic processes need to be accounted for in order to obtain a reliable description. There are some studies in which theoretical models were applied to gas mixtures, but those focus on electron excitation only.[41,48–51] One exception is Ref. 52, which also considers several atom and molecule collision mechanisms. Such theoretical models are typically set up with a specific application in mind. The specifics of the application will be reflected by the number of electronic states and the selection of the microscopic processes between the species of the plasma, which are taken into account. Taking xenon as an example, Ref. 53 lists 443 electronic states just for neutral xenon, 161 for Xe^{+}, 157 for Xe^{2+}, and more for even higher ionization levels. The amount of electronic states used for theoretical models varies, e.g., 173 states in Ref. 24 or 38 states in Ref. 47. This means that the models are not easily transferable to other applications where the macroscopic excitation and discharge conditions of the plasma have changed. In particular, this also applies for gas mixtures. Adding another atomic species to a propellant, such as krypton to xenon, requires an accurate description of the electronic states of both species and corresponding ions similar to Refs. 41, 48, and 52. Furthermore, an entirely different set of microscopic processes between the xenon and krypton species comes into play, as for describing xenon–krypton collisions and excitation transfer.[54–58] A mixed gas model that includes such transfer mechanisms for argon and nitrogen is shown in Ref. 52. The missing parameters, such as cross sections, etc., are difficult to predict with *ab initio* theories and hard to determine experimentally.[59–64]

Here, we demonstrate that our non-invasive approach for determining plasma parameters is easily transferable to more sophisticated plasmas, such as those of gas mixtures of xenon and krypton. In future studies, this method might be applied to iodine plasmas as well, as iodine is another promising alternative to xenon as a propellant.[65,66] We demonstrate that the challenges met when attempting a microscopic description of such plasmas can be circumvented by our approach, and the plasma parameters can be reliably extracted.

II. EXPERIMENTAL DETAILS

The experimental setup used is shown in Fig. 1. The plasma is generated in a cylindrical RIT-10 (10 cm diameter) quartz glass

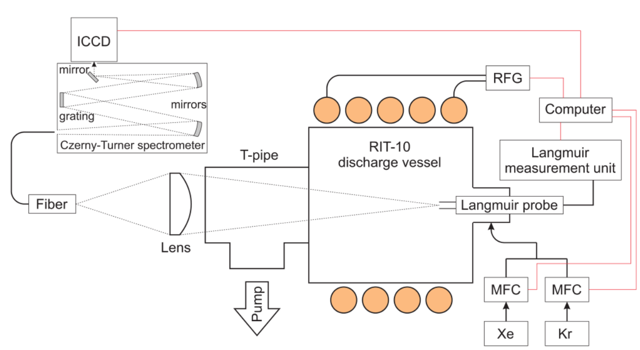

FIG. 1. Experimental setup for simultaneous measurement of the optical emission spectrum and the plasma parameters via a Langmuir double probe at the same position. The connections to the computer are shown as red lines. The setup is a modified version of the setup used in the previous work[29] yielding higher accuracy and allowing for the operation with mixed gases.

discharge vessel. The vessel has no extraction system and is operated without surrounding vacuum. Only the inside of the vessel is evacuated via the opening that holds the extraction system in a thruster arrangement. The magnetic field generated by the rf coil with six windings surrounding the vessel is not affected by the exposure to air as the relative permittivity of air and vacuum is almost identical.[67] The gas inlet is mounted on the opposite side of the vessel and also contains the Langmuir double probe to determine the electron temperature T_e and density n_e.[19,20,68,69]

The probe diagnostics were realized with a Keysight B2901A Precision Source/Measurement Unit as a four-wire measurement. The measurement range was -100 to 100 V (potential difference between the two probe wires) with voltage steps of 0.1 V and an integration time of 50 ms. The uncertainty for voltage and current measurement is given in the data sheet of the instrument with $\pm 0.015\%$ and $\pm 0.02\%$, respectively. The Langmuir probe was built in-house and consists of two cylindrical wires of length 6.90 ± 0.1 mm and a radius of 0.125 ± 0.0125 mm. The spacing between the wires was 1.425 ± 0.025 mm.

The optical access to the discharge vessel is given by a glass window, and the focus of the detection optics is positioned in close vicinity of the Langmuir probe. The omission of the extraction system probably causes differences in the gas density distribution. Therefore, it is important to perform OES and Langmuir diagnostics on the same spot so that the correlation can be transferred to a real thruster with different gas density distributions with minimal error. The used 0.5 m Czerny–Turner spectrometer is connected to an intensified charge-coupled device (ICCD) camera (Princeton Instruments PI-MAX 4 1024f). The ICCD is capable of both continuous-wave (cw) and time-resolved measurements on the nanosecond scale but was only used for cw-measurements here. We chose a spectral window from 808 to 837 nm as it contains some of the fastest decaying spectral transitions for both neutral xenon and krypton.[70] Examples for xenon and krypton spectra are shown in Fig. 2. The observed optical transitions and feeding transitions of a potential transition chain are listed in Table I. All of the observed spectral transitions have relaxation times shorter than the period of the rf cycle, most of them by about an order of magnitude. The spectral resolution in the observed wavelength region is approximately 28 pm/pixel. The spectra were measured with 500 µs integration time and were averaged 10 000 times. The ICCD's intensifier was set to 1. We found a standard deviation of 1%–2% relative to the average counts for the background region and up to 5% at the peak positions. The response correction was performed with an AVALIGHT-HAL-CAL-MINI calibration source. The gas flow into the discharge vessel is controlled by a set of gas flow controllers (MFC), one for xenon (Bronkhorst EL-Flow F-200CV-AAA-11-V) and another for krypton (Bronkhorst EL-Flow select F-200CV-002-AAD-00-V). Both MFCs have a maximum flow range of 1.5 sccm xenon. The MFC calibration with the used gases (Kr 5.0 and Xe 4.0) was performed with a Mettler Toledo ME503T/00 scale with a mounted gas reservoir. In this calibration process, the reservoir is evacuated and then filled by setting a constant mass flow on the MFC under calibration. The measured weight is recorded until a total mass of 150 mg is accumulated. This measurement was done for four different gas flows for both MFCs. A linear fit of the weight over time measurements yields the

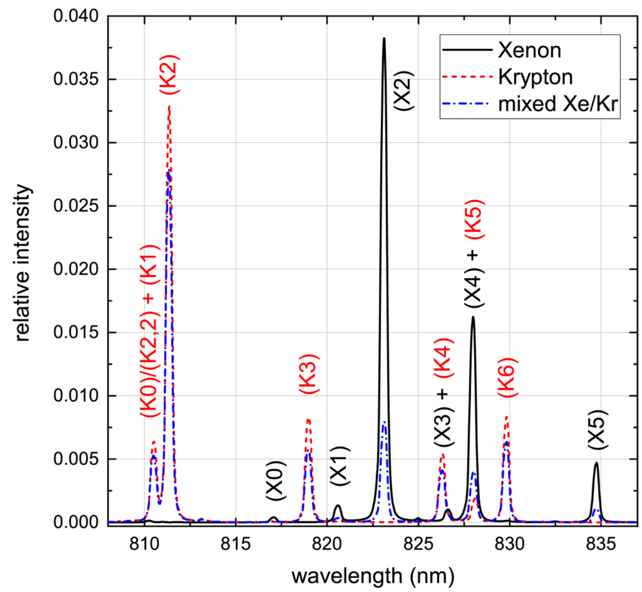

FIG. 2. Example spectra for both xenon and krypton as well as mixed gas plasma. Additional information about the individual lines can be found in Table I. The shown spectra are intensity-normalized.

actual gas flow. A linear fit of the actual gas flows over the nominal gas flows yields the calibration function. The accuracy of the calibration was about 0.1 % for xenon and about 1.5 % for krypton. The plasma was excited by a half-bridge radio-frequency generator (RFG)[71,72] at a resonance frequency around 1.6 MHz corresponding to a period of the rf cycle of 625 ns. The RFG input power was delivered by an Aim TTi CPX400DP power source, and the frequency was measured with a GW Instek GDS-2204E oscilloscope. The RFG input power was varied while keeping the gas flow constant. The experiments were performed for various combinations of xenon and krypton gas flows. The plasma was operated for 5 min at each operational point before starting the measurement to ensure thermal stability during roughly 2 min of measurement time. After changing the gas flow settings, the plasma was allowed to settle for 12 min before commencing the measurements.

In a previously conducted measurement series, we used the glass vessel with an easy optical access to the plasma from behind.[29] The setup was rearranged and improved in order to allow detection of the plasma emission from a spot close to the Langmuir probe. The rearrangement of the setup further increases the reliability of the measurement approach. The previously used spectral window from 820 to 840 nm[29] was shifted slightly toward shorter wavelengths (808–837 nm), thus sacrificing one small xenon line in favor of a strong krypton double line (K0+K1 and K2 in Fig. 2).

A. Principal component analysis

To analyze the behavior of the relative line intensities for different operational points of the plasma of a species or gas mixture, we

TABLE I. Wavelengths, relaxation times, intensities, and the involved electronic states of the observed transitions shown in Fig. 2 are listed for both xenon[53,70] and krypton.[70,73] The listed intensities are only the qualitative values from Refs. 53 and 73. Using the index, the transitions can be found in Fig. 2. The observed transitions are also shown in bold.

				Lower level			Upper level		
Index	Wavelength (nm)	Relaxation time (ns)	Intensity	Configuration	Term	J	Configuration	Term	J
(X0)	**817.10**	**n.a.**	**100**	$\boldsymbol{5p^5(^2P^\circ_{3/2})6p}$	$\boldsymbol{^2[3/2]}$	**2**	$\boldsymbol{5p^5(^2P^\circ_{1/2})5d}$	$\boldsymbol{^2[3/2]^\circ}$	**2**
(X0,1)	722.26	n.a.	20	$5p^5(^2P^\circ_{1/2})5d$	$^2[3/2]^\circ$	2	$5p^5(^2P^\circ_{1/2})6f$	$^2[5/2]$	3
(X0,2)	800.96	n.a.	30	$5p^5(^2P^\circ_{1/2})5d$	$^2[3/2]^\circ$	2	$5p^5(^2P^\circ_{1/2})5f$	$^2[5/2]$	3
(X1)	**820.63**	**50**	**700**	$\boldsymbol{5p^5(^2P^\circ_{1/2})6s}$	$^2[1/2]^\circ$	**0**	$\boldsymbol{5p^5(^2P^\circ_{1/2})6p}$	$\boldsymbol{^2[3/2]}$	**1**
(X1,1)	3605.49	1700	20	$5p^5(^2P^\circ_{1/2})6p$	$^2[3/2]$	1	$5p^5(^2P^\circ_{1/2})5d$	$^2[5/2]^\circ$	2
(X2)	**823.16**	**35**	**10000**	$\boldsymbol{5p^5(^2P^\circ_{3/2})6s}$	$\boldsymbol{^2[3/2]^\circ}$	**2**	$\boldsymbol{5p^5(^2P^\circ_{3/2})6p}$	$^2[3/2]$	**2**
(X2,1)	3107.77	1400	6000	$5p^5(^2P^\circ_{3/2})6p$	$^2[3/2]$	2	$5p^5(^2P^\circ_{3/2})5d$	$^2[5/2]^\circ$	3
(X2,2)	1672.82	556	5000	$5p^5(^2P^\circ_{3/2})6p$	$^2[3/2]$	2	$5p^5(^2P^\circ_{3/2})7s$	$^2[3/2]^\circ$	2
(X2,3)	739.38	204	150	$5p^5(^2P^\circ_{3/2})6p$	$^2[3/2]$	2	$5p^5(^2P^\circ_{3/2})7d$	$^2[5/2]^\circ$	3
(X3)	**826.65**	**61.7**	**500**	$\boldsymbol{5p^5(^2P^\circ_{1/2})6s}$	$^2[1/2]^\circ$	**1**	$\boldsymbol{5p^5(^2P^\circ_{1/2})6p}$	$\boldsymbol{^2[1/2]}$	**1**
(X3,1)	4610.87	3700	1	$5p^5(^2P^\circ_{1/2})6p$	$^2[1/2]$	1	$5p^5(^2P^\circ_{1/2})5d$	$^2[3/2]^\circ$	2
(X4)	**828.01**	**27.1**	**7000**	$\boldsymbol{5p^5(^2P^\circ_{3/2})6s}$	$\boldsymbol{^2[3/2]^\circ}$	**1**	$\boldsymbol{5p^5(^2P^\circ_{3/2})6p}$	$\boldsymbol{^2[1/2]}$	**0**
(X4,1)	1878.82	1100	860	$5p^5(^2P^\circ_{3/2})6p$	$^2[1/2]$	0	$5p^5(^2P^\circ_{3/2})7s$	$^2[3/2]^\circ$	1
(X4,2)	2651.77	6300	30	$5p^5(^2P^\circ_{3/2})6p$	$^2[1/2]$	0	$5p^5(^2P^\circ_{3/2})5d$	$^2[3/2]^\circ$	1
(X5)	**834.68**	**24**	**2000**	$\boldsymbol{5p^5(^2P^\circ_{1/2})6s}$	$\boldsymbol{^2[1/2]^\circ}$	**1**	$\boldsymbol{5p^5(^2P^\circ_{1/2})6p}$	$\boldsymbol{^2[3/2]}$	**2**
(X5,1)	3869.68	1900	200	$5p^5(^2P^\circ_{1/2})6p$	$^2[3/2]$	2	$5p^5(^2P^\circ_{1/2})5d$	$^2[5/2]^\circ$	3
(K0)	**810.40**	**153**	**500**	$4s^24p^5(^2P^\circ_{3/2})5p$	$^2[5/2]$	**3**	$4s^24p^5(^2P^\circ_{3/2})5d$	$^2[7/2]^\circ$	**4**
(K1)	**810.44**	**112**	**4000**	$\boldsymbol{4s^24p^5(^2P^\circ_{3/2})5s}$	$^2[3/2]^\circ$	**2**	$\boldsymbol{4s^24p^5(^2P^\circ_{3/2})5p}$	$\boldsymbol{^2[5/2]}$	**2**
(K1,1)	1317.74	204	310	$4s^24p^5(^2P^\circ_{3/2})5p$	$^2[5/2]$	2	$4s^24p^5(^2P^\circ_{3/2})6s$	$^2[3/2]^\circ$	1
(K1,2)	1362.24	201	130	$4s^24p^5(^2P^\circ_{3/2})5p$	$^2[5/2]$	2	$4s^24p^5(^2P^\circ_{3/2})4d$	$^2[3/2]^\circ$	1
(K1,3)	1689.05	130	340	$4s^24p^5(^2P^\circ_{3/2})5p$	$^2[5/2]$	2	$4s^24p^5(^2P^\circ_{3/2})4d$	$^2[7/2]^\circ$	3
(K2)	**811.29**	**27.70**	**500**	$\boldsymbol{4s^24p^5(^2P^\circ_{3/2})5s}$	$^2[3/2]^\circ$	**2**	$\boldsymbol{4s^24p^5(^2P^\circ_{3/2})5p}$	$\boldsymbol{^2[5/2]}$	**3**
(K2,1)	645.63	150	200	$4s^24p^5(^2P^\circ_{3/2})5p$	$^2[5/2]$	3	$4s^24p^5(^2P^\circ_{3/2})6d$	$^2[7/2]^\circ$	4
(K2,2)	810.40	153	500	$4s^24p^5(^2P^\circ_{3/2})5p$	$^2[5/2]$	3	$4s^24p^5(^2P^\circ_{3/2})5d$	$^2[7/2]^\circ$	4
(K2,3)	1363.42	97.1	250	$4s^24p^5(^2P^\circ_{3/2})5p$	$^2[5/2]$	3	$4s^24p^5(^2P^\circ_{3/2})6s$	$^2[3/2]^\circ$	2
(K3)	**819.01**	**112**	**300**	$\boldsymbol{4s^24p^5(^2P^\circ_{3/2})5s}$	$^2[3/2]^\circ$	**1**	$\boldsymbol{4s^24p^5(^2P^\circ_{3/2})5p}$	$\boldsymbol{^2[3/2]}$	**2**
(K3,1)	985.62	251	500	$4s^24p^5(^2P^\circ_{3/2})5p$	$^2[3/2]$	2	$4s^24p^5(^2P^\circ_{1/2})4d$	$^2[3/2]^\circ$	2
(K3,2)	1537.20	680	725	$4s^24p^5(^2P^\circ_{3/2})5p$	$^2[3/2]$	2	$4s^24p^5(^2P^\circ_{3/2})6s$	$^2[3/2]^\circ$	2
(K3,3)	1678.51	148	320	$4s^24p^5(^2P^\circ_{3/2})5p$	$^2[3/2]$	2	$4s^24p^5(^2P^\circ_{3/2})4d$	$^2[5/2]^\circ$	3
(K4)	**826.32**	**29.27**	**400**	$\boldsymbol{4s^24p^5(^2P^\circ_{1/2})5s}$	$^2[1/2]^\circ$	**1**	$\boldsymbol{4s^24p^5(^2P^\circ_{1/2})5p}$	$\boldsymbol{^2[3/2]}$	**2**
(K4,1)	1006.60	3770	10	$4s^24p^5(^2P^\circ_{1/2})5p$	$^2[3/2]$	2	$4s^24p^5(^2P^\circ_{3/2})6d$	$^2[7/2]^\circ$	3
(K4,2)	1388.29	94.3	27	$4s^24p^5(^2P^\circ_{1/2})5p$	$^2[3/2]$	2	$4s^24p^5(^2P^\circ_{1/2})6s$	$^2[1/2]^\circ$	1
(K5)	**828.11**	**70.52**	**200**	$\boldsymbol{4s^24p^5(^2P^\circ_{1/2})5s}$	$\boldsymbol{^2[1/2]^\circ}$	**1**	$\boldsymbol{4s^24p^5(^2P^\circ_{1/2})5p}$	$\boldsymbol{^2[1/2]}$	**1**
(K5,1)	1012.10	1600	30	$4s^24p^5(^2P^\circ_{1/2})5p$	$^2[1/2]$	1	$4s^24p^5(^2P^\circ_{3/2})6d$	$^2[3/2]^\circ$	2
(K5,2)	1383.29	321	8	$4s^24p^5(^2P^\circ_{1/2})5p$	$^2[1/2]$	1	$4s^24p^5(^2P^\circ_{1/2})6s$	$^2[1/2]^\circ$	1
(K5,3)	1393.90	90.9	10	$4s^24p^5(^2P^\circ_{1/2})5p$	$^2[1/2]$	1	$4s^24p^5(^2P^\circ_{1/2})6s$	$^2[1/2]^\circ$	0
(K6)	**829.81**	**34.12**	**500**	$\boldsymbol{4s^24p^5(^2P^\circ_{3/2})5s}$	$\boldsymbol{^2[3/2]^\circ}$	**1**	$\boldsymbol{4s^24p^5(^2P^\circ_{3/2})5p}$	$\boldsymbol{^2[3/2]}$	**1**
(K6,1)	1442.68	108	350	$4s^24p^5(^2P^\circ_{3/2})5p$	$^2[3/2]$	1	$4s^24p^5(^2P^\circ_{3/2})6s$	$^2[3/2]^\circ$	1
(K6,2)	1496.19	1110	290	$4s^24p^5(^2P^\circ_{3/2})5p$	$^2[3/2]$	1	$4s^24p^5(^2P^\circ_{3/2})4d$	$^2[3/2]^\circ$	1
(K6,3)	1693.58	173	280	$4s^24p^5(^2P^\circ_{3/2})5p$	$^2[3/2]$	1	$4s^24p^5(^2P^\circ_{3/2})4d$	$^2[5/2]^\circ$	2

performed a PCA[30] of all recorded spectra at up to several hundreds of operational points. The PCA technique reduces the dimensions of a dataset with a large number of measured variables. This simplifies the process of correlating the spectral information and the corresponding plasma parameters significantly. PCA is not the only technique capable of dimension reduction. Other methods include linear discriminant analysis,[74] non-negative matrix factorization,[75] and factor analysis.[76] However, we only focus on the PCA here.

For establishing an empirical correlation between OES and plasma parameters, a reference dataset is measured, consisting of a total of m spectra. Each spectrum consists of n data points or n wavelength positions and their respective spectral intensities. In other words, a spectrum is a point in an n-dimensional coordinate space, in which the n wavelength positions define the coordinate axes and the respective intensities are the coordinates on these axes. By performing a PCA, the n-dimensional coordinate space that contains the spectra is, for example, reduced into a two-dimensional coordinate space, in which the individual data points still are well separated. This two-dimensional coordinate space is spanned by two new axes, which typically contain the highest and second highest variance of the dataset.

The process of determining the PCA axes is described in the following. The covariances σ_{ij} of each of the n wavelength positions with every other wavelength position (including itself) are calculated using

$$\sigma_{ij} = \frac{1}{m} \times \sum_{k=0}^{m} (x_{ki} - \overline{x_i}) \times (x_{kj} - \overline{x_j}), \tag{1}$$

where x_{ki} and x_{kj} are the intensities of spectrum k at the two wavelength positions i and j. The variables $\overline{x_i}$ and $\overline{x_j}$ are the average intensities at the wavelength positions i and j of the average spectrum of all spectra of the recorded set.

With the covariances calculated, the covariance matrix $\mathbf{C}$ is set up as

$$\mathbf{C} = \begin{pmatrix} \sigma_{00} & \sigma_{01} & \cdots & \sigma_{0n} \\ \sigma_{10} & \sigma_{11} & \cdots & \sigma_{1n} \\ \vdots & \vdots & \ddots & \vdots \\ \sigma_{n0} & \sigma_{n1} & \cdots & \sigma_{nn} \end{pmatrix}. \tag{2}$$

The eigenvalues of $\mathbf{C}$ correspond to the data variances on the principal component axes $PC_{\mathrm{E},i}(\lambda)$, which are the eigenvectors of $\mathbf{C}$ and are spectrum-like with n components.

The coordinates (or scores) of a spectrum $S(\lambda)$ in this new coordinate system of $PC_{\mathrm{E},i}(\lambda)$ are calculated as follows:

$$PC_i = \sum_{\lambda} (S(\lambda) - \overline{S_{\mathrm{PCA}}}(\lambda)) \times PC_{\mathrm{E},i}(\lambda), \tag{3}$$

where $\overline{S_{\mathrm{PCA}}}$ is the average spectrum of the reference dataset. The spectrum $S(\lambda)$ can now be written as a series expansion,

$$S(\lambda) = \overline{S_{\mathrm{PCA}}}(\lambda) + \sum_{i} PC_i \times PC_{\mathrm{E},i}(\lambda). \tag{4}$$

The fraction in percent of the total variance on each axis shows how much of the variation in the data is represented by the scores of this principal component. Often, the sum the variances on PC_1 and PC_2 is already close to 100% of the total variance so that the data can be sufficiently separated in just two dimensions.

B. Evaluation of the Langmuir probe measurements

The Langmuir probe measurements were evaluated using a modified version of the standard procedure.[19,20,68,69] This modified approach is more robust against deviations from the theoretical ideal. It was developed in the course of our previously reported experiments[29] on the basis of the standard procedure.[19,20,68,69] The process is shown in Fig. 3, where the first step is the determination of the ion saturation current I_{sat}. I_{sat} is the intercept of a linear fit $[f(U) = a \times U + I_{\mathrm{sat}}]$ in the saturation regions shown as red dashed lines in Fig. 3. To correct for the saturation, the slope a is subtracted from the U–I-characteristics $[I_{\mathrm{corrected}}(U) = I(U) - a \times U]$, and the dashed blue curve in Fig. 3 is obtained. The corrected curve $I_{\mathrm{corrected}}(U)$ is normalized by dividing by I_{sat} (not shown in Fig. 3 for simplicity). The maximum slope $s_{\max}$ of the normalized, corrected curve is proportional to the inverse electron temperature T_{e}. $s_{\max}$ is obtained by a polynomial fit of third order $[f(x) = \sum_{i=0}^{3} a_i \times x^i]$ in the region $-\Delta U$ to $+\Delta U$; therefore, $s_{\max} = -\frac{1}{3} a_2^2/a_3 + a_1$. The electron temperature in Kelvin is calculated according to

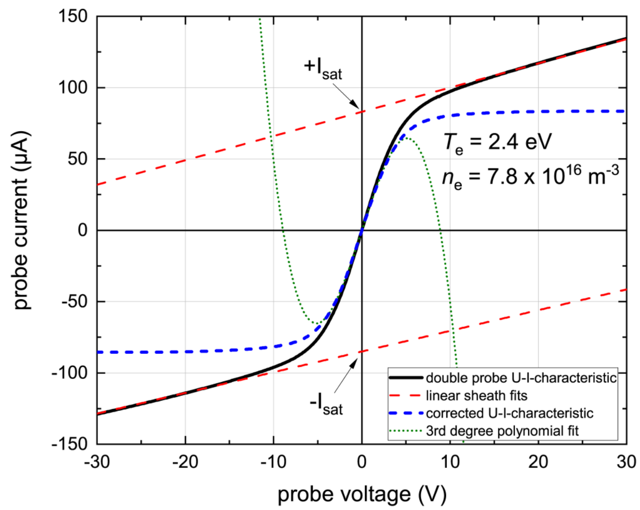

FIG. 3. Langmuir double probe evaluation process illustrated for measurement data of a pure xenon plasma. The linear parts of the measured curve (black line) are fitted to obtain the ion saturation current I_{sat} (red dashed lines). The probe voltage U is the potential difference between the two probe wires. The curve is corrected (dashed blue line), and the maximum slope is determined by fitting a third order polynomial (dotted green line) in the vicinity of $U = 0$ V. The plasma parameters T_{e} and n_{e} are calculated using Eqs. (5) and (6).

$$T_{\mathrm{e}} = \frac{e}{2k_{\mathrm{B}} \times s_{\max}}. \tag{5}$$

To calculate the electron density n_{e}, the previously determined values I_{sat} and T_{e}, as well as the probe area A_{p}, and the ion mass m_{ion} are needed,

$$n_{\mathrm{e}} = \frac{I_{\mathrm{sat}}}{A_{\mathrm{p}} e} \sqrt{\frac{m_{\mathrm{ion}}}{k_{\mathrm{B}} T_{\mathrm{e}}}}. \tag{6}$$

An additional approximation is necessary when the electron density n_{e} has to be calculated for mixed gas plasmas using Eq. (6). The ion mass m_{ion} is not easily determined, as the mixture consists of the two main ion species Xe^{+} and Kr^{+}, which both contribute to the measured Langmuir U–I-characteristics. We, therefore, use an approximated effective ion mass $m_{\mathrm{ion,eff}}$ for the calculation of n_{e}. Since the gas flow Q in sccm represents the number of particles inserted into the discharge chamber, we can calculate the weighted average atomic mass $m_{\mathrm{atom,eff}}$ as

$$m_{\mathrm{atom,eff}} = m_{\mathrm{Xe}} \times \frac{Q_{\mathrm{Xe}}}{Q_{\mathrm{Xe}} + Q_{\mathrm{Kr}}} + m_{\mathrm{Kr}} \times \frac{Q_{\mathrm{Kr}}}{Q_{\mathrm{Xe}} + Q_{\mathrm{Kr}}}, \tag{7}$$

assuming equal residence times of the two atomic species inside the discharge chamber. While the exact gas flow does not matter for the evaluation of Langmuir measurements on a pure gas plasma, mixed gas plasmas require calibrated MFCs to avoid errors when employing Eq. (7). If we further assume the ionization degree for xenon and krypton to be identical, effective atomic mass and effective ion mass will be equal ($m_{\mathrm{atom,eff}} = m_{\mathrm{ion,eff}}$). However, in reality, krypton will have a shorter residence time due to its smaller mass and, therefore, a higher thermal velocity. Furthermore, the higher ionization energy of krypton will result in a lower ionization degree than for xenon. Both effects will push the real effective ion mass further toward that of xenon. Therefore, the real n_e will be probably somewhat higher than estimated. However, our assumptions should be sufficient to demonstrate the basic principle of our approach without going deeper into ionization processes and particle motion.

The definition of a temperature assumes a Maxwellian electron energy distribution function (EEDF).[19,20,68] In an rf plasma, the fast electrons in the Maxwell tail are suppressed; therefore, the EEDF can deviate from the Maxwellian ideal.[37,77] This also changes the optical spectrum, as excitation rates change. Our empirical approach builds a correlation on a set of experimental data of a real plasma. Thus, as long as another real plasma analyzed on the basis of our reference data is comparable to the one used for acquiring the reference data (which shall be the case, if the optical emission spectra are comparable), the specific EEDF is not too relevant for the outcome of the analysis. We assume that a spectrum will be comparable to the reference spectra, if the plasma under study is driven under comparable experimental conditions (i.e., rf frequency and power, neutral gas densities of the propellant mixture) and if all relative line intensities are within the range of the mapped line intensities. If the PCA scores then fall inside the reference PCA, the correlation will be applicable. However, it should be noted that the validity of the application to a plasma in a setup other than the reference setup is not investigated here. It is yet unclear whether differences in the setup may affect the applicability.

III. RESULTS AND DISCUSSION

During the acquisition of a series of hundreds of spectra, small vibrations or thermal expansion of the measurement equipment might cause small wavelength shifts of the optical transitions of some tens of picometers. Here, the spectra shifted by approximately 1 pixel or 28 pm over the full measurement series. While they are not relevant for the evaluation, the PCA may be sensitive to such shifts. To circumvent the issue, the spectral information is simplified by integrating the line intensities of the, e.g., six xenon lines shown in Fig. 2. For example, the line intensity of X2 at 823.16 nm is determined by adding up all measured intensities between 821.99 and 824.11 nm. The PCA is then performed with these line intensities as input. The obtained principal components $PC_{\mathrm{E},i}$ ($i = 1, \ldots, 6$ for xenon) are the new coordinate axes with maximum data spread, where $PC_{\mathrm{E},1}$ covers the highest variance, followed by $PC_{\mathrm{E},2}$, etc.

First, we conducted measurements on a pure xenon plasma at various gas flows and input powers. $PC_{\mathrm{E},1}$ and $PC_{\mathrm{E},2}$ cover the majority of the data variance. However, due to a wide range of rf power, the first two principal components are not fully sufficient to separate the spectra in the corresponding 2D representation for all operational points of the plasma, with each spectrum corresponding to another set of plasma parameters. To fully separate the spectra, the third axis $PC_{\mathrm{E},3}$ also has to be considered. For this purpose, we define a new axis direction in the PC_1/PC_2 plane as a linear combination of PC_1 and PC_2 defined by the vector $\vec{v}$,

$$x_v = \begin{pmatrix} v_1 \\ v_2 \end{pmatrix} \cdot \begin{pmatrix} PC_1 \\ PC_2 \end{pmatrix} = v_1 \times PC_1 + v_2 \times PC_2. \tag{8}$$

Choosing $v_1 = -1/3$ and $v_2 = 1$ in this case yields a satisfactory separation of the data points (each corresponding to a spectrum of a specific operational point of the plasma) when plotting the corresponding scores in a projected 2D representation PC_3 vs $(-1/3PC_1 + PC_2)$ as shown in Fig. 4(a). The scores in Fig. 4(a) reveal a regular pattern with clear trends as functions of the external input parameters, i.e., the rf power coupled into the plasma and the propellant gas flow defining the neutral gas density of the plasma. A variation of the gas density for a given power yields almost straight lines in the 2D plane, whereas the variation of the rf power at a fixed density leads to curves as indicated in the figure.

The corresponding plasma parameters shown in Fig. 4(b) measured simultaneously with the spectra exhibit the anticipated trends.[15,78,79] Lowering the xenon gas flow increases the electron temperature. The electron density increases with higher input power. The maximum electron density reached for lower gas flow decreases, as the input power limitation is reached earlier. An interesting pattern occurs at low input powers, where the mapping was done in small power steps. Here, the electron temperature rises with increasing electron density and falls off again exhibiting a sharp maximum at around $5 \times 10^{16}\,\mathrm{m}^{-3}$. Currently, we seek a satisfactory explanation for this behavior.

Having established a 2D representation in a 2D plane of the coordinate space in Fig. 4(a), which virtually separates the data points representing all spectra taken at different operational conditions and having shown in Fig. 4(b) that the plasma parameters T_e and n_e show the anticipated trends, we can now parameterize the dependence of T_e and n_e on the coordinates given by the chosen new axes. To describe the plasma parameters in Fig. 4(b) as a function of the scores shown in Fig. 4(a), we introduce the fitting function,

$$f(x_v, PC_3) = \sum_{i=0}^{n} \sum_{j=0}^{i+j\leq n} a_{i,j} \times x_v^i \times PC_3^j. \tag{9}$$

Here, x_v is the modified score value according to Eq. (8) and n is the polynomial order of the fit. Using the fitting function in Eq. (9) with a polynomial order of $n = 4$, the R^2-values for the T_e and n_e fits are 0.954 and 0.990, respectively. Since the function in Eq. (9)

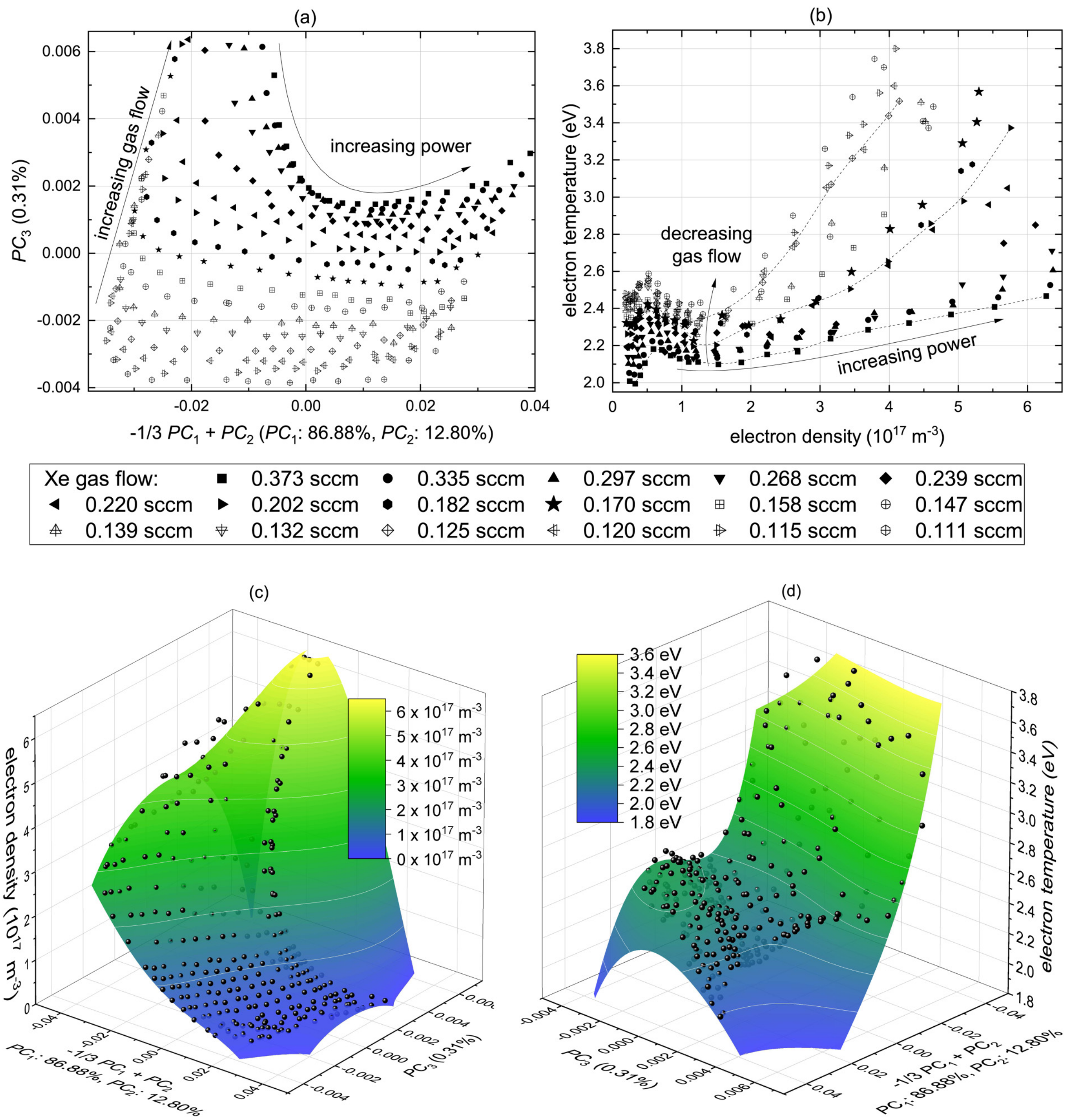

FIG. 4. PCA scores of a series of xenon spectra taken at various gas flows (a). The three-dimensional scores are displayed in two dimensions with the *x* axis being a vector on the PC_1–PC_2 plane to better visualize the spread in the OES data. The corresponding plasma parameters measured with the Langmuir double probe of the same series are shown in (b). The fits of the electron density (c) and the temperature (d) over the modified PCA scores are the correlation between OES and plasma parameters for pure xenon.

is three-dimensional, the fits can be displayed and are shown in Figs. 4(c) and 4(d). The two 3D plots clearly demonstrate that the PCA can indeed establish correlations between plasma parameters and the optical emission spectra. Of course, such a parameterization is best in the center of the set of data points and deviates toward the edges of the fitted 2D surface. In this measured dataset, we find the deviation between measured and calculated plasma parameters to be about ±5% for T_e and ±20% for n_e

when the edges of the contour fitting are avoided. For the anticipated application, i.e., the non-invasive determination of the plasma parameters inside an ion thruster, it will be of major importance that the operational points of its plasma lie well inside the parameter space of operational points of the reference plasma. However, if this is given, the plasma parameters can be determined non-invasively with a high degree of accuracy.

Using the same approach, we can also analyze the OES data for krypton plasmas. The data points corresponding to the optical emission spectra recorded at different operational points of the plasma can be separated quite well when plotting their PC scores in the plane spanned by PC_2 and PC_3 as shown in Fig. 5(a). However, there is no angle at which the first three principal component scores can be projected to a 2D representation without major overlapping of data points.

Nevertheless, the plot of the electron density n_e vs electron temperature T_e in Fig. 5(b) shows again clear trends as a function of rf power and gas flow. The electron temperatures reach higher levels than for xenon, while the electron densities are somewhat smaller. Due to the higher ionization energy of krypton, more energy is needed for heating of the electrons before ionization is possible. Therefore, a hotter, less dense plasma is expected.

Contrary to the xenon case, the two plasma parameters cannot be fitted to a fitting curve according to Eq. (9), as the overlapping shown in Fig. 5(a) prevents a direct surjective correspondence. One possibility to set up a parametric correlation is employing a higher dimensional fit, thus yielding $T_e(PC_1, PC_2, PC_3)$ and $n_e(PC_1, PC_2, PC_3)$. However, such a fit cannot be presented in a 3D plot. Therefore, we use an alternative approach. As the data cloud forms a 3D surface, another option is to find a parametric description of that surface with two variables u and v and to establish correlations $T_e(u, v)$ and $n_e(u, v)$. For this purpose, we created a mesh from the PCA results as shown in Fig. 5(a). We then assigned u and v values to the individual measurements according to their position on that mesh so that u increases with decreasing input power, while v increases with decreasing mass flow. The PCA scores can then be fitted as a function of the u–v coordinates as shown in Fig. 5(c). The corresponding plasma parameters shown in Fig. 5(b) can also be fitted as functions of the u–v coordinates as shown in Figs. 5(d) and 5(e). All fits were performed using fitting functions of the type,

$$f(u, v) = \sum_{i=0}^{n} \sum_{j=0}^{i+j \leq n} a_{i,j} \times u^i \times v^j, \tag{10}$$

with $n = 3$. The R^2 values were 0.978 for $PC_1(u, v)$, 0.986 for $PC_2(u, v)$, 0.991 for $PC_3(u, v)$, 0.918 for $T_e(u, v)$, and 0.997 for $n_e(u, v)$.

A new spectrum measured at an operational point where the plasma parameters shall be determined can now be transferred in the PCA coordinate space using Eq. (3). To obtain the plasma parameters for this operational point, the u–v coordinates have to be determined. By looking at the position of the corresponding PCA-point on the mesh shown in Fig. 5(a), u–v coordinates can be estimated. The u–v values can now be refined using the previously found functions $PC_i(u, v)$ and minimizing the sum of the relative quadratic deviations of the measured scores PC_i of the spectrum and the calculated scores $PC_i(u, v)$ using

$$\sum_{i=1}^{3} \left(\frac{PC_i - PC_i(u, v)}{PC_i} \right)^2 \rightarrow \text{min}. \tag{11}$$

The refined u–v values can then be used to obtain T_e and n_e using the previously found functions $T_e(u, v)$ and $n_e(u, v)$. This method is, however, somewhat reliant on the quality of the parameterization $PC_i(u, v)$ and a good first estimation of u and v. Especially toward the edges of the fitting regions, this method becomes less reliable. In our measured dataset, if good first estimations are used and the edges are avoided, we find the deviation between measured and calculated plasma parameters to be about $\pm 10\%$ for T_e and $\pm 25\%$ for n_e.

After having demonstrated that our approach is suitable for plasmas of pure xenon and krypton propellants, we will now turn to its use for analyzing plasmas of gas mixtures of xenon and krypton. The spectra of the xenon/krypton plasma shown in Fig. 2 indicate one of the challenges typical in analyzing OES data of mixed plasma. In the spectral window selected by us, the spectral lines of xenon and krypton, X3 and K4, and X4 and K5 overlap. We have handled this situation by considering these lines as one line in the simplification procedure prior to the PCA. Furthermore, we have performed multiple series of combined OES and Langmuir measurements where we have kept the krypton gas flow constant and varied the xenon gas flow. In other words, the mixing ratio is not constant throughout a series. We have acquired datasets for the four constant krypton gas flows 0.354, 0.218, 0.147, and 0.108 sccm. In what follows, we will exemplarily discuss the data set where the krypton gas flow was set to 0.218 sccm and the xenon gas flow was varied between about 0.1 and 0.4 sccm.

As for the pure propellants, the PCA results of the mixture allow one to separate all the data points corresponding to optical emission spectra taken at different operational conditions as shown in Fig. 6(a). Thus, the projection method could be employed similar to the pure xenon case. The projection plane was spanned by PC_2 and the linear combination of $-0.05PC_1 + PC_3$. Again, clear trends in the 2D plot can be observed as a function of increasing xenon flow as well as in dependence on rf power as indicated in Fig. 6(a).

The same holds for the plot of electron temperature T_e vs electron density n_e in Fig. 6(b). Characteristic curves are obtained as a function of added xenon gas flow and as a function of rf power. These resemble those obtained for the pure propellants.

As expected, the electron temperature rises with decreasing gas flow. However, the differences in the electron temperature for different xenon gas flows shown in Fig. 6(b) become smaller with decreasing xenon gas flows. The rise in the electron temperature is a result of lower neutral gas density, where the electrons acquire more energy per rf half cycle, as they have a lower probability to collide with atoms and ions. In this case, only the xenon gas flow of the gas mixture is lowered; therefore, only the neutral xenon density is reduced. Since the krypton gas flow remains constant, the overall neutral gas density approaches a constant value greater than zero. Decreasing the xenon gas flow from, e.g., 0.120 to 0.111 sccm, has less effect on the plasma parameters than in pure

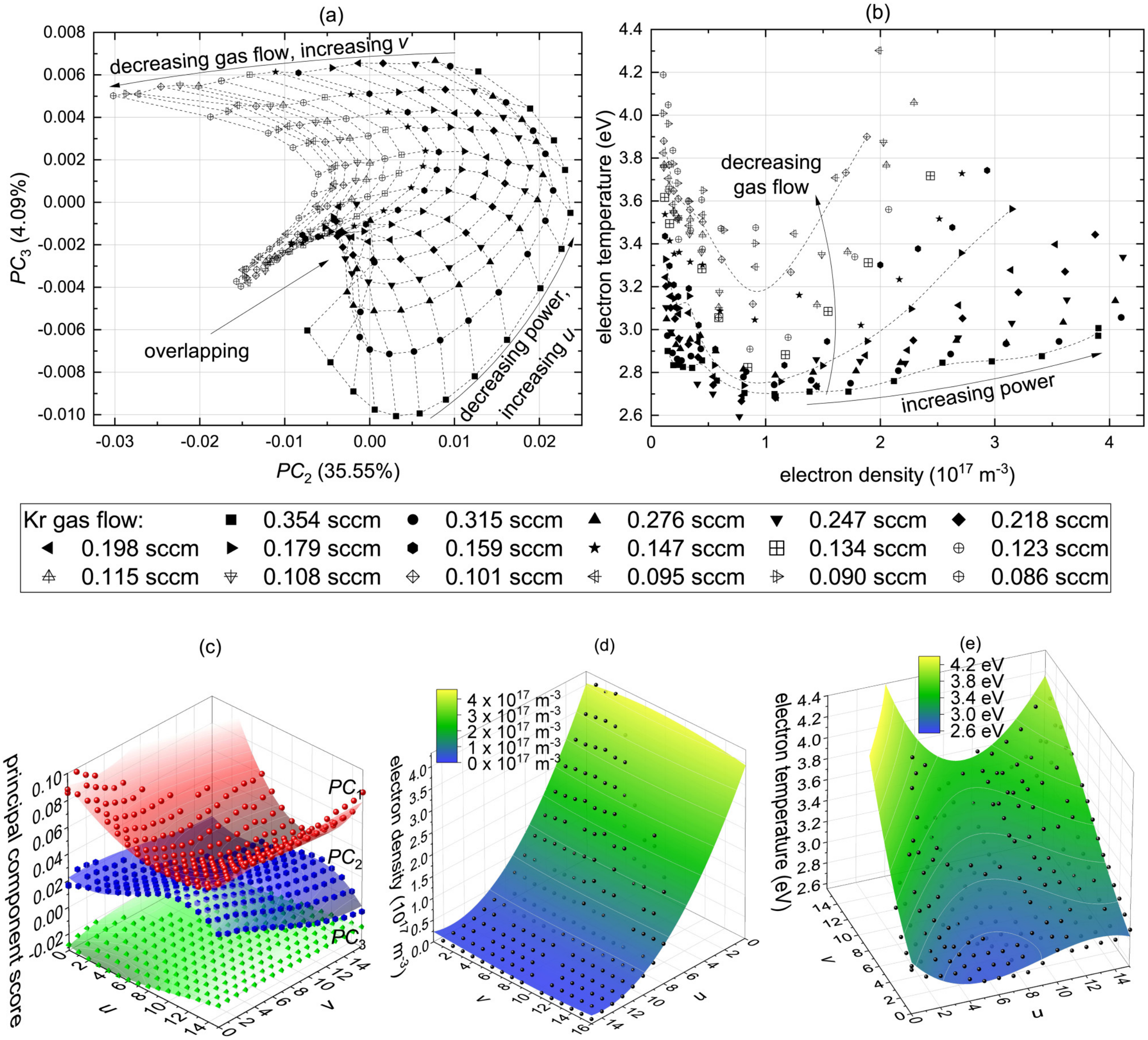

FIG. 5. PCA scores for a series of krypton spectra taken at various gas flows (a). The data spread can be seen best when observing the three-dimensional scores in the PC_2–PC_3 plane. The corresponding plasma parameters measured with the Langmuir double probe for this series are shown in (b). A fit for each principal component as a function of new coordinates u and v is shown in (c). The data points of PC_1 and PC_2 in (c) are shifted upward for a better visual representation. The values for the new variables u and v are assigned to the data points in the PCA coordinate space according to their position on the mesh shown in (a). The plasma parameters can also be fitted as functions of the u–v coordinates, as shown for electron density (d) and temperature (e). This yields a correlation between optical emission spectra and plasma parameters with one additional step to perform compared to the projection method used for xenon in Fig. 4.

xenon as the krypton atoms present as a background serve as collision partners for the electrons. Vice versa, a small portion of xenon in the plasma still provides enough easily ionizable atoms to keep the electron temperature below the ones shown in Fig. 5(b) for pure krypton.

These findings allow us to plot surfaces of the plasma parameters in dependence of the PCA based coordinates selected for achieving the separation into two dimensions in Fig. 6(a). The two surface fits of electron density n_e and electron temperature T_e are shown in Figs. 6(c) and 6(d), respectively. Here, Eq. (9) was applied with a polynomial order of $n = 4$, yielding an R^2 of 0.980 for n_e and 0.978 for T_e. In this mixed gas dataset, we find the deviation between measured and calculated plasma parameters to be about $\pm 5\%$ for T_e and $\pm 25\%$ for n_e when the edges of the contour

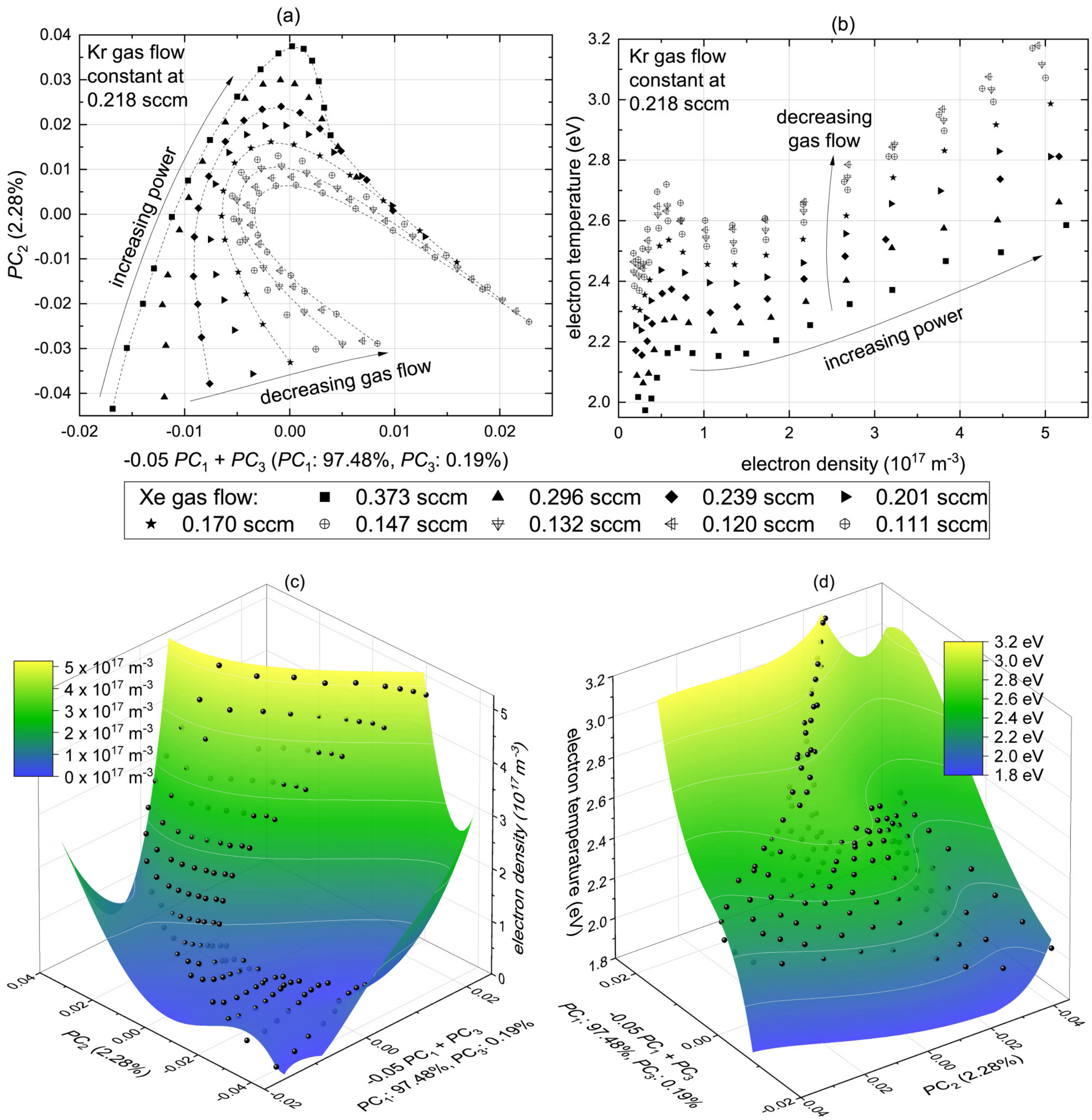

FIG. 6. PCA scores of the xenon/krypton mixed gas OES measurements for a constant krypton gas flow of 0.218 sccm and variable xenon gas flow (a). Like in Fig. 4(a), the three-dimensional scores are displayed in two dimensions with the *x* axis being a vector on the PC_1–PC_3 plane to better visualize the spread in the OES data. The corresponding plasma parameters from the Langmuir double probe measurements are shown in (b). The fits of the electron density (c) and temperature (d) over the modified PCA scores are the correlation between OES and plasma parameters for the mixed gas plasma with a constant krypton gas flow of 0.218 sccm.

fitting are avoided. Similar results have been obtained for the other xenon/krypton gas mixture series based on constant krypton gas flows of 0.354, 0.147, and 0.108 sccm, which are provided in the data availability statement. The results strongly suggest that a similar analysis and the establishment of a surjective mapping of the PC scores of spectra onto the corresponding plasma parameters are also possible for datasets taken of xenon/krypton gas mixtures with constant fractions of xenon and krypton.

The situation is different when simultaneously performing a PCA of the full dataset, i.e., of all spectra taken at different xenon and krypton gas flows and rf powers. In this case, we cannot find a 2D plane in the coordinate space of the spectra where the data points representing the spectra are clearly separated. This means that at least a third principal component based coordinate axis is required to achieve a full separation of the data points representing the spectra. However, this is somewhat anticipated as three external control parameters, xenon gas flow, krypton gas flows, and rf power, are variable in this situation. However, it should still be possible to establish a corresponding surjective mapping between PC scores and plasma parameters, but it will be of higher dimensionality than two-dimensional.

IV. CONCLUSION

We have developed an empirical approach for correlating optical emission spectra of gas plasmas obtained at different operational points with the corresponding plasma parameters. For this purpose, we measured the optical emission spectra of xenon, krypton, and xenon/krypton mixed plasmas at different operational points and simultaneously performed Langmuir probe measurements. The different operational points were defined by tuning two external parameters, the propellant gas flow (in the case of the gas mixtures, the gas flow of one constituent, while keeping that of the other constant), as well as the power coupled into the plasma for each set of combined optical emission and Langmuir measurements. The Langmuir measurements at each operation point were analyzed to extract electron temperature and electron density. For each set of optical emission spectra, a principal component analysis was conducted in order to present the differences in the set of spectra by a reduced number of characteristic coordinates based on the principal components. For all sets of spectra, it was possible to unambiguously characterize each spectrum of the set by two such characteristic coordinates only. This was demonstrated for xenon by using a projection method and for krypton by using a u–v mapping method. In a corresponding, two-dimensional plot in the plane spanned by these two coordinates, the data points representing the spectra can be well separated. This separation allows us to parameterize the plasma parameters as a function of the two coordinates, i.e., to establish a surjective mapping of the optical spectra onto the plasma parameters. In particular, the finding that this approach is successful for rather complex plasmas, such as those of gas mixtures, fortifies our view that the approach will also be applicable to various types of alternative propellants in future studies, for example, iodine, whose plasma is difficult to describe by microscopic theories. Having established such a reference set by simultaneously performing optical emission spectroscopy and Langmuir measurements, the next step is to employ the surjective mappings for a non-invasive determination of the plasma properties of unknown plasmas provided the same gas is used and the operational parameters lie within those of the reference set. Such plasmas may be those inside an ion source or ion thruster where an invasive probe, such as a Langmuir probe, may not be used as it may affect the plasma properties (e.g., in the case of very small discharge vessels) or where no suitable access for the probe is available (e.g., in electric thrusters that shall be qualified for space). Future studies may also examine the spatial distributions of the plasma parameters inside a RIT using this approach. The presented method of non-invasively determining the plasma parameters by optical spectroscopy will considerably contribute to a better understanding of ion thrusters and to speeding up their development and qualification for space.

ACKNOWLEDGMENTS

Benny Nauschütt is grateful for receiving a Ph.D. studentship in the framework of the JLU-Ariane Group Graduate School “Radio frequency ion thrusters.” This work was supported by ERDF within the Horizon 2020 program (Innovation Lab “Rough ambient physics”).

AUTHOR DECLARATIONS

Conflict of Interest

The authors have no conflicts to disclose.

DATA AVAILABILITY

The datasets used and/or analyzed during the current study are available from JLUdata under the link “http://dx.doi.org/10.22029/jlupub-234” for the xenon and mixed gas measurements and “http://dx.doi.org/10.22029/jlupub-300” for the krypton measurements.

REFERENCES

[1]S. Mazouffre, “Electric propulsion for satellites and spacecraft: Established technologies and novel approaches,” Plasma Sources Sci. Technol. **25**, 033002 (2016).
[2]K. Holste, P. Dietz, S. Scharmann, K. Keil, T. Henning, D. Zschätzsch, M. Reitemeyer, B. Nauschütt, F. Kiefer, F. Kunze, J. Zorn, C. Heiliger, N. Joshi, U. Probst, R. Thüringer, C. Volkmar, D. Packan, S. Peterschmitt, K. T. Brinkmann, H.-G. Zaunick, M. H. Thoma, M. Kretschmer, H. J. Leiter, S. Schippers, K. Hannemann, and P. J. Klar, “Ion thrusters for electric propulsion: Scientific issues developing a niche technology into a game changer,” Rev. Sci. Instrum. **91**, 061101 (2020).
[3]G. Karabadzhak, Y.-H. Chiu, S. Williams, and R. Dressler, *Hall Thruster Optical Emission Analysis Based on Single Collision* (American Institute of Aeronautics and Astronautics, 2001).
[4]J. Sommerville and L. King, “An optical diagnostic for xenon Hall thrusters including metastable contributions,” in *42nd AIAA/ASME/SAE/ASEE Joint Propulsion Conference and Exhibit* (American Institute of Aeronautics and Astronautics, 2006).
[5]R. Welle, *Availability Considerations in the Selection of Inert Propellants for Ion Engines* (American Institute of Aeronautics and Astronautics, 1990).
[6]R. Welle, *Xenon and Krypton Availability for Electric Propulsion—An Updated Assessment* (American Institute of Aeronautics and Astronautics, 1993).
[7]K. H. Groh, H. W. Loeb, and H. W. Velten, “Performance data comparison of the inert gas RIT 10,” J. Spacecrafts Rockets **21**, 360–365 (1984).
[8]H. Bassner and K. Groh, “A 50 mn RIT thruster assembly for application to heavy geostationary satellites,” in *31st Joint Propulsion Conference and Exhibit* (AIAA, 1995), p. 3068.
[9]V. Kim, G. A. Popov, V. Kozlov, A. Skrylnikov, and D. Grdlichko, “Investigation of SPT performance and particularities of its operation with Kr and Kr/Xe mixtures” in *International Electric Propulsion Conference, IEPC-01-065, Pasadena, CA* (ERPS, 2001).

[10]A. Bugrova, A. Morozov, A. Lipatov, A. Bishaev, V. Kharchevnikov, and M. Kozintseva, "Integral and spectral characteristics of ATON stationary plasma thruster operating on krypton and xenon," IEPC Paper **366**, 2003 (2003).
[11]J. A. Linnell and A. D. Gallimore, "Internal plasma potential measurements of a Hall thruster using xenon and krypton propellant," Phys. Plasmas **13**, 093502 (2006).
[12]J. A. Linnell and A. D. Gallimore, "Efficiency analysis of a Hall thruster operating with krypton and xenon," J. Prop. Power **22**, 1402–1418 (2006).
[13]H. Löb, "Ein elektrostatisches Raketentriebwerk mit Hochfrequenzionenquelle," Astronaut. Acta **8**, 49 (1962).
[14]H. Löb and J. Freisinger, *Ionenraketen* (Vieweg+Teubner Verlag, 1967).
[15]D. M. Goebel and I. Katz, *Fundamentals of Electric Propulsion*, 1st ed. (John Wiley & Sons, 2008).
[16]J. Beattie, R. Robson, and J. Williams, *Flight Qualification of an 18-mN Xenon Ion Thruster* (AIAA, 1993).
[17]V. Rawlin, J. Sovey, J. Anderson, and J. Polk, *NSTAR Flight Thruster Qualification Testing* (American Institute of Aeronautics and Astronautics, 1998).
[18]D. A. Herman, "Nasa's evolutionary xenon thruster (next) project qualification propellant throughput milestone: Performance, erosion, and thruster service life prediction after 450 kg," in *JANNAF 7th Modeling and Simulation, 5th Liquid Propulsion, and 4th Spacecraft Propulsion Joint Subcommittee Meeting* (NASA Technical Reports Server 2010), pp. 3–7.
[19]V. I. Demidov, S. V. Ratynskaia, and K. Rypdal, "Electric probes for plasmas: The link between theory and instrument," Rev. Sci. Instrum. **73**, 3409–3439 (2002).
[20]J. Benedikt, H. Kersten, and A. Piel, "Foundations of measurement of electrons, ions and species fluxes toward surfaces in low-temperature plasmas," Plasma Sources Sci. Technol. **30**, 033001 (2021).
[21]Y. Chiu, B. L. Austin, S. Williams, R. A. Dressler, and G. F. Karabadzhak, "Passive optical diagnostic of Xe-propelled Hall thrusters. I. Emission cross sections," J. Appl. Phys. **99**, 113304 (2006).
[22]G. F. Karabadzhak, Y. Chiu, and R. A. Dressler, "Passive optical diagnostic of Xe propelled Hall thrusters. II. Collisional-radiative model," J. Appl. Phys. **99**, 113305 (2006).
[23]T. S. Matlock, C. W. Larson, W. A. Hargus Jr, and M. R. Nakles, "An inversion method for reconstructing Hall thruster plume parameters from the line integrated measurements (postprint)," Technical Report, 2007.
[24]J. Yang, S. Yokota, R. Kaneko, and K. Komurasaki, "Diagnosing on plasma plume from xenon Hall thruster with collisional-radiative model," Phys. Plasmas **17**, 103504 (2010).
[25]L.-Q. Wei, W.-B. Li, Y.-J. Ding, X.-M. Zhu, Y.-F. Wang, J.-F. Hu, S.-L. Yan, and D.-R. Yu, "A photographic method for in-orbit measurement of electron temperature distribution in the plume of Hall thrusters," Plasma Sources Sci. Technol. **27**, 084002 (2018).
[26]Y. Wang, Y.-F. Wang, X.-M. Zhu, O. Zatsarinny, and K. Bartschat, "A xenon collisional-radiative model applicable to electric propulsion devices: I. Calculations of electron-impact cross sections for xenon ions by the Dirac B-spline R-matrix method," Plasma Sources Sci. Technol. **28**, 105004 (2019).
[27]X.-M. Zhu, Y.-F. Wang, Y. Wang, D.-R. Yu, O. Zatsarinny, K. Bartschat, T. V. Tsankov, and U. Czarnetzki, "A xenon collisional-radiative model applicable to electric propulsion devices: II. Kinetics of the 6s, 6p, and 5d states of atoms and ions in Hall thrusters," Plasma Sources Sci. Technol. **28**, 105005 (2019).
[28]M. R. Nakles and T. S. Matlock, "Hall thruster near-field plume characterization through optical emission spectroscopy" in *International Electric Propulsion Conference, IEPC-2019-246, Vienna, Austria* (ERPS, 2019).
[29]B. T. Nauschütt, L. Chen, K. Holste, and P. J. Klar, "Non-invasive assessment of plasma parameters inside an ion thruster combining optical emission spectroscopy and principal component analysis," EPJ Tech. Instrum. **8**, 13 (2021).
[30]H. Abdi and L. J. Williams, "Principal component analysis," Wiley Interdiscip. Rev. Comput. Stat. **2**, 433–459 (2010).
[31]J. Vlcek, "A collisional-radiative model applicable to argon discharges over a wide range of conditions. I. Formulation and basic data," J. Phys. D: Appl. Phys. **22**, 623–631 (1989).
[32]J. Vlcek and V. Pelikan, "A collisional-radiative model applicable to argon discharges over a wide range of conditions. II. Application to low-pressure, hollow-cathode arc and low-pressure glow discharges," J. Phys. D: Appl. Phys. **22**, 632–643 (1989).
[33]A. Bogaerts, R. Gijbels, and J. Vlcek, "Collisional-radiative model for an argon glow discharge," J. Appl. Phys. **84**, 121–136 (1998).
[34]A. Bogaerts, R. Gijbels, and J. Vlcek, "Modeling of glow discharge optical emission spectrometry: Calculation of the argon atomic optical emission spectrum," Spectrochim. Acta Part B **53**, 1517–1526 (1998).
[35]S. Iordanova and I. Koleva, "Optical emission spectroscopy diagnostics of inductively-driven plasmas in argon gas at low pressures," Spectrochim. Acta Part B **62**, 344–356 (2007).
[36]N. Tian-Ye, C. Jin-Xiang, L. Lei, L. Jin-Ying, W. Yan, W. Liang, and L. You, "A comparison among optical emission spectroscopic methods of determining electron temperature in low pressure argon plasmas," Chin. Phys. **16**, 2757–2763 (2007).
[37]G. P. Canal, H. Luna, R. M. O. Galvão, and R. Castell, "An approach to a non-LTE Saha equation based on the Druyvesteyn energy distribution function: A comparison between the electron temperature obtained from OES and the Langmuir probe analysis," J. Phys. D: Appl. Phys. **42**, 135202 (2009).
[38]J. B. Boffard, C. C. Lin, and C. A. DeJosephJr, "Application of excitation cross sections to optical plasma diagnostics," J. Phys. D: Appl. Phys. **37**, R143–R161 (2004).
[39]J. B. Boffard, R. O. Jung, C. C. Lin, L. E. Aneskavich, and A. E. Wendt, "Argon 420.1–419.8 nm emission line ratio for measuring plasma effective electron temperatures," J. Phys. D: Appl. Phys. **45**, 045201 (2012).
[40]J. B. Boffard, R. O. Jung, C. C. Lin, and A. E. Wendt, "Optical emission measurements of electron energy distributions in low-pressure argon inductively coupled plasmas," Plasma Sources Sci. Technol. **19**, 065001 (2010).
[41]X.-M. Zhu, W.-C. Chen, J. Li, and Y.-K. Pu, "Determining the electron temperature and the electron density by a simple collisional-radiative model of argon and xenon in low-pressure discharges," J. Phys. D: Appl. Phys. **42**, 025203 (2008).
[42]X.-M. Zhu and Y.-K. Pu, "Optical emission spectroscopy in low-temperature plasmas containing argon and nitrogen: Determination of the electron temperature and density by the line-ratio method," J. Phys. D: Appl. Phys. **43**, 403001 (2010).
[43]X.-M. Zhu, Y.-K. Pu, Y. Celik, S. Siepa, E. Schüngel, D. Luggenhölscher, and U. Czarnetzki, "Possibilities of determining non-Maxwellian EEDFs from the OES line-ratios in low-pressure capacitive and inductive plasmas containing argon and krypton," Plasma Sources Sci. Technol. **21**, 024003 (2012).
[44]S. Siepa, S. Danko, T. V. Tsankov, T. Mussenbrock, and U. Czarnetzki, "On the OES line-ratio technique in argon and argon-containing plasmas," J. Phys. D: Appl. Phys. **47**, 445201 (2014).
[45]R. A. Dressler, Y. Chiu, O. Zatsarinny, K. Bartschat, R. Srivastava, and L. Sharma, "Near-infrared collisional radiative model for Xe plasma electrostatic thrusters: The role of metastable atoms," J. Phys. D: Appl. Phys. **42**, 185203 (2009).
[46]X.-M. Zhu, W.-C. Chen, and Y.-K. Pu, "Gas temperature, electron density and electron temperature measurement in a microwave excited microplasma," J. Phys. D: Appl. Phys. **41**, 105212 (2008).
[47]Priti, R. K. Gangwar, and R. Srivastava, "Collisional-radiative model of xenon plasma with calculated electron-impact fine-structure excitation cross-sections," Plasma Sources Sci. Technol. **28**, 025003 (2019).
[48]V. M. Donnelly, "Plasma electron temperatures and electron energy distributions measured by trace rare gases optical emission spectroscopy," J. Phys. D: Appl. Phys. **37**, R217–R236 (2004).
[49]Y. Iida, S. Kado, and S. Tanaka, "On the application of He I collisional-radiative model to the He–H2 mixture plasmas in MAP-II divertor simulator," J. Nucl. Mater. **438**, S1237–S1240 (2013).
[50]Priti, R. K. Gangwar, and R. Srivastava, "Collisional radiative model for Ar-O_2 mixture plasma with fully relativistic fine structure cross sections," Phys. Plasmas **25**, 043517 (2018).

[51]N. Shukla, R. K. Gangwar, and R. Srivastava, "Diagnostic of Ar-CO_2 mixture plasma using a fine-structure resolved collisional radiative model," Spectrochim. Acta Part B **175**, 106019 (2021).
[52]F. Debal, J. Bretagne, M. Jumet, M. Wautelet, J. P. Dauchot, and M. Hecq, "Analysis of DC magnetron discharges in Ar-N_2 gas mixtures. comparison of a collisional-radiative model with optical emission spectroscopy," Plasma Sources Sci. Technol. **7**, 219–229 (1998).
[53]E. B. Saloman, "Energy levels and observed spectral lines of xenon, Xe I through Xe LIV," J. Phys. Chem. Ref. Data **33**, 765–921 (2004).
[54]O. Cheshnovsky, B. Raz, and J. Jortner, "Electronic energy transfer in rare gas mixtures," J. Chem. Phys. **59**, 3301–3307 (1973).
[55]J. D. Cook and P. Leichner, "Collisional and radiative excitation transfers in Kr-Xe mixtures: Quenching of Kr," Phys. Rev. A **31**, 90 (1985).
[56]J. D. Cook and P. Leichner, "Collisional and radiative excitation transfers in Kr-Xe mixtures: Emissions from the Xe (3 p 1) resonant level and the Xe first continuum region," Phys. Rev. A **43**, 1614 (1991).
[57]B. Krylov, G. Gerasimov, A. Morozov, A. Arnesen, R. Hallin, and F. Heijkenskjold, "Energy transfer studies in krypton-xenon mixtures excited in a cooled dc discharge," Eur. Phys. J. D **8**, 227–239 (2000).
[58]G. Zvereva and A. Loginov, "Excitation transfer in the plasma of a barrier discharge in a krypton-xenon mixture," Opt. Spectrosc. **90**, 502–507 (2001).
[59]E. J. McGuire, "Electron ionization cross sections in the born approximation," Phys. Rev. A **16**, 62 (1977).
[60]D. Margreiter, H. Deutsch, and T. Märk, "A semiclassical approach to the calculation of electron impact ionization cross-sections of atoms: From hydrogen to uranium," Int. J. Mass Spectrom. Ion Processes **139**, 127–139 (1994).
[61]D.-W. Chang and P. L. Altick, "Doubly, singly differential and total ionization cross sections of rare-gas atoms," J. Phys. B At. Mol. Opt. Phys. **29**, 2325 (1996).
[62]A. A. Sorokin, L. A. Shmaenok, S. V. Bobashev, B. Möbus, M. Richter, and G. Ulm, "Measurements of electron-impact ionization cross sections of argon, krypton, and xenon by comparison with photoionization," Phys. Rev. A **61**, 022723 (2000).
[63]R. O. Jung, J. B. Boffard, L. W. Anderson, and C. C. Lin, "Electron-impact excitation cross sections from the xenon $J = 2$ metastable level," Phys. Rev. A **72**, 022723 (2005).
[64]M. A. Stevenson, L. R. Hargreaves, B. Lohmann, I. Bray, D. V. Fursa, K. Bartschat, and A. Kheifets, "Fully differential cross-section measurements for electron-impact ionization of neon and xenon," Phys. Rev. A **79**, 012709 (2009).
[65]K. Holste, W. Gärtner, D. Zschätzsch, S. Scharmann, P. Köhler, P. Dietz, and P. J. Klar, "Performance of an iodine-fueled radio-frequency ion-thruster," Eur. Phys. J. D **72**, 9 (2018).
[66]P. Dietz, W. Gärtner, Q. Koch, P. E. Köhler, Y. Teng, P. R. Schreiner, K. Holste, and P. J. Klar, "Molecular propellants for ion thrusters," Plasma Sources Sci. Technol. **28**, 084001 (2019).
[67]H. Henke, *Elektromagnetische Felder : Theorie und Anwendung* (Springer Berlin Heidelberg, Berlin, 2015).
[68]E. O. Johnson and L. Malter, "A floating double probe method for measurements in gas discharges," Phys. Rev. **80**, 58–68 (1950).
[69]S. Bhattarai, "Interpretation of double langmuir probe I-V characteristics at different ionospheric plasma temperatures," Am. J. Eng. Appl. Sci. **10**, 882–889 (2017).
[70]A. Kramida and Y. Ralchenko, "NIST atomic spectra database, NIST standard reference database 78" (1999).
[71]J. Simon, U. Probst, and P. J. Klar, "Development of a radio-frequency generator for rf ion thrusters," in *34th International Electric Propulsion Conference, Hyogo-Kobe, Japan* (Aerospace Technology Japan, 2015).
[72]J. E. Junker, U. Probst, and P. J. Klar, "Development of a full bridge series resonant radio-frequency generator for optimized rit operation," in *36th International Electric Propulsion Conference, Vienna, Austria* (ERPS, 2019).
[73]E. B. Saloman, "Energy levels and observed spectral lines of krypton, Kr I through Kr XXXVI," J. Phys. Chem. Ref. Data **36**, 215–386 (2007).
[74]A. J. Izenman, "Linear discriminant analysis," in *Modern Multivariate Statistical Techniques*, Springer Texts in Statistics (Springer, New York, 2013), pp. 237–280.
[75]V. P. Pauca, J. Piper, and R. J. Plemmons, "Nonnegative matrix factorization for spectral data analysis," Linear Algebra Appl. **416**, 29–47 (2006).
[76]R. L. Gorsuch, *Factor Analysis* (Psychology Press, 2013).
[77]J. B. Boffard, R. O. Jung, C. C. Lin, L. E. Aneskavich, and A. E. Wendt, "Optical diagnostics for characterization of electron energy distributions: Argon inductively coupled plasmas," Plasma Sources Sci. Technol. **20**, 055006 (2011).
[78]A. Reeh, U. Probst, and P. J. Klar, "Global model of a radio-frequency ion thruster based on a holistic treatment of electron and ion density profiles," Eur. Phys. J. D **73**, 232 (2019).
[79]P. Dietz, A. Reeh, K. Keil, K. Holste, U. Probst, P. J. Klar, and C. Volkmar, "Global models for radio-frequency ion thrusters," EPJ Tech. Instrum. **8**, 10 (2021).

Plasma parameter measurement on a RIT-10 using empirical correlations between non-invasive optical emission spectroscopy and Langmuir diagnostics

IEPC-2022-253

Presented at the 37th International Electric Propulsion Conference
Massachusetts Institute of Technology, Cambridge, MA, USA
June 19-23, 2022

Benny Nauschütt[1] and Felix Becker[2] and Limei Chen[3] and Kristof Holste[4] and Peter J. Klar[5]
Justus Liebig University, Giessen, Hesse, 35392, Germany

Characterizing an electric propulsion device is crucial during testing and qualification. The optimization of existing diagnostic systems as well as the development of new ones is an important part in electric propulsion research. Here, we present an approach to determine plasma parameters non-invasively by first establishing a correlation between optical emission spectroscopy (OES) and Langmuir diagnostics and then applying this correlation to new OES measurements. This approach has no need for theoretical microscopic modeling of the plasma and its spectra which makes it very versatile since no knowledge of excitation cross sections or transition matrix elements is required. As the demand for electric propulsion is growing, this method may help to reduce qualification and testing times and enable continuous monitoring during use.

I. Introduction

For plasma-based electric propulsion systems xenon is commonly used as a propellant [1]. However, alternative propellants such as krypton, xenon/krypton gas mixtures or iodine are more and more considered as space electric propulsion systems turn into mass products [2–7]. Furthermore, commercialization makes the space market even more competitive, enforcing faster development cycles and lower costs for qualification. As all new thruster systems need to be tested, it is desirable to extract as much information as possible from every test and qualification step. Thus, non-invasive in-situ diagnostic methods need to be established not only for the ion plume, but also for the plasma inside the thruster. Invasive electrical probes are not desirable for characterizing a plasma inside the thruster during qualification, as they may severely affect the thruster's operation [8]. Furthermore, in case of a gridded ion thruster, like the radio-frequency ion thruster (RIT), the plasma is not easily accessible with electrical probes. This only leaves non-invasive diagnostic techniques, such as optical emission spectroscopy (OES) as appropriate means for characterizing the plasma.

To obtain plasma parameters from an OES measurement, a correlation between plasma parameters and measured spectra needs to be established. Usually, the OE spectra characteristic for specific plasma parameters are calculated based on microscopic plasma models (e.g. [9] or [10]). Such models require an exact knowledge of microscopic input parameters, such as the electronic states of the species forming the plasma, excitation cross-sections and transition matrix elements, which are not always readily available. We circumvent this challenge by employing an empirical approach which does not rely on such microscopic input parameters and can be used for all sorts of elemental plasmas as well for mixed gas plasmas [11, 12].

Prior to characterizing a RIT-10 thruster with active extraction, we measure a large reference data set of optical emission spectra and simultaneously conduct Langmuir measurements on the same RIT-10. The main differences in the

[1]PhD Student, Institute of Experimental Physics I, benny.nauschuett@physik.uni-giessen.de
[2]PhD Student, Institute of Experimental Physics I, felix.becker@exp1.physik.uni-giessen.de
[3]Senior Researcher, Institute of Experimental Physics I, limei.chen@exp1.physik.uni-giessen.de
[4]Senior Researcher, Institute of Experimental Physics I, kristof.holste@exp1.physik.uni-giessen.de
[5]Professor, Institute of Experimental Physics I, peter.j.klar@exp1.physik.uni-giessen.de

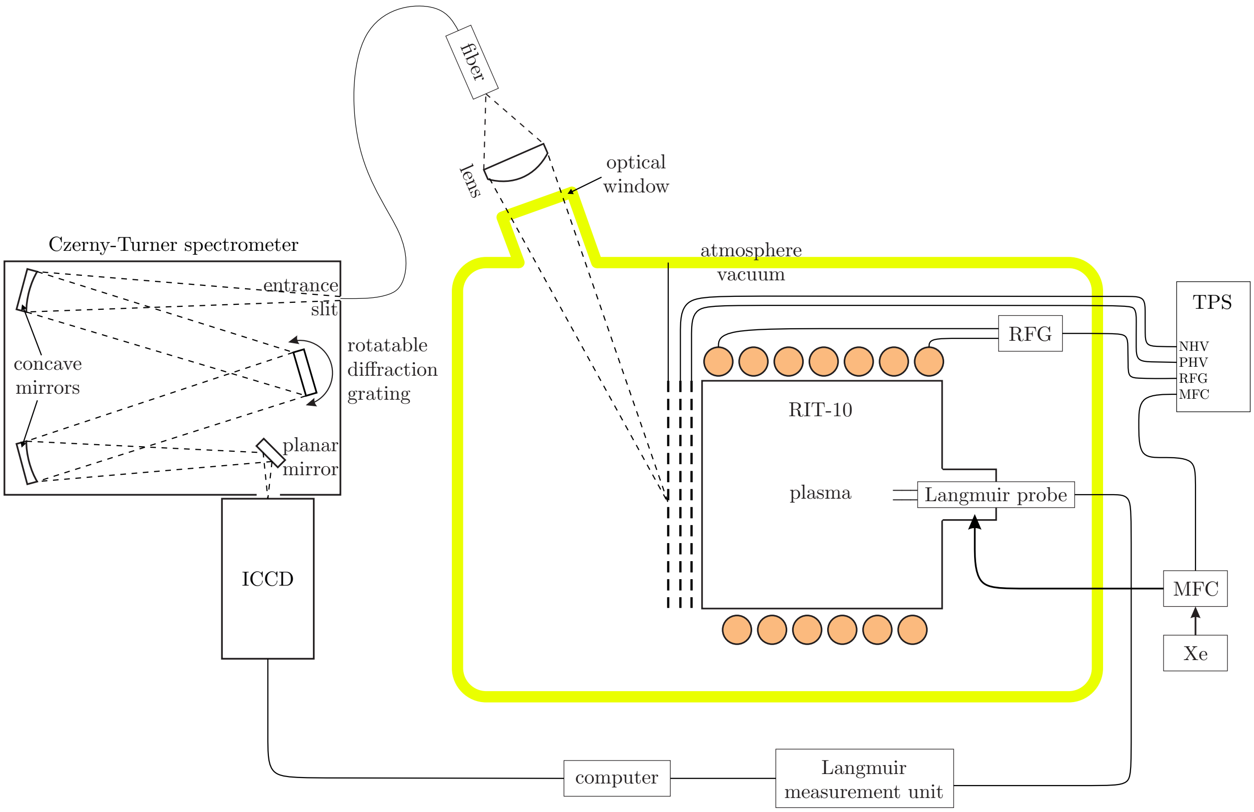

Fig. 1 Schematic image of the used experimental setup. A RIT-10 is operated in a vacuum chamber. A Langmuir double probe is inserted in the gas inlet of the thruster. The OES measurement is carried out through an optical window with focus on the plasma.

measured spectra are determined by applying a principal component analysis [13] (PCA). The PCA yields a simplified coordinate system in which each spectrum can be displayed as a single point in a low-dimensional, e.g., two-dimensional coordinate space. The plasma parameters, electron temperature and electron density determined, by the Langmuir measurements are then fitted onto the new PCA coordinates using a suitable polynomial surface fitting function yielding one-to-one correspondences between the PCA coordinates and the two plasma parameters. When an optical emission spectrum is acquired on the thruster operating with extraction in the same plasma region as previously studied in the reference setup, it can be transformed into a data point in the PCA space. Afterwards its coordinates in PCA space can be used to extract the corresponding plasma parameters from the polynomial fits of the electron temperature and electron density surfaces. This procedure can be repeated for different operational points which enables us to relate the plasma parameters with the thruster's performance without the need for a Langmuir probe measurement.

II. Experimental details and theory

A schematic depiction of the experimental setup used in this study is shown in Fig. 1. The thruster is a laboratory prototype of a RIT-10 with a cylindrical discharge chamber with 10 cm diameter and an extraction system consisting of three grids. The xenon plasma is generated by a radio-frequency generator (RFG) [14, 15] at a frequency of approximately 1.6 MHz. The thruster is operated in grounded mode without a neutralizer. A Langmuir double probe is inserted into the thruster through the gas inlet to measure the plasma parameters. The optical emission spectroscopy (OES) measurements are performed from the outside of the vacuum chamber through an optical window. The light from the plasma is focused onto an optical fiber, which is connected to a Czerny-Turner spectrometer with an optical length of 0.5 m and an intensified charge coupled device (ICCD) for detection. The OES measurements are performed at a distance of approximately 3.15 m from the thruster and under an angle of approximately 33° to the beam direction.

The test power supply (TPS) consists of the individual power supplies for the negative and positive high voltage

(NHV and PHV) grids, the RFG, and the mass flow controller (MFC). The grid voltages are set to +1700 V on the PHV grid and −100 V on the NHV grid when extracting an ion beam. This setting yields a focused ion beam for the investigated beam currents in the range from 40 mA to 80 mA. Since the Langmuir measurement unit can only be biased with 250 V to ground, no Langmuir measurements are performed with active extraction, as the plasma and the probe will be biased by the PHV. Instead, we measure OES and Langmuir simultaneously without extraction for a wide range of RFG input powers and xenon gas flows. Afterwards, we unplug the Langmuir probe from the measurement unit and perform only OES measurements for different thrusts and xenon gas flows.

A. Principle component analysis

The optical spectra obtained from the OES measurements contain 1024 data points each. This means that each spectrum can be interpreted as a single point in a 1024-dimensional coordinate space. Naturally, correlations between data in such coordinate systems are hard to detect, so the dimensions have to be reduced preserving as much of the differences between the data as possible to allow for an easier comparison between different spectra. For this purpose, the seven emission lines of xenon in the spectral window are in a first step integrated by adding the intensity values over the full width of the emission lines, leaving a single spectrum as a data point in a coordinate system with only seven dimensions. To further reduce the dimensions, the OES data is evaluated using the principle component analysis (PCA) [13] in a second step. The PCA determines the axes with the highest variance in the data set to transform the data into a new coordinate system based on these axes. This is done by setting up the covariance matrix of the measured spectra and finding its eigenvectors $\overrightarrow{PC_i}$. The first PCA axis along the first eigenvector $\overrightarrow{PC_1}$ then accounts for the highest variance of the data set, the second PCA axis along $\overrightarrow{PC_2}$ for the second highest variance and so on. The new coordinates on these PCA axes are also called scores. While the seven dimensions of the data points still yield seven dimensions after the PCA, the first, e. g., two axes are usually already sufficient to describe the differences of the spectra. This way, the dimensions are effectively reduced from 1024 to 2, yielding an easy way to discover correlations between input parameters and optical spectrum.

B. Langmuir

In a Langmuir double probe measurement, a sweeping voltage is applied between two probe wires which are inserted into the plasma. The resulting voltage-current-characteristic is evaluated to extract the plasma parameters electron temperature T_e and electron density n_e [8, 16–18]. The evaluation procedure used here is a modified approach on the basis of the standard procedure [8, 16–18]. This modified approach is described in more detail in our previous publications [11, 12]. Briefly summarized, the saturation region of the typical Langmuir double probe characteristic is fitted with a linear dependence. The measured curve is corrected using the slope of the fit and normalized by the intercept. Now, the electron temperature can be calculated from the maximum slope at a voltage of approximately zero, which is determined using a third order polynomial fit in this region.

III. Results and discussion

The measured OES and Langmuir data is evaluated and shown in Fig. 2. Every point in the resulting PCA of the OES data depicted in Fig. 2 (a) corresponds to a spectrum measured at a specific operational point of the thruster. It can be seen that the data points representing the spectra are well separated from one another. Only some points at low PC_1 values overlap. The measurement series for different constant gas flows are arranged in curved lines, which reflects the changes in the RFG input power. In this case, the first axis PC_1 accounts for 97.40% of the data variance, which mainly corresponds to changes in the RFG input power. The second axis PC_2 accounts for only 2.54% of the data variance and mainly contains the information about the gas flow.

The electron temperatures T_e and densities n_e from the Langmuir double probe measurements shown in Fig. 2 (b) also can be roughly separated in terms of gas flow and RFG input power. As expected, the temperature rises with lower gas flows and the ion density rises with higher input power [19–21].

The plasma parameters from Fig. 2 (b) are then plotted over the PCA scores shown in Fig. 2 (a) yielding Fig. 2 (c) and (d) for T_e and n_e, respectively. A two dimensional polynomial of the form

$$f(PC_1, PC_2) = \sum_{i=0}^{n} \sum_{j=0}^{i+j\leq n} a_{ij} \cdot PC_1^i \cdot PC_2^j \tag{1}$$

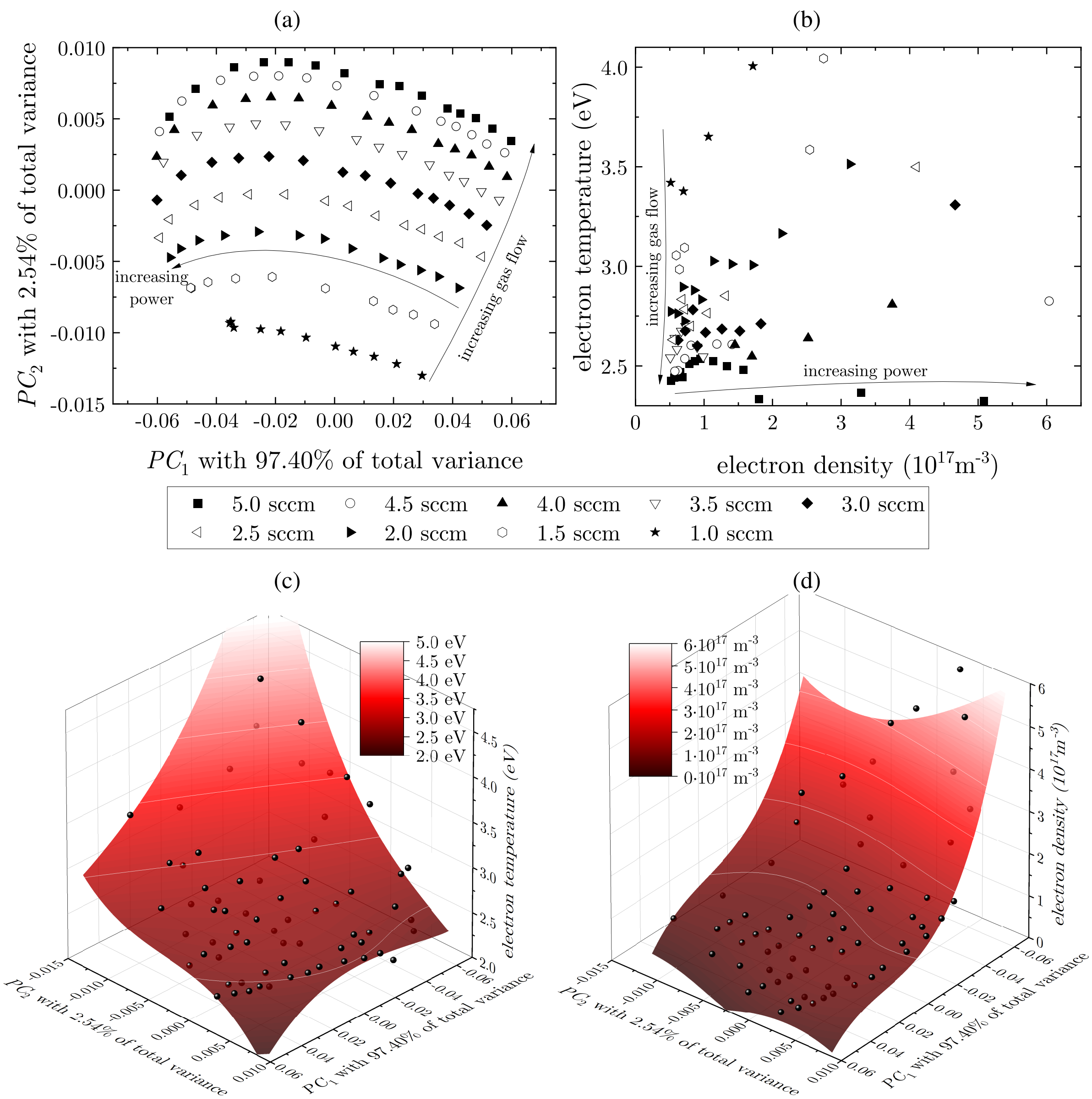

Fig. 2 The PCA data corresponding to the measured spectra are well separated in the reduced coordinate system from the PCA (a). The corresponding Langmuir results are shown in (b). The correlations between PCA and Langmuir results are shown for the electron temperature in (c) and the electron density in (d).

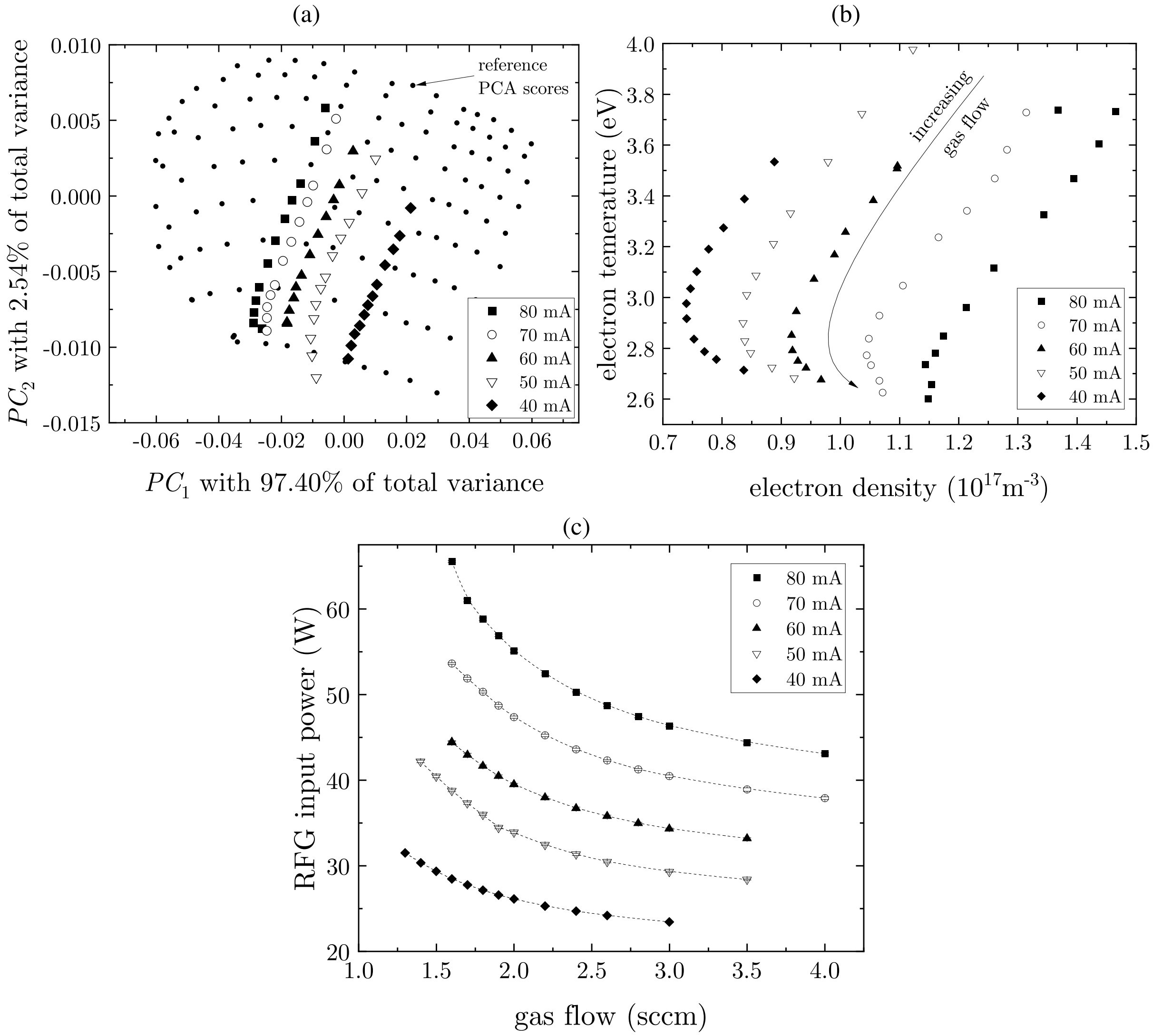

Fig. 3 The PCA scores of the OES measurements during ion beam extraction are shown in (a). The PCA scores of the reference data set are shown as small dots for comparison. The plasma parameters extracted from the PCA scores are shown in (b). The performance curves of the five measured beam currents are shown in (c).

with $n = 3$ is fitted to the data to obtain the functions $T_e(PC_1, PC_2)$ and $n_e(PC_1, PC_2)$, thus correlating the two measurements. The R^2-values from these fits are 0.93 for T_e and 0.96 for n_e. Overall, the results are very similar to previous measurements on a RIT-like setup [11, 12].

This correlation between plasma parameters and optical spectrum is now applied to OES measurements recorded during active ion beam extraction. The results of this measurement series are shown in Fig. 3. The lines of the recorded spectra are integrated, which yields a vector $\overrightarrow{S}$ with seven components, each component corresponding to the intensity of an emission line. The PCA scores PC_i of these OES measurements shown in Fig. 3 (a) are obtained using the eigenvectors $\overrightarrow{PC_i}$ and the vector of the average integrated spectrum $\langle\overrightarrow{S}\rangle$ of the previously performed PCA

$$PC_i = \left(\overrightarrow{S} - \langle\overrightarrow{S}\rangle\right) \cdot \overrightarrow{PC_i}. \tag{2}$$

It can be seen that the PCA scores of the OES measurements during extraction fall within the reference data set and follow a logical pattern determined by gas flow and beam current, so it can be assumed that the correlation derived for the case without extraction still holds. The plasma parameters in Fig. 3 (b) are obtained by inserting the PCA scores into the polynomial fit functions $T_e(PC_1, PC_2)$ and $n_e(PC_1, PC_2)$. It can be observed that the electron temperature decreases with increasing gas flow, which matches the expectations [19–21]. The electron densities shift towards higher values with higher beam currents, which is also expected [19–21]. The shape of the curves shows a decrease in electron density with increasing gas flow at first followed by an increase in electron density towards higher gas flows. We are still investigating the cause of this behavior. However, it has to be noted that the OES measurement reflects the spatially averaged spectrum, as the light of the plasma is focused on the spectrometer entrance slit. The Langmuir diagnostics are representative of a small volume inside the thruster. Differences in spatial distribution of plasma parameters can be misleading, as they might be interpreted as slight global changes of plasma parameters. A direct measurement of plasma parameters during ion beam extraction might be necessary to verify the results acquired here.

Fig. 3 (c) shows the measured performance curves for the five different beam currents. As expected, the required power rises with decreasing gas flow as a higher ionization degree is needed to maintain the beam current.

IV. Conclusion

In this work, we measured optical emission spectra simultaneously with Langmuir diagnostics on a RIT-10 operating with xenon and without ion beam extraction. The OES measurements were simplified by applying a PCA. This yielded a two-dimensional coordinate space in which a spectrum can be displayed as a single point and spectra of different operational points can be distinguished easily. Electron temperature and density were determined from the Langmuir double probe measurements at these points of operation. Langmuir and OES measurements were correlated by fitting the plasma parameters to the PCA results.

Furthermore, we showed that the optical emission spectra of the plasma of the same RIT-10 thruster with ion beam extraction are in the range covered previously by the measurements without ion beam extraction. Therefore, the correlation established between simultaneously measured plasma parameters and OE spectra in case of no extraction can be applied to the OES measurements recorded during extraction, yielding the corresponding plasma parameters. Overall, these plasma parameters determined from the OES measurements behave in a reasonable manner.

Further validation of the approach by experiment as well as by comparison with global modeling of the thruster is still necessary. However, our results underline that a non-invasive OES measurement which can be easily performed, can yield valuable insight into the behavior of the plasma inside an ion thruster and thus its performance.

Acknowledgments

B. Nauschütt and F. Becker are grateful for funding of their PhD positions by the JLU-Ariane Group Graduate School “Radio frequency ion thrusters.” Furthermore, EU regional funding via the EFRE scheme of the State of Hesse is gratefully acknowledged.

References

[1] Holste, K., Dietz, P., Scharmann, S., Keil, K., Henning, T., Zschätzsch, D., Reitemeyer, M., Nauschütt, B., Kiefer, F., Kunze, F., Zorn, J., Heiliger, C., Joshi, N., Probst, U., Thüringer, R., Volkmar, C., Packan, D., Peterschmitt, S., Brinkmann, K. T., Zaunick, H.-G., Thoma, M. H., Kretschmer, M., Leiter, H. J., Schippers, S., Hannemann, K., and Klar, P. J., “Ion thrusters for electric propulsion: Scientific issues developing a niche technology into a game changer,” *Review of Scientific Instruments*, Vol. 91, No. 6, 2020, p. 061101. https://doi.org/10.1063/5.0010134.

[2] Groh, K. H., Loeb, H. W., and Velten, H. W., “Performance data comparison of the inert gas RIT 10,” Vol. 21, No. 4, 1984, pp. 360–365. https://doi.org/10.2514/3.25663.

[3] Kim, V., Popov, G. A., Kozlov, V., Skrylnikov, A., and Grdlichko, D., “Investigation of SPT Performance and Particularities of it’s Operation with Kr and Kr/Xe Mixtures,” 2001.

[4] Linnell, J. A., and Gallimore, A. D., “Internal plasma potential measurements of a Hall thruster using xenon and krypton propellant,” Vol. 13, No. 9, 2006, p. 093502. https://doi.org/10.1063/1.2335820.

[5] Linnell, J. A., and Gallimore, A. D., “Efficiency Analysis of a Hall Thruster Operating with Krypton and Xenon,” Vol. 22, No. 6, 2006, pp. 1402–1418. https://doi.org/10.2514/1.19613.

[6] Holste, K., Gärtner, W., Zschätzsch, D., Scharmann, S., Köhler, P., Dietz, P., and Klar, P. J., “Performance of an iodine-fueled radio-frequency ion-thruster,” *The European Physical Journal D*, Vol. 72, No. 1, 2018. https://doi.org/10.1140/epjd/e2017-80498-5.

[7] Dietz, P., Gärtner, W., Koch, Q., Köhler, P. E., Teng, Y., Schreiner, P. R., Holste, K., and Klar, P. J., “Molecular propellants for ion thrusters,” *Plasma Sources Science and Technology*, Vol. 28, No. 8, 2019, p. 084001. https://doi.org/10.1088/1361-6595/ab2c6c.

[8] Demidov, V. I., Ratynskaia, S. V., and Rypdal, K., "Electric probes for plasmas: The link between theory and instrument," *Review of Scientific Instruments*, Vol. 73, No. 10, 2002, pp. 3409–3439. https://doi.org/10.1063/1.1505099.

[9] Vlcek, J., and Pelikan, V., "A collisional-radiative model applicable to argon discharges over a wide range of conditions. II. Application to low-pressure, hollow-cathode arc and low-pressure glow discharges," *Journal of Physics D: Applied Physics*, Vol. 22, No. 5, 1989, pp. 632–643. https://doi.org/10.1088/0022-3727/22/5/010.

[10] Boffard, J. B., Jung, R. O., Lin, C. C., Aneskavich, L. E., and Wendt, A. E., "Argon 420.1–419.8 nm emission line ratio for measuring plasma effective electron temperatures," *Journal of Physics D: Applied Physics*, Vol. 45, No. 4, 2012, p. 045201. https://doi.org/10.1088/0022-3727/45/4/045201.

[11] Nauschütt, B. T., Chen, L., Holste, K., and Klar, P. J., "Non-invasive assessment of plasma parameters inside an ion thruster combining optical emission spectroscopy and principal component analysis," *EPJ Techniques and Instrumentation*, Vol. 8, No. 1, 2021. https://doi.org/10.1140/epjti/s40485-021-00070-x.

[12] Nauschütt, B., Chen, L., Holste, K., and Klar, P. J., "Combination of optical emission spectroscopy and multivariate data analysis techniques as a versatile non-invasive tool for characterizing xenon/krypton mixed gas plasma inside operating ion thrusters," *Journal of Applied Physics*, Vol. 131, No. 5, 2022, p. 053301. https://doi.org/10.1063/5.0074412.

[13] Abdi, H., and Williams, L. J., "Principal component analysis," *Wiley Interdisciplinary Reviews: Computational Statistics*, Vol. 2, No. 4, 2010, pp. 433–459. https://doi.org/10.1002/wics.101.

[14] Simon, J., Probst, U., and Klar, P. J., "Development of a Radio-Frequency Generator for RF Ion Thrusters," *34th International Electric Propulsion Conference, Hyogo-Kobe, Japan*, 2015.

[15] Junker, J. E., Probst, U., and Klar, P. J., "Development of a full bridge series resonant radio-frequency generator for optimized RIT operation," *36th International Electric Propulsion Conference, Vienna, Austria*, 2019.

[16] Benedikt, J., Kersten, H., and Piel, A., "Foundations of measurement of electrons, ions and species fluxes toward surfaces in low-temperature plasmas," *Plasma Sources Science and Technology*, Vol. 30, No. 3, 2021, p. 033001. https://doi.org/10.1088/1361-6595/abe4bf.

[17] Johnson, E. O., and Malter, L., "A Floating Double Probe Method for Measurements in Gas Discharges," *Physical Review*, Vol. 80, No. 1, 1950, pp. 58–68. https://doi.org/10.1103/physrev.80.58.

[18] Bhattarai, S., "Interpretation of Double Langmuir Probe I-V Characteristics at Different Ionospheric Plasma Temperatures," *American Journal of Engineering and Applied Sciences*, Vol. 10, No. 4, 2017, pp. 882–889. https://doi.org/10.3844/ajeassp.2017.882.889.

[19] Goebel, D. M., and Katz, I., *Fundamentals of Electric Propulsion*, 1^{st} ed., John Wiley & Sons, Hoboken, 2008.

[20] Reeh, A., Probst, U., and Klar, P. J., "Global model of a radio-frequency ion thruster based on a holistic treatment of electron and ion density profiles," *The European Physical Journal D*, Vol. 73, No. 11, 2019. https://doi.org/10.1140/epjd/e2019-100002-3.

[21] Dietz, P., Reeh, A., Keil, K., Holste, K., Probst, U., Klar, P. J., and Volkmar, C., "Global models for radio-frequency ion thrusters," Vol. 8, No. 1, 2021. https://doi.org/10.1140/epjti/s40485-021-00068-5.